

Investigation of laser-plasma interactions at near-critical densities

Dissertation
zur Erlangung des akademischen Grades

doctor rerum naturalium (Dr. rer. nat.)

vorgelegt dem Rat der Physikalisch-Astronomischen Fakultät
der *Friedrich-Schiller-Universität Jena*



von MSc. Ajay Kawshik Arunachalam

geboren am 28.07.1985 in Karamadai, Indien

Vorsitzender:

Gutachter:

1. **Prof. Dr. Malte C. Kaluza**
Institut für Optik und Quantenelektronik
Friedrich-Schiller-Universität Jena, Deutschland
2. **Prof. Dr. Laszlo Veisz**
Fakultät für Physik
Universität Umeå, Schweden
3. **Prof. Dr. Stefan Skupin**
Centre Lasers Intenses et Applications (CELIA)
Universität Bordeaux, Frankreich

Tag der Disputation : 14-Dec-2017

Zusammenfassung

In der vorliegenden Arbeit wurden zwei Experimente mit dem Hochleistungs-Lasersystem JETI40 am IOQ durchgeführt, welche die Wechselwirkung zwischen dem Hochintensität-laser und dem von ihm erzeugten Plasma untersuchten. In den Experimenten traten unterschiedliche Seitenstreuungsprozesse, in Bezug auf die Ausbreitungsrichtung des Laserpulses, auf, die sich in ihrer Ausprägung und Ursache unterscheiden. Im ersten Experiment wurde eine asymmetrische Seitenstreuung beobachtet, welche bei unter-dichten bis viertel-kritischen Plasmadichten auftritt. Es wurde weiterhin eine Abhängigkeit der Asymmetrie der Streuung bei Veränderung der Gasdichte festgestellt. In dieser Arbeit wird gezeigt, dass der Seitenstreuungsprozess eine Konsequenz der Laserausbreitung in ungleichförmigen Plasmen ist, wobei sich der Streuwinkel entlang der Richtung des Plasmagradients orientiert. In dem zweiten Experiment wurde ein symmetrischer Seitenstreuungsprozess aus dem intensiven zentralen Laser-Plasma-Wechselwirkungsbereich beobachtet. Es zeigte sich, dass diese Streuung aus einem in Längsrichtung orientierten engen Laser-Plasma-Wechselwirkungsbereich stammt und über $\pm 50^\circ$ in Bezug auf die transversale Richtung des Lasers variiert. Weiter wurde festgestellt, dass diese primär in nahekritischen Plasmadichten vorkommt ($0.09n_c - 0.25n_c$, wobei n_c die plasmakritische Dichte ist). Im Gegensatz zum ersten Experiment ist die Raman-Streuung die Ursache für diesen symmetrischen Streuprozess, bei dem die Streuung aufgrund des unausgerichteten Wellenvektors zwischen dem Hauptlaserpuls und der von ihm verursachten Plasmawalle auftritt.

Abstract

During the high-intensity laser-plasma experiments conducted at the high-power laser system JETI40 at IOQ, the two qualitatively different laser side-scattering processes have been observed. The side-scattering observed during the first experiment was found to be non-symmetric in nature with respect to the laser's propagation direction and it was estimated to occur from under-dense to quarter critical plasma densities. The scattering angle was found to gradually decrease, as the laser pulse propagates towards regions of higher densities (i.e. the gas jet centre). For increasing nozzle backing pressures, the scattering was also found to gradually change from upward to downward directions. In this thesis, this side-scattering process is shown to a consequence of the laser propagation in non-uniform plasma, where the scattering angle was found to be oriented along the direction of the plasma gradient. In the second experiment, a symmetric side-scattering process with respect to the laser's propagation direction was observed from the intense central laser-plasma interaction region. This scattering process was found to originate from a longitudinally narrow laser-plasma interaction region and vary over $\pm 50^\circ$ with respect to the laser's transverse direction. It was found to primarily occur in the near-critical plasma density regime ($0.09n_c - 0.25n_c$, where n_c is the plasma critical density). In contrast to the previous experiment, Raman scattering has been shown to be the cause of this symmetric scattering process, where the scattering occurs as the result of the wave vector non-alignment between the main laser pulse and the resulting plasma wave.

Contents

1	Introduction	1
2	Theory	4
2.1	Ultra-short Laser Pulse	4
2.1.1	Mathematical Description	4
2.1.2	Laser Intensity	5
2.1.3	Spectral Representation	6
2.2	Ionisation Mechanisms	7
2.2.1	Keldysh Parameter	7
2.2.2	Tunnel Ionisation	8
2.2.3	Barrier Suppression Ionisation	9
2.3	Electron - Light Interaction	10
2.3.1	Non-relativistic Case	11
2.3.2	Relativistic Case	11
2.4	Ponderomotive Force	12
2.5	Plasma Properties	15
2.6	Laser Propagation in Plasma Medium	17
2.6.1	Linear Response	17
2.6.2	Nonlinear Response	20
2.7	Laser Wakefield Acceleration	20
2.8	Direct Laser Acceleration (DLA)	22
2.9	Propagation Effects	24
2.9.1	Ionisation Induced Defocusing	24
2.9.2	Self-focusing in Plasma	27
2.9.3	Self-Phase Modulation	29
2.10	Laser-Plasma Instabilities	31
2.10.1	Generalised Plasma Description	32
2.10.2	Raman Scattering	33
2.10.3	Formulation	36
2.10.4	Two Plasmon Decay (TPD)	38
2.10.5	Modulational and Filamentation Instability	39
2.10.6	Other Instabilities	42

3	Experimental Set-up	44
3.1	Laser-Plasma Experiments	44
3.1.1	Experimental Layout	44
3.1.2	Interferometry Diagnostic	47
3.2	Gas Nozzle Characterisation	49
3.2.1	Valve-Nozzle Construction	49
3.2.2	Mach-Zehnder Interferometer	53
3.2.3	Interferogram Analysis	53
4	Results and Discussion	61
4.1	June 2014 Experiment	61
4.1.1	Side-view Images	61
4.1.2	Limitations of Interferometry	65
4.1.3	Electron Density Estimation	66
4.2	Scattering Measurement	67
4.3	Scattering Mechanisms	69
4.3.1	Raman Scattering	69
4.3.2	Plasma Grating	71
4.3.3	Ionization Induced Defocusing	72
4.4	Gradient Analysis	73
4.4.1	Gas Jet Simulation	74
4.4.2	Electron Density Analysis	75
4.4.3	Origin of Side-scattering	78
4.5	March 2015 Experiment	82
4.5.1	Side-view Images	82
4.5.2	Scattering Measurement	85
4.5.3	Scattering Origin	86
4.5.4	Further Comments	90
5	Conclusion and Outlook	91
	Bibliography	93

Chapter 1

Introduction

Particle beams, depending on their type and energy, can be used for a wide range of applications, such as nuclear fusion¹⁻³, cancer treatment⁴, material structural probing^{5,6}, lithography⁷ and the investigation of subatomic physics⁸. They can either be composed of charged particles⁹, such as electrons, protons and heavy ions, or be composed of neutral particles, such as neutrons. Charged particles are traditionally accelerated by applying alternating electromagnetic fields inside a solid structure, whose acceleration field is limited up to $\sim 10^6$ V/m due to the (solid) material damage threshold¹⁰. Therefore, if the kinetic energy of the particle beams is increased, such as in the case of cancer treatment, where higher ion energies lead to higher penetration depths¹¹, longer accelerating structures need to be constructed. For instance, the SLAC linear accelerator¹² located in California (US) is capable of accelerating electron beams up to 50 GeV energies over a length of 3.2 km.

An alternative way of accelerating electrons was first theoretically proposed by Tajima and Dawson¹³ in 1979. It involves exciting longitudinal electron density oscillations in plasma on spatial-scales greater than the Debye length¹⁴. This can be achieved using, for instance, an intense ultrashort laser-pulse and subsequently trapping electrons for them to be accelerated up to a few GeV energies¹⁵. This particle acceleration mechanism is called the laser wakefield acceleration (LWFA), where ions are assumed to be stationary on these time-scales. In contrast to solid structures, plasma excitations offer electric-fields in the order of $\sim 10^{12}$ V/m thus making them an attractive alternative, as it dramatically reduces the distances over which a particular electron energy can be achieved. Ever since its first proposal, LWFA has been the subject of extensive theoretical^{13;16-18} and experimental¹⁹⁻²² investigations to dominate in the under-dense plasma regime (i.e. $n_e \leq 0.1n_c$, where n_e is the plasma density and n_c is the critical plasma density). At over-critical plasma-densities (i.e. $n_e > n_c$), which can be generated through the interaction between the laser-pulse and a thin foil of thickness ranging from a few 10's of nanometres up to a few microns, laser driven ion acceleration mechanisms, such as target normal sheath acceleration (TNSA) and radiation pressure acceleration (RPA) have been shown to dominate. In the last two decades, these mechanisms have also been the subject of an extensive theoretical²³⁻²⁶ and experimental^{24;27-29} investigation.

In the plasma density regime, which is close to and less than the critical density (i.e. $0.1n_c < n_e < n_c$), the interaction dynamics between an intense ultrashort laser-pulse

($\Delta\tau < 35$ fs) and plasma have been found to be uniquely characterised by phenomena, such as resonant laser absorption³⁰, relativistic self-focusing³¹, Direct Laser Acceleration (DLA)³², hole boring³³, soliton formation³⁴, vortex formation³⁵, laser pulse collapse³⁶ and gamma ray generation³⁷. In the case of the electron acceleration mechanism DLA, whereby a single electron filament is formed and sustained by its self-generated magnetic-field, in which electrons can resonantly interact with the co-propagating laser-pulse to gain energies up to several hundred³⁸ MeV. In this near-critical density regime, the energy transfer from the laser-pulse to the electrons is expected to be greater than in the case of under-dense plasma due to the near-resonance between the laser and plasma frequencies.

Although a number of experiments have been carried out to explore this electron acceleration mechanism^{32;39-41}, our understanding of the laser-plasma interaction dynamics at this density regime and kind of instabilities that could arise during the interaction is still imperfect. A few of the past experiments made use of foam targets and gas jets to produce near-critical plasma. The experiments involving foam targets were primarily aimed at investigating the dependency of the energy of the accelerated ions on the target thickness^{42;43}. Because of the nature of the foam targets, they could not be optically probed, thus limiting any direct insight into the laser-plasma interaction dynamics. Whereas, in the case of the experiment involving helium gas jet³⁶, the use of an optical probe revealed the phenomenon of laser pulse collapse, which refers to the strong and almost complete absorption of laser-pulse at near-critical densities. However, more details about the laser-plasma interaction dynamics could not be revealed.

Therefore, in order to understand the interaction dynamics between an intense laser-pulse and near-critical plasma, two high-intensity laser-plasma experiments have been conducted at the high-power laser system JETI40 at IOQ, Jena. These experiments used two different focusing geometries with the help of $f/6$ and $f/2$ off-axis parabolas, respectively and two different argon gas jet flow geometries, respectively were aimed at exploring different laser intensity and plasma-density combinations. These experiments contained necessary particle detection diagnostics, such as electron spectrometer and scintillator screen capable of detecting energetic ions, and a second-harmonic probe beam, which was intended to backlight the interaction region. Thus, the interaction region could be directly imaged at 90° to the laser's propagation direction.

Thesis Outline

This thesis has been structured in the following way:

Chapter 2 summarises the theoretical background of this research work. It starts with an introduction to the description of a laser-pulse and ionisation mechanisms involved in producing the plasma. It then describes the interaction dynamics between a laser-pulse and a single electron, followed by the collective plasma response to an intense laser-pulse.

It is then followed by the description of electron acceleration mechanisms in under-dense and near-critical plasma, the propagation effects that a laser-pulse might undergo in plasma, and the kind of instabilities that could arise during the laser-plasma interactions.

Chapter 3 provides a description of the experimental setup and the various plasma and particle-detection diagnostics used in the high-intensity laser-plasma experiments conducted at the high-power laser-system JETI40 at IOQ. The targets used in these experiments, namely subsonic and transonic gas-jets, are discussed in detail. It first provides a description of the design, construction and operation of the gas-nozzles used, which is then followed by a description of the Mach-Zehnder interferometry technique that was used to characterise the gas nozzles. The steps involved in analysing the corresponding interferograms obtained using the Mach-Zehnder interferometer are also discussed in detail.

Chapter 4 contains the results obtained from the two subsequent high-intensity laser-plasma experiments conducted at JETI40. Although no energetic particles have been observed during the experiments, the results show the presence of two qualitatively different laser side-scattering processes during the laser-plasma interactions at under-dense to near-critical plasma densities. This chapter explores the various characteristics of the observed side-scattering processes and finds possible explanations of their origins.

Chapter 5 summarises the results obtained from the experiments conducted at JETI40 and provides an outlook into how these results can be utilised to benefit the future high-intensity laser-plasma experiments aimed processes, such as electron acceleration or plasma fusion.

Chapter 2

Theory

Since this research work is primarily concerned with the interaction of ultra-short laser pulses with a FWHM pulse duration $\Delta\tau = 30$ fs with a plasma medium, a basic discussion on ultra-short laser pulses, plasma characteristics, various laser pulse propagation effects and laser-plasma instabilities that could potentially arise during the interaction will be presented in this chapter.

2.1 Ultra-short Laser Pulse

In the context of this thesis, the term 'ultra short' laser pulse refers to an electro-magnetic wave packet of FWHM duration $\Delta\tau = 30$ fs, which is much longer than an optical cycle ($T_{opt} = 2.67$ fs for 800 nm), meaning that the pulse contains many electric-field oscillations.

2.1.1 Mathematical Description

A laser pulse that is linearly polarized in x -direction and propagating in z -direction, which is spatially and temporally confined can be mathematically expressed in terms of its electric field (\mathcal{E} -field) variations in the following way:

$$\vec{\mathcal{E}}(x,y,z,t) = \mathcal{E}_0 \underbrace{\exp\left[-\left(\frac{x^2 + y^2}{w_l^2}\right)\right] \exp\left[-\left(\frac{t}{\tau_G}\right)^2\right]}_{\text{spatial and temporal envelope}} \underbrace{\exp[i(\omega_0 t - kz + \phi_0)]}_{\mathcal{E}\text{-field oscillations}} \hat{x} \quad (2.1)$$

where, $\vec{\mathcal{E}}$ is expressed in complex field notation, where the physical field is the real-part of $\vec{\mathcal{E}}$, \mathcal{E}_0 is the \mathcal{E} -field amplitude, $w_l = d_0/2\sqrt{\ln 2}$ with d_0 being the full width at half maximum (FWHM) laser focal spot size, $\tau_G = \Delta\tau/2\sqrt{\ln 2}$ with $\Delta\tau$ being the FWHM pulse duration, ω_0 is the central laser frequency, wave number $k = 2\pi/\lambda_0$ with λ_0 being the central laser wavelength, and ϕ_0 is the carrier envelope phase (CEP). Here, the laser pulse is assumed to have a Gaussian shaped envelope both in spatial and temporal domains. The CEP is the phase relationship between the envelope and \mathcal{E} -field oscillations, which in our case can be neglected, as the envelope contains many oscillations.

For the sake of simplicity and mathematical convenience, equation 2.1 can be reduced to its temporal dependence in the following form representing the variation of the laser's \mathcal{E} -field at a fixed point in space along its propagation axis⁴⁴:

$$\tilde{\mathcal{E}}(t) = \mathcal{E}_0 \exp \left[- \left(\frac{t}{\tau_G} \right)^2 \right] \exp[i(\omega_0 t + \phi_a(t))] \quad (2.2)$$

where the phase term $\phi_a(t)$ is introduced to account for the various pulse propagation effects, such as dispersion and self-phase modulation that might occur in plasma. The term $\omega_0 t$ represents the primary field oscillations, where ω_0 can be related to T_{opt} through $T_{opt} = 2\pi/\omega_0$. If $\phi(t) = \omega_0 t + \phi_a(t)$ is to represent the instantaneous phase of the laser pulse, its instantaneous frequency $\omega(t)$ is given by,

$$\omega(t) = \frac{d\phi(t)}{dt} = \omega_0 + \frac{d\phi_a}{dt} \quad (2.3)$$

The magnitude of the magnetic field (\mathcal{B} -field) oscillations of the laser pulse can be related to its \mathcal{E} -field magnitude through⁴⁵ $\vec{k} \times \vec{\mathcal{B}}_0 = -\omega \vec{\mathcal{E}}_0$, where the \mathcal{E} -field $\vec{\mathcal{E}}_0$ is oriented perpendicular to both the \mathcal{B} -field $\vec{\mathcal{B}}_0$ and propagation direction \vec{k} .

2.1.2 Laser Intensity

The laser pulse's intensity (I) can be defined as the cycle-average of the magnitude of the Poynting vector⁴⁵. For a plane wave propagating in vacuum, this quantity is given by $I = (1/2)\epsilon_0 c \mathcal{E}_0^2$, where ϵ_0 is the vacuum permittivity and c is the speed of light in vacuum. For a Gaussian pulse described by equation 2.1, the time-averaged intensity distribution $I(r,t)$ can be expressed in terms of the experimentally measurable quantities such as pulses's energy (E_t), diameter (d_0) and duration ($\Delta\tau$), as the spatio-temporal dependence of the E-field is experimentally difficult to measure. Thereby,

$$I(r,t) = \underbrace{E_t \cdot \frac{8}{d_0^2 \Delta\tau} \left[\frac{\ln 2}{\pi} \right]^{3/2}}_{I_0} \exp \left[-4 \ln 2 \left(\frac{r}{d_0} \right)^2 \right] \exp \left[-4 \ln 2 \left(\frac{t}{\Delta\tau} \right)^2 \right] \quad (2.4)$$

where I_0 is the peak laser-intensity, E_t is the total energy content of the laser-pulse, d_0 is the FWHM beam diameter and $\Delta\tau$ is the FWHM pulse duration. Equation 2.4 satisfies the integral of the form:

$$E_t = 2\pi \int_0^\infty \int_0^\infty I(r,t) r dr dt \quad (2.5)$$

Whereas the average laser intensity corresponding to the FWHM parameters d_0 and $\Delta\tau$ can be calculated in the following way

$$I_{avg} = \frac{2\pi \int_{-\Delta\tau/2}^{-\Delta\tau/2} \int_0^{d_0/2} I(r,t) r dr dt}{\left[2\pi \int_0^{d_0/2} r dr\right] \cdot \int_{-\Delta\tau/2}^{\Delta\tau/2} dt} = \frac{\text{Energy}}{\text{Area} \cdot \text{Time}} = \frac{E_{FWHM}}{(\pi/4)d_0^2 \cdot \Delta\tau} \quad (2.6)$$

since the energy content (E_{FWHM}) inside the FWHM pulse duration cannot be experimentally measured, it can be approximated to the energy content (E) inside the FWHM focal area, but integrated over times beyond $\pm\Delta\tau/2$. For instance, for $d_0 = 6.6 \mu\text{m}$, $\Delta\tau = 30 \text{ fs}$ and $E = 210 \text{ mJ}$, $I_{max} = 4.1 \times 10^{19} \text{ W/cm}^2$.

For a laser-pulse that is being focused in vacuum, the expression for the intensity distribution along its propagation direction (z) can be written as⁴⁶,

$$I(r,z,t) = I_0 \left[\frac{w_0}{w(z)} \right]^2 \exp \left[-\frac{2r^2}{w(z)^2} \right] \exp \left[-4 \ln 2 \left(\frac{t}{\Delta\tau} \right)^2 \right] \quad (2.7)$$

where I_0 is the peak laser-intensity at focus, the beam-size parameter $w(z) = w_0 \sqrt{1 + (z/z_R)^2}$, the beam-waist $w_0 = d_0/\sqrt{2 \ln 2}$ and the Rayleigh length z_R can be related to the beam-waist w_0 by $z_R = \pi w_0^2/\lambda_0$.

2.1.3 Spectral Representation

The Fourier analysis of a laser pulse of finite duration is bound to contain an extended frequency spectrum. A laser-pulse can thus be thought of as the result of the coherent overlap of several much longer quasi-monochromatic waves. If the phase relationship among these waves can be matched such that a maximum from any one particular wave of a certain frequency coincides with one maximum from each of the other waves corresponding to differing frequencies, they can constructively interfere to produce a laser pulse. The relation between the FWHM pulse duration $\Delta\tau$ and the FWHM spectral width $\Delta\nu$ is given by the so-called Time-Bandwidth Product (TBP): $\Delta\tau\Delta\nu \geq K$ with K ranging from 0.14 – 0.44 depending on the choice of the envelope shape. The Fourier transform of the Gaussian laser pulse represented by eq. (2.2) is given by⁴⁴,

$$\tilde{\mathcal{E}}(\omega) = \int_{-\infty}^{\infty} \mathcal{E}(t) \exp(-i\omega t) dt = \mathcal{E}_0 \Delta\tau \sqrt{\frac{\pi}{2 \ln 2}} \exp \left[-\frac{\Delta\tau^2}{8 \ln 2} \omega^2 \right] \exp[-i\phi(\omega)] \quad (2.8)$$

This yields a TBP of $\Delta\tau\Delta\nu \geq 0.441$, which in terms of wavelength is given by $(c/\lambda_0^2)\Delta\tau\Delta\lambda \geq 0.441$. Consequently, for $\Delta\tau = 30 \text{ fs}$ and a central wavelength of $\lambda_0 = 800 \text{ nm}$, TBP yields a FWHM spectral width of $\Delta\lambda \approx 30 \text{ nm}$.

When a laser-pulse propagating through a material, in which its constituent frequencies propagate at differing speeds, the phase relationship among the frequencies changes as

it propagates. This causes changes in the temporal structure of the laser-pulse, which leads to propagation effects such as group velocity dispersion (GVD) and chirp. These effects can be mathematically examined by expanding the spectral phase $\phi(\omega)$ using a Taylor series⁴⁷ around its central frequency ω_0 . GVD causes the laser-pulse to simply broaden in time during its propagation, whereas chirp, in addition to causing changes in the pulse-duration, also causes changes in the momentary frequency of the laser pulse. A detailed discussion on these effects can be found in the book by Boyd⁴⁷.

2.2 Ionisation Mechanisms

An ensemble of atoms or molecules can be ionised using various mechanisms to produce a plasma medium with which a laser pulse can interact. In the context of this thesis, only laser induced ionisation is considered, by which an argon gas-jet can be ionised to produce plasma, whose density can be varied by the appropriate choice of the nozzle size and backing pressure. Some of the well known ionisation mechanisms are photo-ionisation⁴⁸, multi-photon ionisation (MPI)⁴⁹, tunnel ionisation⁵⁰, and barrier suppression ionisation (BSI)⁵¹. In the case of photo-ionisation, during the interaction between an atom and a laser pulse, an atom can be ionised if the ionisation energy (E_{ion}) of any of its constituent electrons match or exceed the photon energy ($\hbar\omega$). This is the classical photo-electric effect⁴⁸, which in particular works for less intense radiation (i.e. unlike a laser pulse). However, in the case of argon, the photon energy corresponding to $\lambda = 800 \mu\text{m}$ is much less than its first ionisation energy. For example, the ionisation energy needed to achieve Ar^{1+} : $15.8 \text{ eV} \gg 1.55 \text{ eV}$, which is the photon energy corresponding to λ_0 of 800 nm. Therefore, this mechanism is not of relevance here.

2.2.1 Keldysh Parameter

For a given laser's \mathcal{E} -field (\mathcal{E}_0), photon energy ($\hbar\omega_0$) and the ionisation potential (E_{ion}) of an atom, the Keldysh parameter (γ_K) helps to determine if MPI or tunnel ionisation dominates⁵⁰. MPI refers to the ionisation of an atom due to the simultaneous absorption of more than one photon by an electron⁴⁹. Whereas, tunnel ionisation is a process by which an electron tunnels to the potential barrier resulting from the combined \mathcal{E} -field of the atom and the laser field⁵⁰.

The Keldysh parameter γ_K effectively compares the laser's central frequency (ω_0) with the threshold frequency (ω_t) above which the tunneling process is frequency dependent meaning that the laser's \mathcal{E} -field oscillations can be fast enough for the electrons not to have sufficient time to tunnel through the barrier. It can be expressed as⁵⁰,

$$\gamma_K = \frac{\omega_0}{\omega_t} = \frac{\omega_0}{e\mathcal{E}_0/\sqrt{2m_e E_{ion}}} = \sqrt{\left[\frac{4m_e\omega_0^2}{e^2\mathcal{E}_0^2}\right] \frac{E_{ion}}{2}} = \sqrt{\frac{E_{ion}}{2\Phi_p}} \quad (2.9)$$

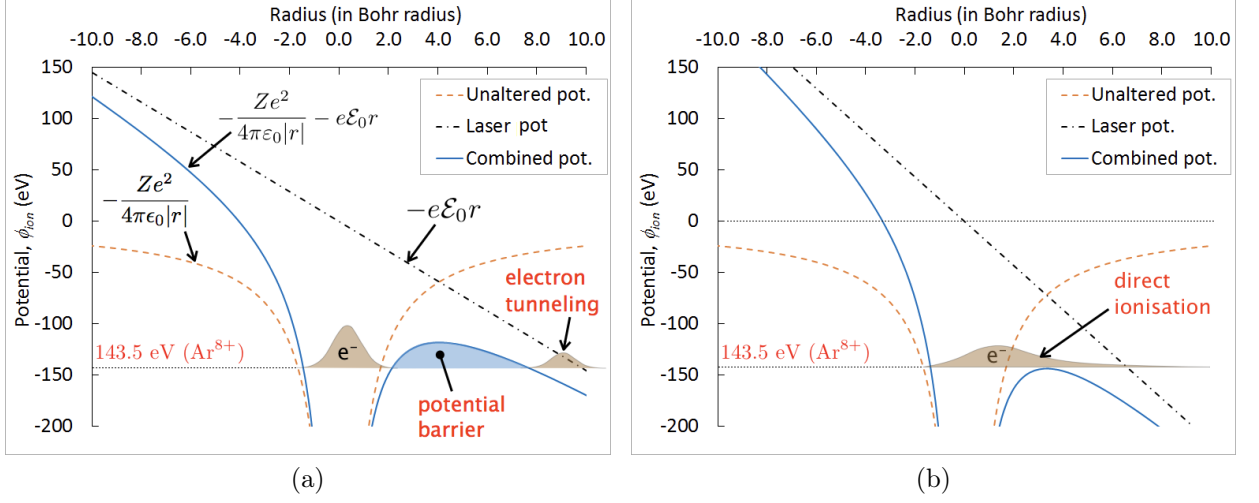


Figure 2.1: (a) Tunnel ionisation of an Ar atom for strong external quasi-static \mathcal{E} -fields, where the electron has been shown to tunnel through the resulting potential barrier of the atom. Here, the laser intensity corresponding to \mathcal{E}_0 is $1 \times 10^{16} \text{ W/cm}^2$ and 143.5 eV corresponds to argon ionisation process of $\text{Ar}^{7+} \rightarrow \text{Ar}^{8+}$ and (b) barrier suppression ionisation process of $\text{Ar}^{7+} \rightarrow \text{Ar}^{8+}$ corresponding to a laser intensity of $2 \times 10^{16} \text{ W/cm}^2$.

where the threshold frequency ω_t is determined from the laser's \mathcal{E} -field \mathcal{E}_0 and the atom's ionisation potential E_{ion} such that $\omega_t = e\mathcal{E}_0/(2m_e E_{ion})^{1/2}$, and the ponderomotive potential $\Phi_p = e^2 \mathcal{E}_0^2 / 4m_e \omega_0^2$. The time required for the electron to tunnel through the potential barrier (i.e. the tunneling time δt) can be related to the threshold frequency ω_t by $\delta t = 1/\omega_t$. MPI dominates for $\gamma_K > 1$, which corresponds to high ionisation energies and low \mathcal{E} -fields. Whereas, tunnel ionisation dominates for $\gamma_K < 1$, which corresponds to low ionisation energies and high \mathcal{E} -fields. For instance, in the case of Ar^{7+} ion, for $I = 10^{16} \text{ W/cm}^2$ and $\lambda_0 = 800 \text{ nm}$, $\gamma_K = 0.25 (< 1)$ meaning that for laser intensities relevant to this experiment, tunnel ionisation dominates over MPI. The corresponding tunneling time $\delta t = 0.1 \text{ fs}$, which is less than the optical cycle time T_{opt} meaning that the laser's \mathcal{E} -field can be assumed to be quasi-stationary during the ionisation process.

2.2.2 Tunnel Ionisation

Tunnel ionisation is a process by which an electron tunnels through the potential barrier resulting from the combined \mathcal{E} -field of the atom and the applied laser field, and gets liberated from the atom, as shown in fig. 2.1a. The modified atomic potential (ϕ_{Ar}) can

be expressed as,

$$\phi_{\text{Ar}} = -\frac{Z_{\text{eff}}e^2}{4\pi\epsilon_0|r|} - e\mathcal{E}_0r = -14.36/\text{eV} \cdot \frac{Z_{\text{eff}}}{|r/\text{\AA}|} - 2.75 \times 10^{-7} \cdot \sqrt{I/\text{Wcm}^{-2}} \cdot (r/\text{\AA}) \text{ eV} \quad (2.10)$$

where Z_{eff} is the reduced effective nuclear charge due to the shielding by inner electrons, as seen by the electron to be ionised, which can be calculated from the Slater's rule⁵², the applied \mathcal{E} -field $\mathcal{E}_0 = (2I/\epsilon_0c)^{1/2}$ and r is the distance from the centre of the nucleus.

For a given applied \mathcal{E} -field, the height ($\delta\phi_{\text{Ar}} = \phi_2 - \phi_1$) and width ($\delta r = r_2 - r_1$) of the potential barrier to be overcome by the electron can be calculated from equation 2.10 by substituting $\phi_{\text{Ar}} = E_{\text{ion}}$, where E_{ion} is the ionisation potential. The tunneling factor, also called the transmission co-efficient (T), which compares the magnitude of the electron's wave function before and after the potential barrier is given by⁵³,

$$T = \exp \left[-\frac{2}{\hbar} \int_{r_1}^{r_2} |p(r)| dr \right], \text{ where momentum } p(r) = \sqrt{2m_e|E_{\text{tot}} - \phi_{\text{Ar}}(r)|} \quad (2.11)$$

where E_{tot} is the total energy of the electron. Assuming that $E_{\text{tot}} = E_{\text{ion}}$, $T = \exp[-0.162 \int (E_{\text{ion}} - \phi_{\text{Ar}})^{1/2} dr/\text{\AA}]$. For example, for the tunnel ionisation process of $\text{Ar}^{7+} \rightarrow \text{Ar}^{8+}$ state shown in fig. 2.1a, where $I = 1 \times 10^{16} \text{ W/cm}^2$ and $E_{\text{ion}} = 143.5 \text{ eV}$, the tunneling factor $T = 0.0035$.

The rate of the probability of ionisation $\Gamma(t)$ in the presence of an external \mathcal{E} -field is given by the ADK-theory, as follows^{54-58†},

$$\Gamma(t) = 4\omega_a \left[\frac{E_{\text{ion}}}{E_{\text{H}_2}} \right]^{5/2} \frac{\mathcal{E}_a}{\mathcal{E}(t)} \exp \left[-\frac{2}{3} \left(\frac{E_{\text{ion}}}{E_{\text{H}_2}} \right)^{3/2} \frac{\mathcal{E}_a}{\mathcal{E}(t)} \right] \quad (2.12)$$

$$= \frac{4.54 \times 10^{22}}{\text{s}^{-1}} \cdot \frac{(E_{\text{ion}}/\text{eV})^{2.5}}{\sqrt{I(t)/\text{Wcm}^{-2}}} \cdot \exp \left[-\frac{2.5 \times 10^6}{\sqrt{I(t)/\text{Wcm}^{-2}}} \right] \quad (2.13)$$

where the angular atomic frequency $\omega_a = (1/16\pi^2\epsilon_0^2)(m_e e^4/\hbar^3) = 4.13 \times 10^{16} \text{ s}^{-1}$, E_{H_2} is ionisation potential of the hydrogen atom, the atomic unit of the \mathcal{E} -field $\mathcal{E}_a = m_e^2 e^5 / (4\pi\epsilon_0)^3 \hbar^4 = 5.14 \times 10^{11} \text{ V/m}$ and $\mathcal{E}(t)$ is the applied \mathcal{E} -field.

2.2.3 Barrier Suppression Ionisation

For sufficiently high laser \mathcal{E} -field values, the electron's potential barrier can be suppressed and the electron can freely escape the Coulomb field of the atom (i.e. the electron can

[†]The original expression for the tunnel ionisation rate of the hydrogen atom was developed by Landau⁵⁴. Further developments were carried out by Perelomov et al.⁵⁵ and Ammosov et al.⁵⁶ to account for atoms of higher atomic numbers, which also takes into account the orbital angular momentum (l) and its projection (m) along the direction of the applied \mathcal{E} -field. In this expression, $l = |m| = 1$ is assumed⁵⁶.

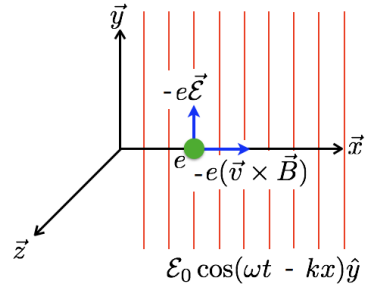


Figure 2.2: (a) Force exerted on an electron by the EM-field of a plane wave.

be directly field ionised). This is referred to as the barrier suppression ionisation (BSI) or over the barrier ionisation (OTBI) mechanism. For a given electron energy level, the electron can be directly field ionised if its ionisation potential E_{ion} equals the modified peak electrostatic potential of the atom⁵¹, as shown in fig. 2.1b. The critical distance (r_c) at which it happens can be obtained by setting the first spatial derivative of equation 2.10 to zero, which yields $r_c^2 = (1/4\pi\epsilon_0)Z_{eff}e/\mathcal{E}_0$. Thus, equating the atomic potential at distance r_c with that of E_{ion} , one obtains the critical laser \mathcal{E} -field $\mathcal{E}_c = (\pi\epsilon_0/Z_{eff}e^3)E_{ion}^2$. Hence, the laser-intensity needed to field ionise the electron, which is referred to as the appearance intensity (I_{app}) is given by,

$$I_{app} = \frac{1}{2}\epsilon_0 c \mathcal{E}_c^2 = 4 \times 10^9 \cdot \left(\frac{E_{ion}}{eV}\right)^4 \cdot \left(\frac{1}{Z_{eff}}\right)^2 \text{ W/cm}^2 \quad (2.14)$$

For example, for the ionisation process $\text{Ar}^{7+} \rightarrow \text{Ar}^{8+}$ corresponding to an ionisation energy of 143.5 eV, $Z_{eff} = 8.8$ and the appearance intensity $I_{app} = 2.2 \times 10^{16} \text{ W/cm}^2$. Here, the effective nuclear charge Z_{eff} has been calculated using the Slater's rule⁵². Therefore, BSI is of relevance for this research work, where laser intensities well above $1 \times 10^{16} \text{ W/cm}^2$ were reached. For higher ionisation states, however, tunnel ionisation still plays a role.

2.3 Electron - Light Interaction

In order to understand the interaction dynamics between an intense laser pulse and plasma, it is worth examining what happens to a single electron in vacuum in the presence of an EM-field. The force exerted by the electric ($\vec{\mathcal{E}}$) and magnetic ($\vec{\mathcal{B}}$) components of a light wave on an electron, as shown in fig. 2.2, is given by⁵⁹,

$$\frac{d}{dt}\vec{p} = \frac{d}{dt}(\gamma_e m_e \vec{v}_e) = -e[\vec{\mathcal{E}} + (\vec{v}_e \times \vec{\mathcal{B}})] \quad (2.15)$$

where, the Lorentz factor $\gamma_e = 1/\sqrt{1 - v_e^2/c^2}$ and v_e is the electron velocity. By making use of the Coulomb gauge⁴⁵, both the \mathcal{E} -field and \mathcal{B} -field can be expressed in terms of

a common variable called the vector potential \vec{A} such that $\vec{\mathcal{E}} = -(\partial\vec{A}/\partial t) - \nabla V$ and $\vec{\mathcal{B}} = \nabla \times \vec{A}$. In the absence of any static \mathcal{E} -field, the electrostatic potential V can be set to zero. Thus, the equation 2.15 can be reduced to the following form:

$$\frac{d}{dt}(\gamma_e m_e \vec{v}_e) = -e \left[\nabla(\vec{v}_e \cdot \vec{A}) - \frac{d\vec{A}}{dt} \right] \quad (2.16)$$

2.3.1 Non-relativistic Case

For electron velocities much less than the speed of light ($v_e \ll c$), the contribution of the magnetic force is negligible compared to its \mathcal{E} -field counterpart i.e. $|\vec{v}_e \times \vec{\mathcal{B}}| = |(\vec{v}_e/c) \times \vec{\mathcal{E}}| \ll |\vec{\mathcal{E}}|$, where the relation $B = \mathcal{E}/c$ (which is valid in vacuum) was used. Therefore, in the classical limit ($\gamma_e = 1$), equation 2.16 can be reduced to:

$$m_e \frac{d}{dt} \vec{v}_e = e \frac{d\vec{A}}{dt} \quad (2.17)$$

At $t = 0$, for an electron at rest at the origin, the expressions for the electron's velocity and displacement can be obtained by making an ansatz $\vec{A}(x,t) = \vec{A}_0 \sin[k_0 x - \omega_0 t] \hat{y}$ and integrating the equation 2.17 with respect to time.

$$\vec{v}_e(x,t) = \frac{eA_0}{m_e} \sin[k_0 x - \omega_0 t] \hat{y}; \quad \vec{y}(x,t) = \frac{eA_0}{\omega_0 m_e} (1 - \cos[k_0 x - \omega_0 t]) \hat{y} \quad (2.18)$$

These equations describe the motion of an electron under the influence of a weak EM-field for which $v_e \ll c$. Equation 2.18 shows that the electron undergoes a harmonic oscillation in the y-direction centered around $eA_0/\omega_0 m_e$, whereas its position along the x-axis remains unchanged. The phase relationship between the motion of the electron and the applied \mathcal{E} -field component of the electro-magnetic field is shown in fig. 2.3a, where it can be seen that the electron's displacement is in phase with the \mathcal{E} -field, whereas its velocity is 90° out of phase.

2.3.2 Relativistic Case

For increasing laser intensities, the electron's velocity approaches the speed of light ($v_e \approx c$), the \mathcal{B} -field contribution to the electron's motion is comparable to its \mathcal{E} -field counterpart and relativistic corrections need to be made in the electron's equation of motion. Therefore, both the \mathcal{B} -field contribution and γ_e cannot be neglected anymore. By integrating the x and y components of the electron's equation of motion 2.16, the following two invariants can be obtained:

$$\tilde{p}_y - a = C_1; \quad \gamma_e - \tilde{p}_x = C_2 \quad (2.19)$$

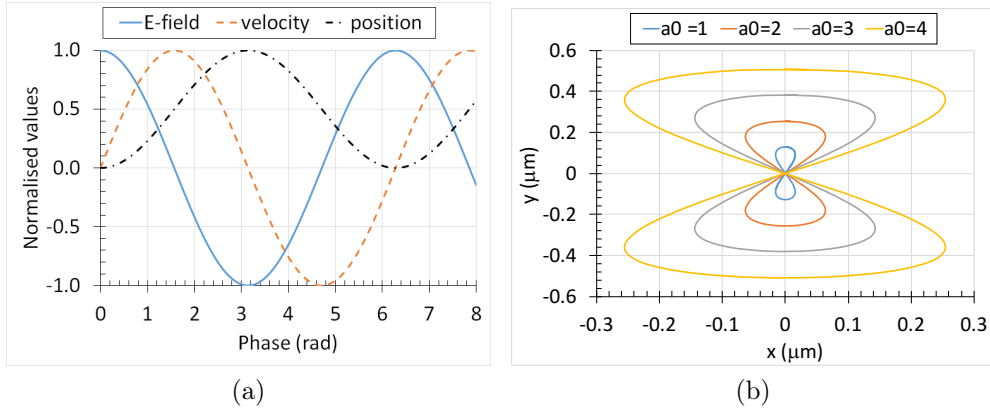


Figure 2.3: (a) Phase relationship among the \mathcal{E} -field, electron's oscillation velocity (\vec{v}_e), and its transverse motion (\vec{y}) for non-relativistic EM-field strengths, and (b) figure '8' motion of a relativistic electron in the co-moving reference frame with drift velocity (v_{df}) for $a_0 = 1, 2, 3, 4$ oscillating with the laser frequency ω_l .

where, the momentum components \tilde{p}_x and \tilde{p}_y are normalised to $m_e c$, and $a = eA/m_e c^2 = a_0 \sin[k_0 x - \omega_0 t]$, where $a_0 = eA_0/m_e c^2$ is defined as the normalised vector potential of the laser pulse. For an electron initially at rest at the origin, the constants C_1 and C_2 correspond to 0 and 1, respectively. In the co-moving reference frame of the laser pulse* ($\tau = t - x/c$), equation 2.19 can be integrated to obtain the motion of an electron in a strong EM-field⁵⁹.

$$x(\tau) = \frac{c}{4} a_0^2 \left[\tau - \frac{1}{2\omega_l} \sin(2\omega_l \tau) \right]; \quad y(\tau) = \frac{c}{\omega_l} a_0 [1 - \cos(\omega_l \tau)]; \quad z(\tau) = 0 \quad (2.20)$$

They show that the transverse motion $y(\tau)$ is still a purely oscillating term (similar to the classical solution equation 2.18), whereas $x(\tau)$ denotes a combination of oscillation with double the frequency and translation with a drift velocity $v_{df} = ca_0^2/(a_0^2 + 4)$. Thus, in its co-moving reference frame ($v_{df} = 0$), the electron performs the figure-8 motion shown in figure 2.3b. It is important to note that there is no net energy gain by the electron from the laser field according to the *Lawson-Woodward theorem*^{60;61}.

2.4 Ponderomotive Force

The analysis that so far has been carried out assumes a EM-field of constant amplitude (infinitely long plane wave) around the vicinity of the electron. This is, however, inadequate

*No explicit Lorentz transform is carried out here, as the length scales are kept the same both in the co-moving and lab reference frames

to understand as to what happens to an electron present in an inhomogeneous EM-field ($\vec{\mathcal{E}}(\vec{y}, t) = \vec{\mathcal{E}}_s(\vec{y}) \cos[\omega_0 t]$) like in the case of a tightly focused laser pulse. This can be overcome by investigating the equation of motion of the electron 2.15 in its non-relativistic form using a Taylor expanded \mathcal{E} -field $\vec{\mathcal{E}}_s(\vec{y})$ that accounts for its spatial inhomogeneity in the following way,

$$\vec{\mathcal{E}}_s(\vec{y}) = \underbrace{\vec{\mathcal{E}}_s(\vec{y})|_{\vec{y}_0}}_{1^{st}\text{-order}} + \underbrace{(\Delta\vec{y} \cdot \nabla)\vec{\mathcal{E}}_s(\vec{y})|_{\vec{y}_0}}_{2^{nd}\text{-order}} + \dots \quad (2.21)$$

where $\Delta\vec{y} = \vec{y}_1 - \vec{y}_0$. Taking into account only the 1th-order term, for an electron initially at the origin ($y_0 = 0$), its velocity (\vec{v}_1) and displacement (\vec{y}_1) can be by obtained by integrating the equation 2.15.

$$\vec{v}_1 = -\frac{e}{m_e \omega_0} \vec{\mathcal{E}}_s(\vec{y}_0) \sin[\omega_0 t]; \quad \Delta\vec{y} = \vec{y}_1 = \frac{e}{m_e \omega_0^2} \vec{\mathcal{E}}_s(\vec{y}_0) \cos[\omega_0 t] \quad (2.23)$$

These equations describe the oscillatory motion of an electron acted upon by a uniform \mathcal{E} -field $\vec{\mathcal{E}}_s(\vec{r}_0)$. The contribution of the \mathcal{E} -field inhomogeneity can be obtained by revisiting equation 2.15 and considering only the motion resulting the non-uniform \mathcal{E} -field and $\vec{v}_1 \times \vec{\mathcal{B}}$ components, as shown below,

$$m_e \frac{d\vec{v}_2}{dt} = -e \left[(\vec{y}_1 \cdot \nabla) \vec{\mathcal{E}}(\vec{y}_1, t)|_{\vec{y}_0} + \vec{v}_1 \times \vec{\mathcal{B}}(\vec{y}_1, t) \right] \quad (2.24)$$

The force component resulting from the \mathcal{B} -field ($\vec{v}_1 \times \vec{\mathcal{B}}$) is taken into account, as it is of the same expansion order as the non-uniform \mathcal{E} -field contribution. Time averaging over the fast oscillations of the laser-field and making use of equations 2.23, the expression 2.24 can be reduced to⁶²:

$$\mathbf{F}_{pond} = m_e \left\langle \frac{d\vec{v}_2}{dt} \right\rangle_T = -\frac{e^2}{4m_e \omega_0^2} \nabla(\vec{\mathcal{E}}_s^2) \quad (2.25)$$

This expression shows that in the case of a non-uniform electro-magnetic field, there is a net force acting on the electron from the regions of high to low intensities. This is the so-called ponderomotive force (\mathbf{F}_p), which can be viewed as the force resulting from the light pressure difference acting on the electron. The ponderomotive force can be written in terms of a potential Φ_p such that $\mathbf{F}_p = -\nabla\Phi_p$ in which Φ_p can be equated to the average kinetic energy gained by the electron from the laser field, as shown below

$$\Phi_p = \frac{e^2}{4m_e \omega_0^2} \vec{\mathcal{E}}_s^2 \equiv \frac{1}{2} m_e \langle \vec{v}_0 \rangle^2 \quad (2.26)$$

which can also be verified from equation 2.23 (for \vec{v}_1). For electron velocities close to the speed of light ($v_0 \approx c$), a similar expression can be derived using the relativistic equation of motion of the electron^{63;64}.

$$\vec{F}_p = -\nabla\Phi_p = -\frac{e^2}{4\langle\gamma_e\rangle m_e \omega_0^2} \nabla(\mathcal{E}_s^2) \quad (2.27)$$

where $\langle\gamma_e\rangle$ is the electron's time-averaged Lorentz factor. This shows that the ponderomotive force is proportional to the intensity of the laser pulse (through \mathcal{E}_s^2) and acts independently of the sign of the charge. Neglecting the charge dependence, the force exerted on an electron is however much greater than that on an ion due to the mass dependence in equation 2.27, as ions are much heavier than electrons.

In the case of plasma, where the collective oscillations of its constituent electron population need to be taken into account, the ponderomotive force is balanced by the restoring electrostatic force offered by the ion population. Therefore, one can no longer ignore the electrostatic potential (V) in the Coulomb gauge of the electric field $\vec{\mathcal{E}} = -\partial\vec{A}/\partial t - \nabla V$. Therefore, the corresponding expression for the ponderomotive force is given by⁶⁵,

$$\vec{F}_p = -\nabla\Phi_p = -m_e c^2 \nabla(\gamma_e - 1) \quad (2.28)$$

where $\gamma_e = \sqrt{1 + a^2}$ in the case of plasma (many electron system). Please note that this differs from the case of a single electron in a linearly polarised EM-field, for which $\gamma_e = (1 + a^2/2)^{1/2}$. Since the energy gained by an electron in a non-uniform laser field depends on its starting position, the maximum energy gain is achieved for an electron present at the centre of the focus, where the \mathcal{E} -field is maximum. Therefore, the maximum ponderomotive potential is given by,

$$\Phi_p = m_e c^2 \left(\sqrt{1 + a_0^2} - 1 \right) = 0.511 \left(\sqrt{1 + a_0^2} - 1 \right) \text{ MeV} \quad (2.29)$$

The amplitude of the normalised vector potential a_0 can be related to the laser's peak intensity I_0 in the following way:

$$I_0 = \frac{1}{2} \epsilon_0 c E_0^2 = 2\pi^2 \epsilon_0 c^5 \left(\frac{m_e a_0}{e \lambda_0} \right)^2 \Rightarrow a_0 = \sqrt{\frac{(I_0/\text{Wcm}^{-2})(\lambda_0/\mu\text{m})^2}{1.37 \times 10^{18}}} \quad (2.30)$$

For instance, for a peak laser intensity I_0 of $4 \times 10^{19} \text{ W/cm}^2$ and central laser wavelength λ_0 of $0.8 \mu\text{m}$, the normalised vector potential $a_0 = 4.8$ corresponding to a ponderomotive potential or the average kinetic energy gained by the electron $\Phi_p = 2 \text{ MeV}$. Thus, the electron gains energy from the laser-field in contrast to Lawson-Woodward theorem^{60;61}. For a given laser parameters, such as its energy, pulse duration and focusing geometry, electrons can be accelerated to energies greater than the maximum ponderomotive potential in an under-dense plasma, if the collective plasma oscillations are to be utilised in the acceleration process, as discussed in section 2.7.

2.5 Plasma Properties

The propagation of a laser pulse in a plasma is primarily determined by the plasma electrons' response to the electro-magnetic field of the laser pulse, as their counterparts, namely the ions are much heavier. Any effect on the ion population could thus be deemed as a secondary effect resulting from the displacement of the energetic electrons driven by the laser pulse. Therefore, in this section, the basic properties of the plasma associated with its electron population are first described, which is then followed by its response during the propagation of an intense laser pulse.

Plasma Frequency

The plasma frequency is defined as the frequency with which its constituent electrons collectively respond to any external disturbance and is expressed in terms of the electron density n_e by⁵⁹,

$$\omega_p = \sqrt{\frac{n_e e^2}{\varepsilon_0 m_e}} \quad (2.31)$$

where, e is the electron charge, ε_0 is the vacuum permittivity and m_e is the electron rest mass. At relativistic intensities, the oscillation velocity of an electron in laser field approaches the speed of light. Therefore, the plasma frequency needs to be accordingly modified to $\omega_{rp}^2 = \omega_p^2 / \langle \gamma_e \rangle$, where $\langle \gamma_e \rangle$ is the time-averaged Lorentz factor related to the electron's motion. Furthermore, when one takes into account the thermal motion of the electrons, the dispersion relation for the collective plasma oscillations is given by the so-called Bohm-Gross relation⁶⁶,

$$\omega_{ek}^2 = \omega_p^2 + 3v_{th}^2 k^2 \quad (2.32)$$

where the electron thermal velocity $v_{th} = \sqrt{k_B T_e / m_e}$ with k_B being the Boltzmann constant, T_e being the electron temperature and k being the wave number. The k dependence in equation 2.32 implies the propagation of the electron density oscillations essentially due to the thermal effects (i.e. the propagation will not occur in the absence of the thermal effects).

Critical Density

The propagation of a laser pulse in a plasma medium is restricted up to a density at which the plasma frequency equals the laser frequency i.e., $\omega_p = \omega_0$, which is defined as the critical density (n_c). It can be quantified as

$$n_c = \frac{\varepsilon_0 m_e \omega_0^2}{e^2} = \frac{1.1 \times 10^{21} \text{ cm}^{-3}}{(\lambda_0 / \mu\text{m})^2} \quad (2.33)$$

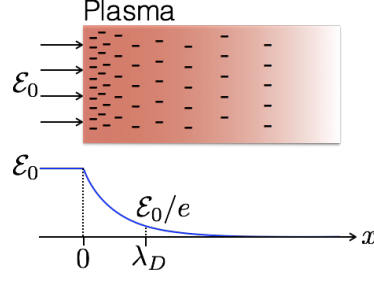


Figure 2.4: Shielding of an external applied \mathcal{E} -field by the plasma, where the \mathcal{E} -field ($\mathcal{E} = -\nabla\phi(x)$) drops exponentially inside the plasma shielding region.

Since the interaction dynamics between an intense laser pulse and the plasma medium is primarily determined by its density, it is meaningful to characterise it as *under-dense* if $n_e \ll n_c$, *near-critical* if $0.1n_c < n_e < n_c$ and *over-critical* if $n_e > n_c$. However, for relativistic intensities, the critical density is increased to $n_c\langle\gamma_e\rangle$.

Debye Length

The Debye length (λ_D) of a plasma is defined as the distance over which an externally applied \mathcal{E} -field is reduced by a factor of $1/e$.¹⁴ When an external \mathcal{E} -field is applied to a plasma with a finite electron temperature (T_e), its electron population at the plasma boundary collectively responds to shield it from the rest of the plasma, as shown in fig. 2.4. Within the distances over which the shielding is achieved, the neutrality of the plasma is not fulfilled i.e. there is a net charge. For a plasma with an exponential electron energy distribution (i.e. $f(v_e) \propto \exp[-v_e^2/v_0^2]$, where $f(v_e)$ is the electron velocity probability distribution function, v_e is the electron velocity and v_0 is the equilibrium electron thermal velocity), the variation of the potential inside the shielding region is given by¹⁴,

$$\phi(x) = \phi_0 \exp\left[-\frac{x}{\lambda_D}\right], \quad \text{where} \quad \lambda_D = \sqrt{\frac{\varepsilon_0 k_B T_e}{e^2 n_{e0}}} \quad (2.34)$$

where ϕ_0 is the amplitude of the potential, which depends on the applied \mathcal{E} -field, x is the distance measured from the plasma boundary, and n_{e0} is the steady state electron density. Here, the mobility of the ions is neglected, as they are much heavier than the electrons i.e. $m_i \gg m_e$, where m_i is the ion mass and m_e is the electron mass. However, in the steady state limit, if the contribution of the ions is to be taken into account, the Debye length is reduced by a factor of⁶⁷ $\sqrt{2}$. Equation 2.34 shows that higher electron temperatures result in larger shielding lengths, due to reduced confinement of these electrons to the region where the potential is applied. For a given T_e , higher electron densities result in shorter shielding lengths, as there are more electrons with lower velocities available.

2.6 Laser Propagation in Plasma Medium

The propagation of electro-magnetic waves in plasma can be described by the Maxwell equations in matter of the form:⁴⁵

$$(i) \nabla \cdot \vec{\mathcal{E}} = -\frac{1}{\varepsilon_0} \nabla \cdot \vec{P} + \rho_f, \quad (ii) \nabla \cdot \vec{\mathcal{B}} = 0 \quad (2.35)$$

$$(iii) \nabla \times \vec{\mathcal{E}} = -\frac{\partial \vec{\mathcal{B}}}{\partial t}, \quad (iv) \nabla \times \vec{\mathcal{B}} = \mu \left(\varepsilon_0 \frac{\partial \vec{\mathcal{E}}}{\partial t} + \frac{\partial \vec{P}}{\partial t} + \vec{J}_f \right) \quad (2.36)$$

where $\vec{\mathcal{E}}(x,t)$ and $\vec{\mathcal{B}}(x,t)$ are the \mathcal{E} and \mathcal{B} -fields of EM-wave, ρ_f is the charge distribution density, $\vec{P}(x,t)$ is the material (plasma) polarisation, μ is the magnetic permeability ($\mu \approx \mu_0$) and the total current $\vec{J} = (\partial \vec{P} / \partial t) + \vec{J}_f$ with $\partial \vec{P} / \partial t$ being the bound current and \vec{J}_f being the free current in plasma. By setting $\rho_f = 0$ and $\vec{J}_f = 0$, plasma can be treated as a dielectric medium, where only the transverse oscillations of the electrons in the EM-field are considered.

By taking the time derivative of equation 2.35(ii) and substituting 2.35(i) in (ii), one can obtain the following expression,

$$\nabla^2 \vec{\mathcal{E}} - \frac{1}{c^2} \frac{\partial^2 \vec{\mathcal{E}}}{\partial t^2} = \frac{1}{\varepsilon_0} \left(\frac{1}{c^2} \frac{\partial^2 \vec{P}}{\partial t^2} - \nabla(\nabla \cdot \vec{P}) \right) \quad (2.37)$$

where $c = 1/\sqrt{\mu_0 \varepsilon_0}$. Considering only the transverse motion of the electrons, the divergence term $\nabla \cdot \vec{P}$ can be set to zero. Assuming that the plasma electrons respond instantaneously to the applied \mathcal{E} -field $\vec{\mathcal{E}}(t)$ ⁶⁸, the polarisation \vec{P} can in general be expanded in terms of $\vec{\mathcal{E}}$ to account for the non-linear response of plasma, as follows^{69;70},

$$\vec{P}(t) = \varepsilon_0 \sum_{n=1}^{\infty} \chi_{ij}^{(n)}(t, \vec{\mathcal{E}}) \vec{\mathcal{E}}(t) = \varepsilon_0 \left(\chi_{ij}^{(1)} + \chi_{ij}^{(2)}(t, \vec{\mathcal{E}}) + \chi_{ij}^{(3)}(t, \vec{\mathcal{E}}^2) + \dots \right) \vec{\mathcal{E}}(t) \quad (2.38)$$

where the proportionality constant $\chi_{ij}^{(1)}$ is the first-order electric susceptibility, which depends on the microscopic structure of the material⁴⁵ (i.e. plasma). Whereas, the higher order electric susceptibilities ($\chi_{ij}^{(2)}, \chi_{ij}^{(3)} \dots$) depend also on the applied \mathcal{E} -field to varying orders.

2.6.1 Linear Response

The first order susceptibility $\chi_{ij}^{(1)}$ corresponds to the linear response of plasma, which is independent of the applied \mathcal{E} -field. Therefore, the plasma polarisation can be shown to

be directly proportional to the applied \mathcal{E} -field i.e. $\vec{P} = \varepsilon_0 \chi^{(1)} \vec{\mathcal{E}}$. For a purely transverse plasma response, the time derivative of the bound current $\partial \vec{P} / \partial t$ is given by,

$$\frac{\partial^2 \vec{P}}{\partial t^2} = \varepsilon_0 \chi^{(1)} \frac{\partial^2 \vec{\mathcal{E}}}{\partial t^2} \quad (2.39)$$

substituting equation 2.39 in 2.37 and setting $\nabla \cdot \vec{P} = 0$, one can obtain the following wave equation of the form:

$$\nabla^2 \vec{\mathcal{E}} = \frac{1 + \chi^{(1)}}{c^2} \frac{\partial^2 \vec{\mathcal{E}}}{\partial t^2} = \left(\frac{\eta}{c}\right)^2 \frac{\partial^2 \vec{\mathcal{E}}}{\partial t^2} \Rightarrow \boxed{\nabla^2 \vec{\mathcal{E}} = \frac{1}{v^2} \frac{\partial^2 \vec{\mathcal{E}}}{\partial t^2}} \quad (2.40)$$

where the refractive index $\eta = (1 + \chi^{(1)})^{1/2}$ and the propagation velocity $v = c/\eta$. Thus, the propagation of an EM-wave in plasma satisfies the wave equation of the form 2.40.

Refractive Index

The bound current $\partial \vec{P} / \partial t$ can be expressed in terms of the transverse electron density oscillations \vec{v}_e such that $\partial \vec{P} / \partial t = -en_e \vec{v}_e$. By taking its time derivative and equating it with equation 2.39, one obtains the following relation⁷¹,

$$\frac{\partial^2 \vec{P}}{\partial t^2} = -en_e \frac{\partial \vec{v}_e}{\partial t} \equiv \varepsilon_0 \chi^{(1)} \frac{\partial^2 \vec{\mathcal{E}}}{\partial t^2} \quad (2.41)$$

where n_e is plasma electron density and \vec{v}_e is the electrons' transverse oscillation velocity. By making use of the electron's (non-relativistic) equation of motion: $\partial \vec{v}_e / \partial t = -e\vec{\mathcal{E}}/m_e$ and $\vec{\mathcal{E}} = \vec{\mathcal{E}}_0 \exp[i(\omega t - kx)]$, equation 2.41 yields the expression for the electric susceptibility $\chi^{(1)}$, which is given by,

$$\chi^{(1)} = -\frac{e^2 n_e}{m_e \varepsilon_0 \omega^2} = -\frac{\omega_p^2}{\omega^2} \quad (2.42)$$

where the plasma frequency $\omega_p = e^2 n_e / m_e \varepsilon_0$. Thus, for a laser pulse with a given spectral width, the plasma refractive index η corresponding to its central frequency (i.e. $\omega = \omega_0$) can be expressed as,

$$\eta = \frac{c}{v} = \left(1 - \frac{\omega_p^2}{\omega_0^2}\right)^{1/2} = \left(1 - \frac{n_e}{n_c}\right)^{1/2} \quad (2.43)$$

where the critical plasma density $n_c = \varepsilon_0 m_e \omega_0^2 / e^2$.

Phase Velocity and Dispersion Relation

For a plane wave ansatz of the form $\vec{\mathcal{E}} = \vec{\mathcal{E}}_0 \exp[i(\omega t - kx)]$ with ω being the frequency and k being the wave number, the wave equation 2.40 yields $v = \omega/k$, which is defined as the phase velocity (v_{ph}) of the wave. Whereas, the corresponding dispersion relation of an electro-magnetic wave propagating in plasma can be obtained by making use of the relation $v_{ph}^2 = c^2\omega^2/(\omega^2 - \omega_p^2)$ (obtained from eqn. 2.43), as follows,

$$\omega^2 = \omega_p^2 + c^2k^2 \quad (2.44)$$

where the plasma frequency ω_p is the minimum frequency of an EM-wave that can still propagate in a plasma.

Group Velocity

Since a (Gaussian) laser pulse can be decomposed into several monochromatic waves of differing frequencies, it is also bound to satisfy the wave equation 2.40. In a medium, where the refractive index experienced by the laser pulse is frequency dependent, each of its frequency component travels at a different phase velocity leading to changes in the temporal structure of the laser pulse. This effect is known as *dispersion*. Therefore, it can be expected that the velocity with which the laser pulse's envelope moves differs from that of its central frequency, which can be understood through the following analysis.

Considering the overlap of the two monochromatic waves of the same amplitude with slightly differing frequencies ($\omega \pm \Delta\omega$) and wave numbers ($k \pm \Delta k$), the resulting \mathcal{E} -field is given by⁷²,

$$\vec{\mathcal{E}} = \vec{\mathcal{E}}_0 \exp[i([\omega + \Delta\omega]t - [k + \Delta k]z)] + \vec{\mathcal{E}}_0 \exp[i([\omega - \Delta\omega]t - [k - \Delta k]z)] \quad (2.45)$$

The real-part of the resultant \mathcal{E} -field can be expressed as,

$$\vec{\mathcal{E}} = 2\vec{\mathcal{E}}_0 \cos[\omega t - kz] \cos[\Delta\omega t - \Delta kz] \quad (2.46)$$

Here, the first cosine term refers to a plane wave with a phase velocity $v_{ph} = \omega/k$, whereas the second cosine term refers to a modulation of $2\pi/\Delta k$ wavelength travelling at a velocity of v_{gr} :

$$\frac{\Delta\omega}{\Delta k} \approx \frac{\partial\omega}{\partial k} = v_{gr} \quad (2.47)$$

This analysis can be likewise extended to include a lot more frequencies that make up a laser pulse. Hence, the group velocity v_{gr} refers to the velocity with which the envelope of the laser pulse moves in the medium, which can be related to the refractive index η using the dispersion relation $\omega^2 = \omega_p^2 + c^2k^2$, as follows,

$$v_{gr} = \frac{\partial\omega}{\partial k} = \frac{kc^2}{\sqrt{\omega_p^2 + c^2k^2}} = c \frac{c}{\omega/k} = c\eta \quad (2.48)$$

Further Comments

For $n_e/n_c < 1$, the expression for the refractive index 2.43 yields $\eta < 1$ indicating that the phase velocity $v_{ph} > c$. It should however be noted that the speed with which information or energy travels in plasma is rather given by the group velocity v_{gr} , which is smaller than c (for $v_{gr} = c\eta$) in accordance with the relativity theory⁷³.

For laser intensities at which the electron's oscillation velocity approaches the speed of light c in vacuum, the plasma frequency ω_p needs to be accordingly modified to account for the relativistic increase in the electron's mass, which is given by⁷⁴ $\omega_{rp} = \omega_p/\sqrt{\langle\gamma_e\rangle}$, where $\langle\gamma_e\rangle$ is the electron's time-averaged relativistic factor. This leads to an induced transparency whereby the laser can propagate up to an enhanced critical density of $\langle\gamma_e\rangle n_c$. Thus, the plasma refractive index can be accordingly modified to:

$$\eta = \sqrt{1 - \frac{\omega_p^2}{\langle\gamma_e\rangle\omega_0^2}} = \sqrt{1 - \frac{n_e}{\langle\gamma_e\rangle n_c}} \quad (2.49)$$

2.6.2 Nonlinear Response

The nonlinear response of the plasma to the applied \mathcal{E} -field can be examined with the help of the refractive index expression shown in eqn. 2.49, where the time-averaged Lorentz factor $\langle\gamma_e\rangle = (1 + a_0^2)^{1/2}$ accounts for the intensity dependent laser propagation effects, such as relativistic self-focusing and self-phase modulation (to be discussed in section 2.9). If one considers the propagation of a laser pulse in a gas medium, where the laser pulse's intensity is high enough to ionise the constituent atoms, the intensity dependent temporal variation of the refractive index $\eta(t, I)$ at a given spatial location is given by,

$$\eta(t, I) = \sqrt{1 - \frac{n_e(t, I)}{\gamma_e(I(t))n_c}}, \quad \text{where} \quad n_e(t, I) = n_e \left(\max_{t' < t} [I(t')] \right) \quad (2.50)$$

which means that for a given time t , the electron density n_e depends on the laser's maximum intensity for times before time t (i.e. $t' < t$). This is valid under the assumption that the electron-ion recombination times are much longer than the laser pulse's time scale, which is usually in the range of a few milliseconds^{75;76} and the electron expulsion due to the ponderomotive force of the laser pulse is negligible.

2.7 Laser Wakefield Acceleration

When an intense laser pulse propagates through plasma, its ponderomotive force serves as a means of radially displacing the electrons from the (heavier) ionic background. These electrons are, however, pulled back by the restoring force offered by the quasi-static ionic

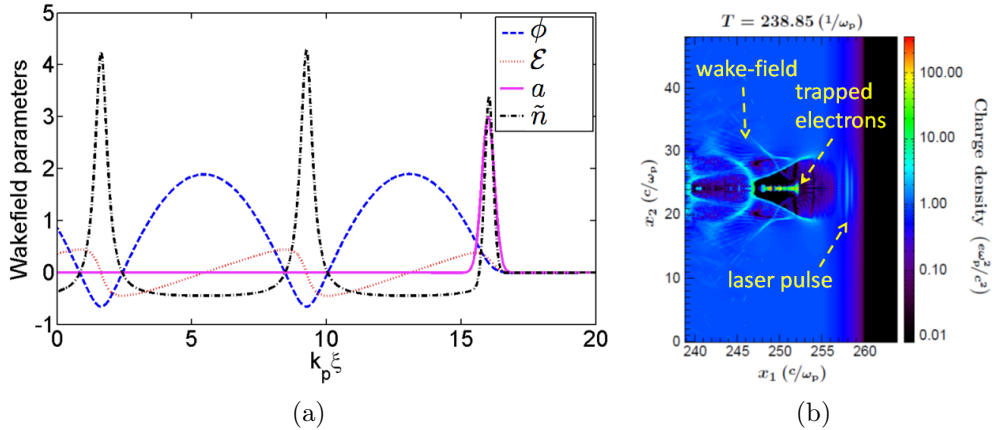


Figure 2.5: (a) Normalised wakefield parameter, namely the electron density perturbation ($\tilde{n} = n'_e/n_e$, where n'_e is the perturbed electron density and n_e the uniform electron density that one starts off with) at the trail of the laser pulse, the resulting nearly linear longitudinal \mathcal{E} -field ($\tilde{\mathcal{E}} = e\mathcal{E}_l/mc^2\omega_0$) due to the charge separation between the electrons and the ions, the corresponding electro-static potential ($\phi = e\Phi/mc^2$), and vector potential of the laser pulse ($a = eA/mc^2$) for a peak value of $a_0 = 3$ and uniform plasma-density $n_e = 0.08n_c$, and (b) 3D PIC simulation result showing wakefield excitation and trapped electrons in the wake⁹⁰.

background, thus setting up an electron density oscillations at the trail of the laser pulse, which is called a plasma wave. If electrons can be trapped inside such spatio-temporal density oscillations (like a surfer catching an ocean wave), they can be accelerated to a few GeV energies due to the longitudinal electric field offered by the charge separation over a few centimetre scale lengths¹⁵. Electrons can be trapped in a plasma wave using methods, such as wake breaking^{17;19–21}, colliding pulse (through beat wave)^{77–80}, ionization induced^{81–83}, shock wave^{84;85}, density-ramp injection⁸⁶ and external injection⁸⁷.

Figure 2.5a shows the excitation of the electron density oscillations at the trail of the laser pulse and the resulting nearly linear longitudinal electric-field due to the charge separation, which can be calculated using a 1D model of the laser wakefield⁸⁸. As the electrons gain energy from the wakefield, they begin to outrun the wakefield and enter into a dephasing region, where the longitudinal \mathcal{E} -field of the wake reverses its direction and begins to decelerate the electrons. Thus, the length after which the electrons enter the deceleration phase is defined as the dephasing length (l_{dp}) and it is quantified by⁸⁹ $l_{dp} = \lambda_p^3/\lambda_0^2$, where λ_0 is the laser wavelength and λ_p is the plasma-wavelength, which for plasma wave's phase velocities close to c is given by $\lambda_p = 2\pi c/\omega_p$. The laser wakefield acceleration process is most efficient when the longitudinal spatial extent of the laser pulse matches with half of the plasma wavelength⁶² i.e. $c\Delta\tau \approx \lambda_p/2$.

A more detailed analysis of the wakefield acceleration can be carried out using Particle-

In-Cell (PIC) simulations, where the interaction between the laser pulse and the plasma medium are self-consistently solved and they can take into account the 3D shape of the plasma-wave, laser pulse's spatio-temporal evolution, energy depletion and various laser-plasma instabilities. Figure 2.5b shows the result obtained from such a PIC-simulation, where the laser pulse, plasma wave excitation and electrons that are trapped inside the wave are depicted⁹⁰. A more detailed discussion on this acceleration mechanism can be found in references^{91–93}. Laser wakefield acceleration has so far been extensively investigated both theoretically^{13;16–18;94;95} and experimentally^{15;19–22;79;84–86;88;96} and has been shown to dominate in the density region $n_e \lesssim 0.1n_c$ in which, electrons can be accelerated up to a few GeV's.^{88;97}

2.8 Direct Laser Acceleration (DLA)

As the plasma density n_e increases (still $< n_c$), both the dephasing length l_{dp} of the wakefield acceleration and the maximum obtainable electron energy E_{max} decrease, as it can be shown that⁸⁹ $l_{dp} \propto 1/n_e^{3/2}$ and $E_{max} \propto 1/n_e$. Furthermore, for increasing plasma densities, the damping of the plasma wave also starts to play a role⁹⁸. However, simulations have shown that laser-plasma interactions in this density regime give rise to an acceleration mechanism called direct laser acceleration (DLA), whereby electrons directly gain energy from the laser field^{31;32;38;39}. In this acceleration mechanism, the pulse duration of the laser plays a less crucial role than in the case of the laser wakefield acceleration⁸⁹.

Mechanism

During the interaction between an intense laser pulse and an under-dense plasma, electrons are expelled from its focal volume due to the ponderomotive force of the laser pulse. The electrons along the laser's propagation direction are continuously expelled by the laser pulse, whereas the radial expulsion of the electron is counteracted by the Coulomb attraction force resulting from the electron-ion charge separation leading to a channel-like structure. This results in a (quasi-static) \mathcal{E} -field pointing radially outwards inside the channel, as shown in fig. 2.6a. The current generated by the forward propagating electrons initially undergoes filamentation due to the Weibel instability^{99;100}, which is triggered e.g. by the perturbations in the transverse laser intensity distribution⁹⁸. For near-critical plasma densities, the self-generated \mathcal{B} -fields of the electron filaments are strong enough to pinch them together to eventually form one single filament (as shown in fig. 2.6b), which survives at time scales longer than the pulse duration³⁸. With the help of simulations, the radial extent of the filament has been shown to be of the order of the laser wavelength, in which the maximum B-field is reached at its radial boundary^{31;38}.

The electrons that are trapped inside the channel structure, undergo oscillatory motion

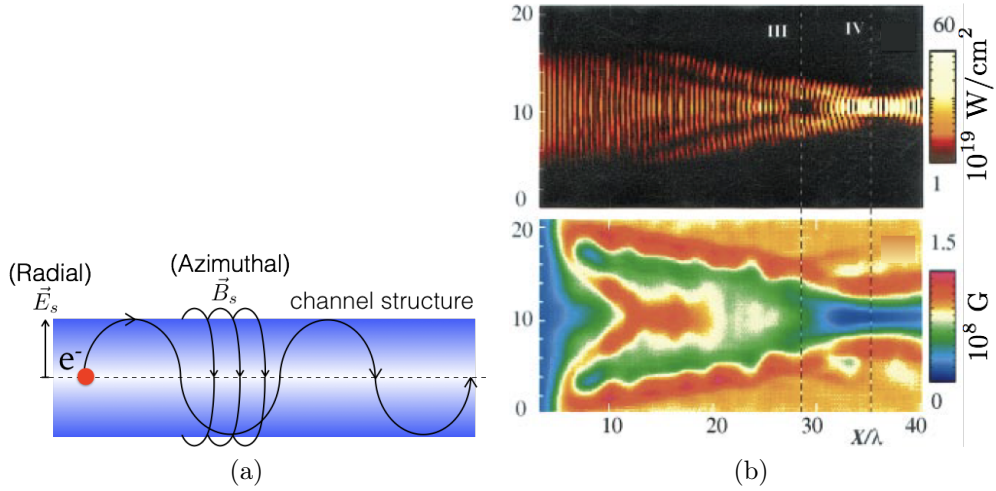


Figure 2.6: (a) Motion of an electron under the influence of transverse \mathcal{E} -field and self-generated \mathcal{B} -field of the channel structure, and (b) Simulation result for $a_0 = 3$ and $n_e/n_c = 0.36$ showing laser pulse propagation (from left to right), where the upper image shows the relativistic self-focusing of the laser pulse in terms of its intensity and the lower image shows the self-generated \mathcal{B} -field of the forward electron current³⁸. For comparison, the \mathcal{B} -field of the light-wave $\mathcal{B}_0 = m_e c \omega_0 / e = 134$ MG for $\lambda_0 = 2\pi c / \omega_0 = 0.8 \mu\text{m}$, whereas the simulation results yield a peak \mathcal{B} -field of 150 MG.

(betatron oscillation) within the channel structure due to the quasi-static \mathcal{E} and \mathcal{B} -fields acting on them^{101–108}, as shown in fig. 2.6a. When these oscillating electrons interact with a laser pulse, they can directly gain energy from the laser-pulse, if the electrons' betatron frequency matches with that of the laser's frequency, as seen by the electron in its own frame of reference. In this scenario, when the electron undergoes purely one transverse betatron oscillation, it is overtaken by the electromagnetic field exactly by one cycle. A more detailed discussion on this electron acceleration mechanisms can be found in the references^{32;38;39}. Similar to the laser wakefield acceleration process, electrons could also enter a deceleration phase if the oscillations of the electrons become out of phase with the laser \mathcal{E} -field. Simulations have reported both Maxwellian³² and quasi-monoenergetic⁴¹ electron energy spectra. The channel structure has been estimated to expand at pico-second timescales due to collisions³⁸. Furthermore, this acceleration mechanism has been shown to dominate at densities around³⁹ $n_e \sim 0.2n_c$, where a helium gas jet was used as a target.

2.9 Propagation Effects

When an intense laser pulse propagates through an under-dense plasma, depending on the local plasma density and laser intensity distribution, the laser pulse could experience various propagation effects, such as ionization induced defocusing, relativistic and ponderomotive self-focusing, self-phase modulation and pulse compression. The refractive index of the plasma η , as a function of the electron density n_e and the electron's relativistic factor $\langle\gamma_e\rangle$ is given by,

$$\eta = \sqrt{1 - \frac{n_e}{\langle\gamma_e\rangle n_c}} \quad (2.51)$$

where $\langle\gamma_e\rangle = \sqrt{1 + a_0^2}$ with a_0 being the normalised vector potential of the laser pulse and plasma's critical-density $n_c = \varepsilon_0 m_e \omega_0^2 / e^2$ with ω_0 being the laser's central frequency. The propagation effects can be studied by introducing perturbations in the plasma density $n'_e = n_e + \delta n_e$ and laser's central frequency $\omega'_0 = \omega_0 + \delta\omega_0$, where $\delta n_e \ll n_e$ and $\delta\omega_0 \ll \omega_0$, in the linearly approximately version of the refractive index of the plasma, which is only valid for under-dense plasma (i.e. $n_e \ll n_c$), as follows,

$$\eta \approx 1 - \frac{1}{2} \frac{e^2}{\varepsilon_0 m_e} \frac{1}{\sqrt{1 + a_0^2}} \frac{n_e + \delta n_e}{(\omega_0 + \delta\omega_0)^2} \quad (2.52)$$

For $a_0 < 1$, the inverse of the Lorentz factor $1/\langle\gamma_e\rangle \approx 1 - a_0^2/2$ and the expression above can be approximated to^{109;110}:

$$\eta = 1 - \frac{1}{2} \frac{\omega_p^2}{\omega_0^2} \left(1 + \frac{\delta n_e}{n_e} - \frac{2\delta\omega_0}{\omega_0} - \frac{a_0^2}{2} \right) \quad (2.53)$$

whereas for $a_0 > 1$, $1/\langle\gamma_e\rangle \approx (1/a_0)(1 - 1/2a_0^2)$. Thereby,

$$\eta = 1 - \frac{1}{2} \frac{\omega_p^2}{\omega_0^2 a_0} \left(1 + \frac{\delta n_e}{n_e} - \frac{2\delta\omega_0}{\omega_0} - \frac{1}{2a_0^2} \right) \quad (2.54)$$

Thus, the dependence of η on δn_e , $\delta\omega_0$ and a_0 leads to a number of effects, which affect the laser pulse during its propagation, which could compete with one another depending on their exact values, orientations and strengths. The following section gives a simplified semi-quantitative account of these different effects, where they are treated independently and any combination of the propagation effects are ignored, whereas as an exact analysis would require detailed computer simulations.

2.9.1 Ionisation Induced Defocusing

Considering the propagation of a laser pulse in an argon gas jet, for (non-relativistic) intensities exceeding the ionisation threshold of the argon atoms, the ionisation process

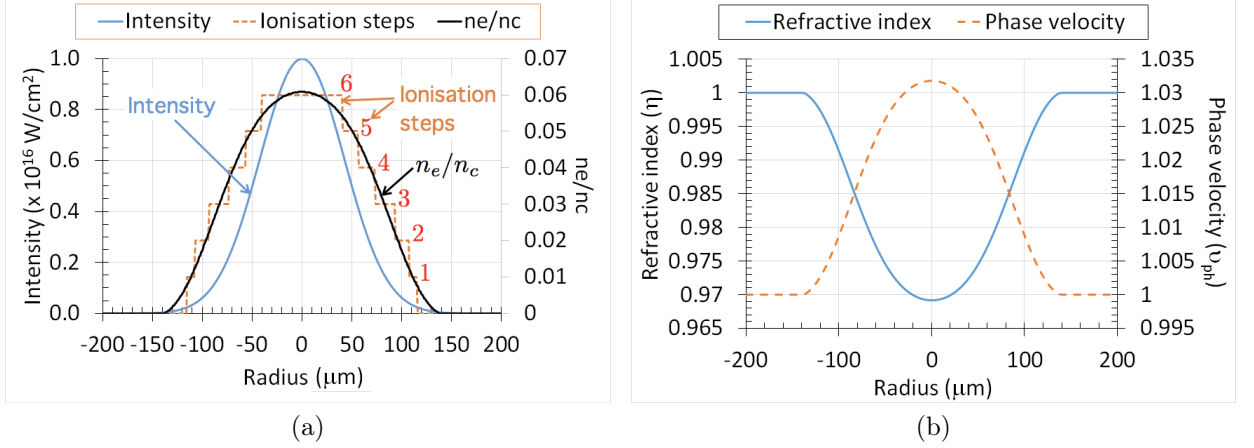


Figure 2.7: (a) Gaussian shaped radial intensity distribution of a focused laser pulse and the corresponding intensity dependent step-line vs smooth plasma density profile. Here, the transition of the argon ionisation states is assumed to be smooth, where the corresponding plasma density is interpolated between the values corresponding to the two successive ionisation states. (b) Associated plasma refractive index ($\eta(r)$) and laser phase velocity (v_{ph}).

leads to a reduction in refractive index (η), as $\eta = (1 - n_e/n_c)^{1/2}$. As the refractive index contribution of the free electrons present in the plasma is much higher than that of their atomic counterpart[†], any further propagation of the laser pulse is primarily determined by the plasma's electron density distribution. Figure 2.7a shows the radial intensity distribution of a Gaussian laser pulse and the resulting electron density distribution corresponding to various argon ionisation levels. Its corresponding plasma refractive index (η) and laser's phase velocity (v_{ph}) profiles are shown in fig. 2.7b, which is equivalent to that of a negative lens. Thus, for a plane wave, an increased v_{ph} in the middle causes the radius of curvature of the laser pulse to increase leading to a defocusing effect. In the case of a wave front that is being focused, this causes first a decrease and then an increase in its radius of curvature. Further propagation of the laser pulse continues to be dominated by the defocusing effect, as long as its intensity exceeds the ionisation threshold.

Formulation

The propagation characteristics of a laser pulse affected by ionisation induced defocusing can be examined by considering the case of a Gaussian beam with beam waist w_0 , as shown

[†]For example, at atmospheric pressure, the refractive index contribution of air $\Delta\eta_{Air} = 0.0003$ corresponding to a number density of $2.5 \times 10^{19} \text{ cm}^{-3}$. Whereas, a plasma with the same electron density yields a refractive index contribution $\Delta\eta = 0.008$, which can further be enhanced through multiple ionisation process.

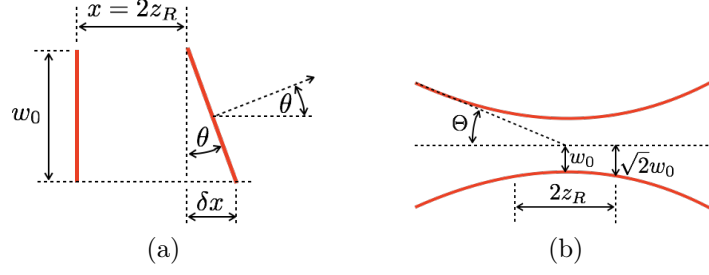


Figure 2.8: (a) Tilting of a flat wavefront of width w_0 after a propagation distance x , and the propagation of a Gaussian beam with a divergen half-angle Θ .

in fig. 2.8a. After a propagation distance of x and time t , the wavefront is shown to have tilted by an angle θ due to ionisation induced defocusing, where the on-axis propagation velocity v'_{ph} is different from that of the edge v_{ph} , which is given by,

$$x = v_{ph}t = \frac{c}{\eta} t = \frac{c}{\sqrt{1 - (n_e/n_c)}} t \approx c \left(1 + \frac{1}{2} \frac{n_e}{n_c} \right) t \quad (2.55)$$

whereas the on-axis distance x' due to the electron density $n_e + \delta n_e$, is given by,

$$x' = v'_{ph}t = \frac{c}{\sqrt{1 - ((n_e + \delta n_e)/n_c)}} t \approx c \left(1 + \frac{1}{2} \frac{n_e}{n_c} + \frac{1}{2} \frac{\delta n_e}{n_c} \right) t \quad (2.56)$$

$$\approx x + c \frac{\delta n_e}{2n_c} t = x + \delta x \quad (2.57)$$

where $\delta x = c\delta n_e t / 2n_c$. Thus, the tilting angle θ for small values is given by,

$$\theta \approx \tan \theta = \frac{\delta x}{w_0} = \frac{ct}{w_0} \frac{\delta n_e}{2n_c} \approx \frac{x}{w_0} \frac{\delta n_e}{2n_c} \quad (2.58)$$

Assuming that the laser pulse is focused with a half-angle Θ , as shown in fig. 2.8b, ionisation induced defocusing is neutralised when $\theta = \Theta$. For a Gaussian beam, it can be shown that⁴⁶ $\Theta = \lambda/\pi w_0$ and the Rayleigh length $z_R = \pi w_0^2/\lambda$. Thus, considering a propagation length of $x = 2z_R \approx ct$, ionisation induced defocusing dominates when¹¹¹,

$$\theta > \Theta \Rightarrow \frac{2\pi w_0^2}{\lambda} \frac{1}{w_0} \frac{\delta n_e}{2n_c} > \frac{\lambda}{\pi w_0} \Rightarrow \frac{\delta n_e}{n_c} > \left(\frac{\lambda}{\pi w_0} \right)^2 \quad (2.59)$$

This condition is largely true for regions immediately around the focus. For distances further away from the focus, it causes an increase in the radius of curvature, which results in a reduction in the peak laser intensity that could theoretically be achieved with a given focusing geometry, thereby causing a shift in the position of the peak intensity, as demonstrated by Auguste *et al*¹¹². This can however be compensated by going for either tighter focusing geometry or pre-ionization of the medium or through the choice of a target with less ionisation levels.

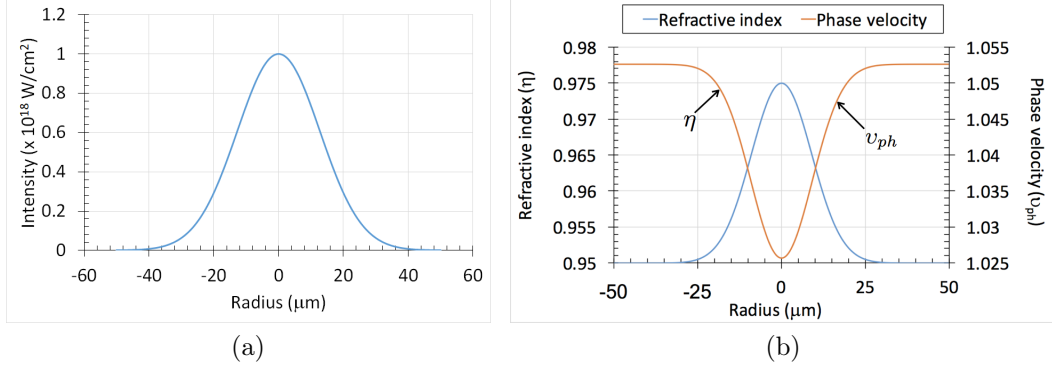


Figure 2.9: (a) Gaussian shaped radial laser intensity profile with a peak intensity of $1 \times 10^{18} \text{ W/cm}^2$ ($a_0 = 0.68$) and a FWHM radial diameter of $30 \mu\text{m}$, and (b) its corresponding plasma refractive index (η) and laser phase velocity (v_{ph}).

2.9.2 Self-focusing in Plasma

Self-focusing of a laser pulse in plasma can occur due to the combination of two effects namely, the relativistic electron mass increase close to the laser axis and the radial expulsion of electrons from the focal region due to the ponderomotive force of the laser pulse (as discussed in section 2.3). Through the act of self-focusing, the laser pulse's intensity can be further increased and it can be guided over lengths greater than the Rayleigh length.

Relativistic Self-focusing

In order to investigate the effect of the relativistic electron mass increase on the laser pulse's propagation, ponderomotive electron repulsion and dispersion effects will be neglected for the time being. Assuming a uniform plasma density, the refractive index (η) can be related to the relativistic factor through the normalised vector potential a_0 in the following way,

$$\eta = 1 - \frac{1}{2} \frac{\omega_p^2}{\omega_0^2} \left(1 - \frac{a_0^2}{2} \right) \quad (2.60)$$

where ω_p and ω_0 are the plasma and laser frequencies, respectively.

Considering a laser pulse of Gaussian radial intensity profile, as shown in figure 2.9a, propagating in a uniform plasma density of $0.1n_c$, the refractive index increases towards the centre of the laser pulse meaning that the corresponding phase velocity (v_{ph}) decreases, as shown in figure 2.9b. This acts as a positive lens thus causing the laser pulse to self-focus, until it is compensated by natural diffraction. The critical laser power (P_{cr}) required

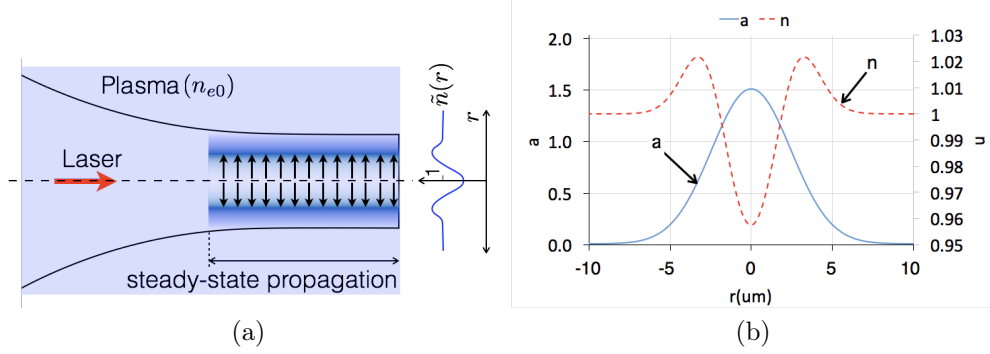


Figure 2.10: (a) Schematic representation of the cavity formation due to the ponderomotive expulsion of the electrons present in the laser's focal region, and (b) electron density variation across the cavity (\tilde{n}) in the steady-state limit corresponding to a Gaussian transverse intensity profile, where the a FWHM focal spot diameter of $6.6 \mu\text{m}$ (the spot size obtained at the vacuum focus of one of the experiments) is used.

for the self-focusing effect to set in can be shown to be⁵⁹,

$$P_{cr} = 17.5 \frac{\omega_0^2}{\omega_p^2} \text{GW} = 17.5 \frac{n_c}{n_e} \text{GW} \quad (2.61)$$

For $n_e = 0.05n_c$, $P_{cr} = 350 \text{GW}$, which can be readily exceeded by modern terawatt class laser systems for the laser pulse to be relativistically self-focused in a uniform plasma. This has also been experimentally demonstrated (for instance, for the hydrogen gas jet target¹¹³), where for $P < P_{cr}$ ionization induced defocusing dominates, and for $P > P_{cr}$ relativistic self-focusing dominates^{113–115}.

Ponderomotive Self-focusing

During the interaction between an intense laser pulse and a plasma medium, the non-uniform nature of the intensity distribution across the laser pulse results in a force that acts from the high to low intensity regions, which is called the ponderomotive force $\vec{F}_{pond} \propto \vec{\nabla}(\mathcal{E}_s^2)$, where \mathcal{E}_s denotes the envelope's \mathcal{E} -field amplitude (refer to 2.4). Near the focal region, this force is strong enough to radially expel the electrons from its intense regions to form an electron cavity¹¹⁶, as shown in fig. 2.10a. For an electron kinetic energy of 2MeV and laser focal radius ($1/e^2$) of $\sim 3 \mu\text{m}$, it takes $\sim 10 \text{fs}$ for the electron to be radially expelled from the central focal region. Compared to the FWHM pulse duration of the laser pulse ($\Delta\tau = 30 \text{fs}$) relevant to this thesis work, one can expect that the electron density distribution the laser pulse can accordingly differ due to response time of the electron expulsion. For instance, the electron distribution at the centre of the laser pulse can differ from that of front and back of the laser pulse. Therefore, the modified refractive

index of the plasma can cause different parts of the laser pulse to undergo ponderomotive self-focusing at varying degrees.

A detailed formulation of the coupled equations describing the evolution of the laser pulse and the electron density distribution can be found in the reference¹¹⁶. In the steady-state limit, where the laser pulse is guided by the electron cavity resulting from the ponderomotive electron expulsion, the radial electron density distribution across the cavity corresponding to a Gaussian transverse laser intensity of the form $a = a_0 \exp[-4 \ln 2 r^2 / \Delta r^2]$ where Δr is the FWHM laser spot size, is shown in fig. 2.10b. Here, the electron depletion occurring in the central focal region for $a > 1$ acts as a positive lens to guide the laser pulse. Together with relativistic self-focusing, it leads to a guiding of the laser pulse over distances much greater the Rayleigh length. This has also been experimentally demonstrated^{113;117;118}, during which both of these effects become indistinguishable from one another.

2.9.3 Self-Phase Modulation

Self-Phase Modulation (SPM) refers to the change in the instantaneous frequency of a laser pulse due to the intensity dependent refractive index in the longitudinal direction ($\eta(t) = \eta_0(t) + \eta_2(t)I(t)$) experienced by the pulse¹¹⁹. It can be seen as the equivalent of self-focusing in the longitudinal direction in a plasma. When a laser pulse is focused into a material such as a gas jet, the leading edge of the laser pulse ionises the atoms to form a plasma. The subsequent laser propagation in plasma depends on the interdependent evolution of electron density $n_e(x,t)$ and laser intensity $I(x,t)$. Here, the effect of SPM on the laser's propagation has been investigated neglecting the other propagation effects such as, ionisation induced defocusing, and relativistic and ponderomotive self-focusing.

Assuming that the envelope shape of the laser pulse and the longitudinal electron density profile remain unchanged in the co-moving reference frame of the laser pulse, the instantaneous plasma refractive index $\eta(\tau)$ is given by,

$$\eta(\tau) = 1 - \frac{1}{2} \frac{n_e(\tau)}{n_c} + \underbrace{\frac{1}{4} \frac{n_e(\tau)}{n_c} a_0^2(\tau)}_{\eta_2 I(\tau)} \quad (2.62)$$

$$\eta_2 I(\tau) \quad (2.63)$$

Here, the term $\eta_2 I(\tau)$ accounts for the contribution of the refractive index due to electron's relativistic mass increase for $a_0 < 1$. For $a_0 > 1$, $\eta(\tau)$ needs to be accordingly modified, as given by equation 2.53. The phase shift $\phi(t)$ accumulated by different parts of the laser pulse after a certain propagation length (L) is given by,

$$\phi(\tau) = \phi_0 + \omega_0 \tau + \phi_{SPM}(\tau) \quad (2.64)$$

where, ω_0 denotes the carrier frequency and $\phi_{SPM}(\tau)$ denotes the accumulated phase shift across the pulse due to the density and density-intensity dependent refractive index

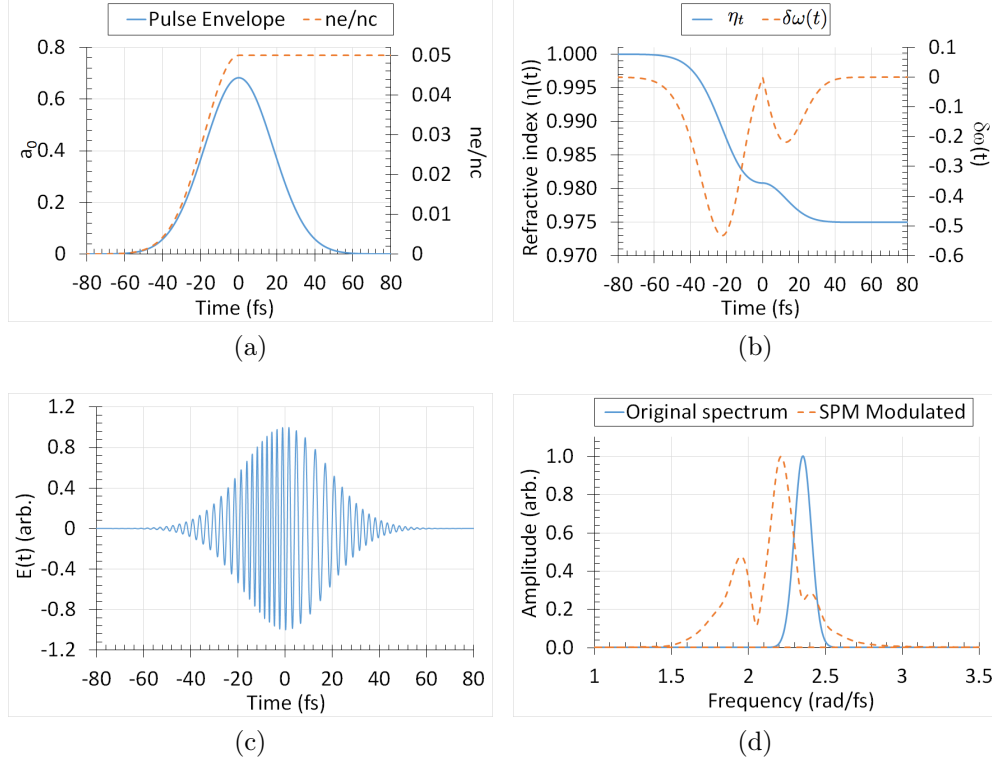


Figure 2.11: (a) Laser's intensity profile and the corresponding electron density profile, (b) the variation of the refractive index profile ($\eta(t)$) and the laser pulse's instantaneous frequency ($\delta\omega(t)$), (c) the modified \mathcal{E} -field of the laser pulse after the propagation of $100\ \mu\text{m}$ in plasma, (d) the unmodulated and self-phase-modulated spectrum of the laser pulse.

$(\eta_0, \eta_2 I)$ profiles of plasma, which can be expressed as⁴⁴,

$$\phi_{SPM}(\tau) = \frac{2\pi}{\lambda_0} \int_0^L \eta(\tau) dx \quad (2.65)$$

The instantaneous frequency $\omega(\tau)$ of the laser pulse is therefore given by,

$$\begin{aligned} \omega(\tau) &= \frac{d}{d\tau}[\phi(\tau)] = \omega_0 + \frac{d}{d\tau}\phi_{SPM}(\tau) = \omega_0 + \frac{d}{d\tau} \left[\frac{2\pi}{\lambda_0} \int_0^L \eta(\tau) dx \right] \\ &= \omega_0 + \underbrace{\frac{2\pi}{\lambda_0} L \frac{d}{d\tau} \eta(\tau)}_{\delta\omega(\tau)} \end{aligned} \quad (2.66)$$

where $\delta\omega(\tau)$ is the change in instantaneous frequency caused by the ionisation¹²⁰ and self-phase modulation⁴⁴ effects.

The effect of self-phase modulation on the temporal and frequency structure of a Gaussian laser pulse during its propagation through plasma has been shown in fig. 2.11. Here a peak laser intensity of $1 \times 10^{18} \text{ W/cm}^2$ corresponding to $a_0 = 0.68$, FWHM pulse duration $\Delta t = 30 \text{ fs}$, and peak electron density $n_e = 0.05n_c$ have been assumed. During the rising edge of the laser pulse, the electron density has been assumed to steadily increase and after the peak intensity, it remains constant neglecting ponderomotive effects of the laser pulse, as shown in fig. 2.11a. Figure 2.11b shows the refractive index profile $\eta(n_e, I)$ seen by the laser pulse in its co-moving reference frame and the instantaneous frequency change $\delta\omega(t)$ across the laser pulse after a propagation distance of $100 \mu\text{m}$. Figure 2.11c shows the corresponding self-phase modulated electric field of the laser pulse, where the frequency modulation across the laser pulse is evident. Figure 2.11d shows the corresponding modulated spectrum. The effect of self-phase modulation on pulse propagation and the resultant spectral broadening have also been extensively investigated^{121;122}.

2.10 Laser-Plasma Instabilities

Laser-plasma instabilities refer to the coupling of an electro-magnetic (EM) wave into various other wave forms in the plasma, such as electron plasma waves, ion acoustic wave and decay EM-waves and how it in-turn influences the pump EM-wave propagation in plasma. The onset of plasma instabilities is primarily due to the density fluctuations, which is either inherently present in the plasma or caused by the ponderomotive force of the laser pulse or the intensity fluctuations of the laser pulse⁹⁸. These density fluctuations can grow in time, if the laser pulse intensity exceeds a certain threshold value, determined by the prevailing plasma density and the type of decay wave.

When a laser pulse couples into an electron plasma wave, under the wave-matching condition $\vec{k}_0 = \vec{k}_s + \vec{k}_p$, where \vec{k}_0 , \vec{k}_s , \vec{k}_p are the wave vectors of the incoming light wave, decay light wave and plasma wave, the beating between the the incoming and scattering light waves causes variations in the electron density. If the fluctuations in the electron density are sufficient, it could also set up an ion density oscillation (ion-acoustic wave). A fluctuation in ion density in turn alters the electron density fluctuation and thus, the instability grows further. It is important to note that the density fluctuations need to be of scale lengths greater than the Debye length (λ_D) for them to grow on¹⁴.

Depending on the type of interaction between the laser pulse and plasma, the resulting instability assumes various forms (graphically shown in fig. 2.12), such as stimulated Raman scattering (SRS), stimulated Brillouin scattering (SBS), two-plasmon decay (TPD), stimulated electron acoustic decay (SEAS) and filamentation instability. The electron plasma wave produced during the primary EM-wave decay could lead to several secondary instabilities, such as Langmuir-wave decay instability (LDI), electro-magnetic decay instability (EDI) and dual electro-magnetic decay (DED). There is also the possibility of a cascading effect from the secondary instabilities produced⁹⁸.

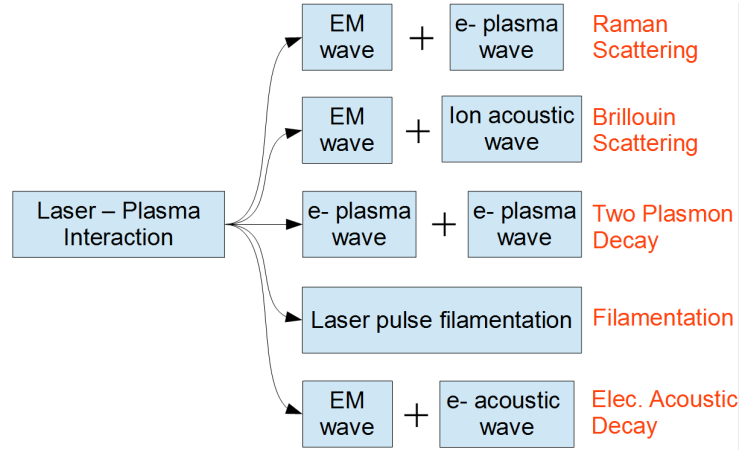


Figure 2.12: Type of instabilities arising during Laser-Plasma interaction.

2.10.1 Generalised Plasma Description

The evolution of a collisionless plasma can in general be described by the so-called Vlasov equation⁹⁸

$$\frac{\partial f_j}{\partial t} + \vec{v} \cdot \nabla f_j + \frac{q_j}{m_j} \left(\vec{\mathcal{E}} + \frac{\vec{v} \times \vec{B}}{c} \right) \cdot \frac{\partial f_j}{\partial \vec{v}} = 0 \quad (2.67)$$

where, $f_j(\vec{x}, \vec{v}, t)$ is the phase-space distribution function of the plasma species j (e.g. electron population), and \vec{x} and \vec{v} denote the spatial and velocity components, respectively. When combined with Maxwell's equations, it offers a complete description of the plasma evolution. Assuming that the ion population is stationary as they are much heavier than their counterpart, the following equations can be obtained by taking the first, second and third order velocity moments of the Vlasov equation for the electron population⁹⁸,

$$\frac{\partial n_e}{\partial t} + \nabla \cdot (n_e \vec{v}_e) = 0 \quad (\text{Continuity equation}) \quad (2.68)$$

$$\frac{\partial v_e}{\partial t} + \vec{v}_e \cdot \nabla v_e - \frac{e}{m_e} \left(\vec{\mathcal{E}} + \frac{\vec{v}_e \times \vec{B}}{c} \right) = -\frac{\nabla p}{n_e m_e} \quad (\text{Eq. of motion}) \quad (2.69)$$

$$\frac{p}{n_e^{5/3}} = \text{Constant} \quad (3\text{D Pressure equation})(2.70)$$

where, the electron plasma pressure (p) is given by $p = n_e k_B T_e$, where k_B is the Boltzmann constant and T_e is the plasma temperature. Equation 2.70 is valid under adiabatic condition, where any energy transfer between plasma and external source (e.g. laser pulse) is neglected. These equations form the basis for numerical simulations of plasma phase-space evolution and also for the laser-plasma instability analysis. The coupling between

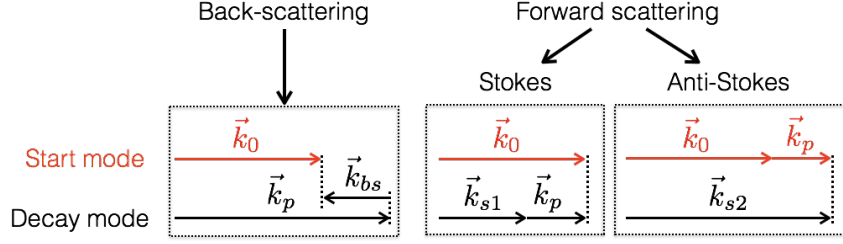


Figure 2.13: Raman forward scattering and back-scattering decay modes.

different species (e.g. electron and ion populations) of the plasma is taken into account through Maxwell's equation $\nabla \cdot \vec{\mathcal{E}} = \rho/\epsilon_0$, where $\rho = -en_e + q_i n_i$ with n_e and n_i being the electron and ion densities and $q_i = eZ$, where Z is the charge state of the ion species¹⁴. If collisions among electrons, ions and atoms, which are neglected here, are to be taken into account, an additional collisional term needs to be introduced in eqn. 2.69. The resulting equation of motion is called the Boltzmann equation¹⁴.

2.10.2 Raman Scattering

Stimulated Raman scattering or Raman instability refers to the decay of a light wave into an electron plasma wave and a scattered light wave of lower frequency. Depending on the direction of the scattered light wave, it can be categorised into *forward*, *backward* and *side-scattering*. The decay waves can subsequently interact with the incoming laser pulse to grow in time, which can be quantified using the respective growth rates (will be discussed in the following section). The corresponding phase matching (momentum conservation) and frequency matching (energy conservation) conditions for the Raman decay are given by,

$$\vec{k}_0 = \vec{k}_s + \vec{k}_p; \quad \omega_0 = \omega_s + \omega_p \quad (2.71)$$

where \vec{k}_0 , \vec{k}_s , \vec{k}_p are the wave vectors of the incoming, scattered and plasma waves, and ω_0 , ω_s , ω_p are the frequencies of the incoming, scattered and plasma waves, respectively. The magnitude of the wave vector $k = 2\pi/\lambda$, where λ is the respective wavelength. Plasma wave growth overcomes its damping rate only when $k_p \lambda_D < 1$ meaning that the plasma wavelength (λ_p) is greater than the Debye length¹²³ λ_D . Therefore, for $\lambda_p > \lambda_D$, Raman instability can grow as long as the decay wave components temporally overlap with the incoming light wave.

Backscattering

Raman backscattering can be viewed as a three wave mixing process ($k_0 = k_p - k_{bs}$), where an incoming light wave decays into a plasma wave (k_p) and a backscattered light

wave (k_{bs}), as shown in fig. 2.13. This decay is convective in nature i.e. the decay waves have a non-zero phase velocity⁹³. Considering that for backscattering $k_s \leq k_0$ (which will be derived in a later section), the wave vector of the plasma wave satisfies $k_0 \leq k_p \leq 2k_0$, which corresponds to¹²⁴ $\lambda_0/2 \leq \lambda_p \leq \lambda_0$. The frequency of the scattered light wave is given by $\omega_s = \omega_0 - \omega_p$, where the (non-relativistic) plasma frequency $\omega_p = (n_e e^2 / \epsilon_0 m)^{1/2}$ with n_e being the plasma density. For instance, for $k_s = k_0 = k_p/2$, the phase velocities of the scattered light wave (v_s) and the plasma wave (v_p) are given by,

$$v_s = \frac{\omega_s}{k_s} = \frac{\omega_0 - \omega_p}{k_0} = v_0 - \frac{\omega_p}{k_0} < v_0; \quad v_p = \frac{\omega_p}{k_p} = \frac{\omega_p}{2k_0} \ll v_0 \quad (2.72)$$

where $v_0 = v_{ph} = \omega_0/k_0$. For example, for $n_e = 0.01n_c$, $\omega_p \approx 0.1\omega_0$, we obtain $v_s = 0.9v_0$ and $v_p = 0.05v_0$.

Because of the slow nature of the resulting plasma wave, it can trap the background thermal electrons, whereby the electrons gain energy and/or get displaced in phase. These electrons can be subsequently trapped by the plasma wave resulting from the Raman forward scattering, which is close to the group velocity of the laser pulse^{125;126}. Although the total growth of the backscattering is limited by the temporal overlap between the incoming and backscattered light wave components, it can be shown to have a higher rate of growth than the Raman forward scattering⁹⁸. Therefore, it can prove to be detrimental to the laser pulse, as its energy is being transported away causing pump depletion^{127;128}.

Forward Scattering

Raman forward scattering can be viewed as a four wave mixing process among the input wave (k_0), plasma wave (k_p), Stokes wave (k_{s1}) and anti-Stokes wave (k_{s2}), as shown in figure 2.13. In Stokes decay ($k_0 = k_{s1} + k_p$; $\omega_{s1} = \omega_0 - \omega_p$), the frequency of the resulting decay light wave is less than that of the incoming light wave i.e. $\omega_{s1} < \omega_0$. In anti-Stokes decay ($k_{s2} = k_0 + k_p$; $\omega_{s2} = \omega_0 + \omega_p$), the laser pulse (k_0) couples with the plasma wave (k_p) resulting from the Stokes decay to yield a decay light wave component (k_{s2}) with frequency higher than that of the incoming light wave i.e. $\omega_{s2} > \omega_0$. In other words, anti-Stokes decay is a secondary decay resulting from the Stokes decay. Thus, the phase and frequency matching conditions for the forward scattering, where the wave vectors aligned in-line, are:

$$k_{s1,s2} = k_0 \mp k_p; \quad \omega_{s1,s2} = \omega_0 \mp \omega_p \quad (2.73)$$

It is important to note that all the light wave components satisfy dispersion relations of the form $\omega^2 = \omega_p^2 + c^2 k^2$. Since the anti-Stokes decay is a secondary process, it can be assumed to be non-resonant and thus not of relevance¹²⁹. The plasma wave (k_p) resulting from the Stokes decay can be construed as the wakefield formed by electron density oscillations (or Langmuir wave¹³⁰) excited at the wake of an intense laser pulse propagating in plasma, as discussed in section 2.7.

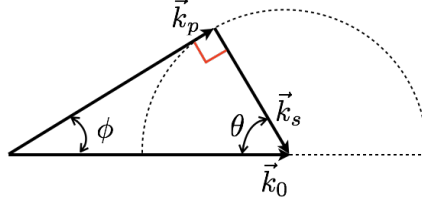


Figure 2.14: Raman side-scattering wavevector alignment¹²³, where the magnitude of the scattered wave is constant for a given plasma density (refer to eqn. 2.74).

Side-scattering

Raman side-scattering results from the non-alignment of wave vectors, as shown in figure 2.14, that limits the region over which the waves can resonantly interact limiting its growth¹²³. For strongly underdense plasma ($n_e \ll n_c$), the wave matching condition for side-scattering yield the wave number of the scattered wave k_s , which can be expressed as¹³¹

$$k_s = k_0 \sqrt{1 - 2\frac{\omega_p}{\omega_0}} = k_0 \sqrt{1 - 2\sqrt{\frac{n_e}{n_c}}} \quad (2.74)$$

This shows that for a given plasma density n_e , k_s remains constant, as shown in fig. 2.14. The wave number of plasma wave, depending on the wave vector non-alignment angle ϕ , can be expressed as,

$$k_p = k_0 \cos \phi - (k_0^2 \cos^2 \phi - 2\omega_p \omega_0 / c^2)^{1/2} \quad (2.75)$$

where ϕ - angle between the laser pulse and plasma wave as shown in fig. 2.14. The angle at which maximum wave vector non-alignment can occur is given by,

$$\sin \theta = \cos \phi = \sqrt{\frac{2\omega_p}{\omega_0}} = 2.45 \times 10^{-7} \left[\frac{n_e / \text{cm}^{-3}}{\gamma} \right]^{1/4} \sqrt{\lambda_0 / nm^{-1}} \quad (2.76)$$

Relevance

Since the minimum laser frequency allowed by the plasma is ω_p , substituting $\omega_s = \omega_p$ in the frequency matching condition $\omega_0 = \omega_p + \omega_s$ results in

$$\omega_0 \geq 2\omega_p; \quad n_e < \frac{n_c}{4}$$

where $(\omega_0 / \omega_p)^2 = n_c / n_e$. This relation shows that Raman instability occurs primarily at densities below $n_c / 4$ and therefore, it is a relevant instability in the low density region. For relativistic intensities, Raman scattering can occur at densities up to $\langle \gamma_e \rangle n_c / 4$, where

$\langle \gamma_e \rangle$ is the average Lorentz factor associated with the electron motion. In the case of the plasma medium with a density gradient, the length over which the waves can resonantly interact is limited due to the inhomogeneity, thus any further propagation of the decay waves is heavily damped¹²⁹. Here, the wave vectors become time dependent and the mathematical treatment of such a scenario becomes rather complicated¹³².

Using the dispersion relation $\omega^2 = \omega_p^2 + c^2 k^2$, the phase (v_s) and group ($v_{s,gr}$) velocities of the scattered wave can be written as,

$$v_s = \frac{\omega_s}{k_s} = \frac{c}{\left(1 - (\omega_p^2/\omega_s^2)\right)^{1/2}}; \quad v_{s,gr} = \frac{\partial \omega_s}{\partial k_s} = c \left(1 - \frac{\omega_p^2}{\omega_s^2}\right)^{1/2} \quad (2.77)$$

This shows that at $n_e = n_c/4$ (i.e. $\omega_s = \omega_p$), Raman instability growth is absolute meaning that its group velocity $v_{s,gr}$ approaches zero. As a result, the instability does not drift away meaning that the scattered light gets trapped, which can become intense enough to expel the surrounding electrons¹²⁹.

The dispersion relation can also be further used to obtain the plasma wave number k_p for forward and backscattering processes, as follows:

$$k_p = k_0 \mp k_s = \frac{\omega_0}{c} \left(1 - \frac{\omega_p^2}{\omega_0^2}\right)^{1/2} \mp \frac{\omega_0 - \omega_p}{c} \left(1 - \frac{\omega_p^2}{(\omega_0 - \omega_p)^2}\right)^{1/2} \quad (2.78)$$

$$= \frac{\omega_0}{c} \left[\left(1 - \frac{n_e}{n_c}\right) \mp \left(1 - 2 \left[\frac{n_e}{n_c}\right]^{1/2}\right)^{1/2} \right] \quad (2.79)$$

where $(\omega_p/\omega_0)^2 = n_e/n_c$. For instance, for $n_e = 0.01n_c$, the plasma wave number for Raman backscattering $k_p = 0.1k_0$, whereas for forward scattering $k_p = 1.9k_0$.

2.10.3 Formulation

Raman instability can be qualitatively described in the following way: when a laser pulse propagates in a plasma with a density perturbation, the electrons start to oscillate along the electric field of the laser pulse at laser's central frequency generating a transverse current $\delta J = -ev_e \delta n_e$, where v_e is the electron velocity and δn_e is the electron density perturbation. As a result, the transverse current generates a scattered wave, which interferes with the incident light, altering its field amplitude. This could eventually lead to laser pulse breakup, which could in turn alter the transverse electron current, thus setting up a feedback loop.

A brief mathematical formulation of this process is given below, whereas a detailed mathematical treatment was formulated by Krueer⁹⁸. Assuming that the laser pulse is propagating through a plasma of uniform density and temperature, Ampère's law ($\nabla \times$

$\vec{B} = \mu_0(\vec{J} + \varepsilon_0(\partial\vec{E}/\partial t))$ - refer to section 2.6) in the Coulomb-gauge can be written as,

$$\left(\frac{\partial^2}{\partial t^2} - c^2\nabla^2\right)\vec{A} = -\frac{e^2}{\varepsilon_0 m_e}n_e\vec{A} \quad (2.80)$$

where $\vec{E}(x,t) = -\partial\vec{A}/\partial t$, $\vec{B}(x,t) = \nabla \times \vec{A}$ and $\nabla \cdot \vec{A} = 0$ under plane-wave assumption. Here, a longitudinal electrostatic wave is assumed i.e., $\nabla \cdot \vec{J}_t = 0$, where \vec{J}_t is the transverse current, and $|v_e| \ll c$ (non-relativistic), where v_e is the transverse electron velocity.

Substituting $\vec{A} = \vec{A}_l + \vec{A}_s$, where scattered wave amplitude $\vec{A}_s \ll \vec{A}_l$ (laser amplitude) and $n'_e = n_e + \delta n_e$, where $\delta n_e \ll n_e$, equation 2.80 can be accordingly modified to

$$\left(\frac{\partial^2}{\partial t^2} - c^2\nabla^2 + \omega_p^2\right)\vec{A}_s = -\frac{e^2}{\varepsilon_0 m_e}\delta n_e\vec{A}_l \quad (2.81)$$

This equation describes the scattering of a large amplitude wave by the electron density fluctuation. Whereas, an equation describing plasma wave evolution due to variations in the laser field can be obtained from Vlasov equations 2.68 and 2.69.

$$\left(\frac{\partial^2}{\partial t^2} + \omega_p^2 - 3v_e^2\nabla^2\right)\delta n_e = \frac{n_e e^2}{m_e^2 c^2}\nabla^2(\vec{A}_l \cdot \vec{A}_s) \quad (2.82)$$

Eqs. 2.81 and 2.82 describe the coupling between the light wave and plasma perturbations.

Dispersion Relation

Assuming that the anti-Stokes component is nonresonant (as it is a secondary process), the dispersion relation for a plane wave propagating in plasma is given by⁹⁸,

$$(\omega^2 - \omega_{ek}^2) \left[(\omega - \omega_0)^2 - (\vec{k} - \vec{k}_0)^2 c^2 - \omega_p^2 \right] = \frac{\omega_p^2 k^2 v_e^2}{4} \quad (2.83)$$

where the decay mode frequency ω is a function of the plasma density and laser intensity, and can in general be expressed as $\omega = \Omega + i\Gamma$, where $\Omega (\gg \Gamma)$ is the plasma frequency shift and Γ is growth rate. At low intensities $\Omega \approx \omega_{ek}$, the growth rate for Raman forward scattering (Γ_{FRS}) and Raman back-scattering (Γ_{RBS}) for constant pump strengths can be expressed as^{59;98}

$$\Gamma_{\text{FRS}} \approx \frac{\omega_p^2}{2\sqrt{2}\omega_0} \frac{v_e}{c} \approx \frac{\omega_p^2}{2\sqrt{2}\omega_0} \frac{a_0}{(1 + a_0^2/2)}; \quad \Gamma_{\text{RBS}} = \omega_p \frac{\sqrt{3}}{2} \left(\frac{\omega_0}{2\omega_p}\right)^{1/3} \frac{a_0^{2/3}}{(1 + a_0^2/2)^{1/2}} \quad (2.84)$$

where a_0 is the normalised vector potential of the laser pulse.

Nonlinear Aspects

Strictly speaking, the introduction of the relativistic factor (through a_0) in growth rates Γ_{FRS} and Γ_{RBS} does not correctly treat the intensity dependent Raman scattering process. This is due to the non-relativistic transverse velocity assumption ($v_t \ll c$) involved in the formulation of the coupled equations 2.81 and 2.82, which does not necessarily hold true for relativistic intensities. In addition to the four-wave process $\omega_p \pm \omega_0$, an electron fluctuation at ω_p can also couple to higher harmonic components such as, $\omega_p \pm 2\omega_0$ (six-wave mixing) for $a_0 > 1$ ^{133;134}. The growth rate for six-wave mixing has also been shown to be comparable to the four-wave mixing case. A further analysis shows that at relativistic intensities ($a_0 > 1$), the growth is significant over a wide range of density regions and wave number space, where a significant portion of the laser-pulse energy can be expected to be scattered¹³². The coupling between the laser pulse and the plasma wave, in general, results in new spectral components ($\omega_0 \pm n\omega_p$), which can be used to estimate the associated plasma density through the spectral analysis of the transmitted light^{135;136}.

Furthermore, Raman Back-Scattering (RBS) has also been treated similar to the Free Electron Laser (FEL) instability, where the laser pulse plays the role of a wiggler and the plasma electrons are compared to the electron beam¹³⁷. In this treatment, nonlinear effects, such as return current and radiation reaction are taken into account. The RBS growth has been derived from the density fluctuations created by the ponderomotive force of the laser pulse. At relativistic intensities, the extent to which forward, side- and back-scattering processes compete with each other at various density regimes still must be experimentally investigated. In this thesis, the observation of Raman side-scattering for $a_0 > 1$ will be reported in the experimental findings section. If the scattered energy becomes comparable to the laser pulse energy, SRS could lead to strong pulse depletion and pulse breakup¹³³.

2.10.4 Two Plasmon Decay (TPD)

Two Plasmon Decay is a three wave mixing process, where the light wave decays into two plasma waves. This instability is of particular concern for experiments, such as inertial confinement fusion (ICF), where the early generation of energetic electrons through the excitation of the electron plasma wave needs to be avoided. In terms of the frequency matching condition, $\omega_0 = \omega_1 + \omega_2$, where $\omega_{1,2}$ - plasma wave decay modes. Resonant TPD decay occurs for $\omega_{1,2}^2 = \omega_{ek}^2 = \omega_p^2 + 3v_{th}^2 k_{1,2}^2$, where if the plasma temperature were to be ignored, $\omega_{1,2} \approx \omega_p = \omega_0/2$. Thus, similar to Raman scattering, TPS also dominates at $n_e < n_c/4$ densities, as $(\omega_p/\omega_0)^2 = n_e/n_c$. In the absence of any direction observation of the laser-plasma interaction, the observation of half integer laser harmonics such as, $\omega_0/2$ and $3\omega_0/2$ due to the interaction between the laser pulse and the plasma wave is usually an indication of the presence of TPD¹³⁸⁻¹⁴³.

Dispersion Relation

Similar to SRS, the dispersion relation for TPD can be obtained from the Vlasov equations 2.68 and 2.69 using the density perturbation method. Neglecting the secondary and non-resonant modes such as, $\omega + \omega_0$ and $\omega - 2\omega_0$, the dispersion relation for TPD in terms of the decay mode wavenumbers \vec{k} and $\vec{k} - \vec{k}_0$ can be written as⁹⁸

$$(\omega^2 - \omega_{ek}^2)[(\omega - \omega_0^2)^2 - \omega_{e(k-k_0)}^2] = \left[\frac{\vec{k} \cdot \mathbf{v}_e \omega_p [(\vec{k} - \vec{k}_0)^2 - k^2]}{2k|\vec{k} - \vec{k}_0|} \right]^2 \quad (2.85)$$

where \vec{v}_e is the electron oscillation velocity. Substituting $\omega = \omega_{ek} + i\Gamma_{\text{TPD}}$, the (linear) TPD growth rate γ_{TPD} can be obtained

$$\Gamma_{\text{TPD}} \approx \frac{\vec{k} \cdot \mathbf{v}_e}{4} \left| \frac{(\vec{k} - \vec{k}_0)^2 - k^2}{k|\vec{k} - \vec{k}_0|} \right| \quad (2.86)$$

For $k \gg k_0$ (under-dense plasma), the maximum growth rate of $k_0 v_e / 4$ can be shown to occur at 45° to the propagation direction, which is also expected to hold even in inhomogeneous plasma as it does not depend on the electron density (n_e). The threshold growth rate is primarily determined by Landau damping in the absence of collisions.

In the case of inhomogeneous plasma, TPD instability could be both absolute, meaning that it grows in time in a confined space, and convective, meaning that it could propagate away from its origin¹⁴⁴. At relativistic intensities ($a_0 > 1$), its growth rate and threshold intensity could be expected to be different from that of the linear regime^{145;146}. Unfortunately, current theories do not offer a complete description of TPD in the nonlinear regime. This instability could also lead to substantial pump depletion and could be detrimental to LWFA.

2.10.5 Modulational and Filamentation Instability

When an intense laser pulse propagates through a plasma medium, it could undergo amplitude and phase modulations due to electron density fluctuations present in the plasma medium. These modulations could alter the pulse structure throughout its further propagation. If the modulations are in the laser propagation direction, it is referred to as modulation instability (MI), whereas modulations in the transverse direction lead to filamentation instability (FI), both of which could lead to pulse break-up.

Plasma density modulations arise primarily due to the variations in the ponderomotive force across the laser pulse. Since electrons are expelled from regions of ponderomotive force maxima, it leads to a non-uniform electron density, where light is refracted towards the regions of lower density. Thus, the feedback between the plasma density and the laser intensity modulations modifies the pulse structure as it propagates along the plasma

medium. The laser pulse, as a result, experiences a periodically modulated refractive index profile due to electron density oscillations (*wakefield*) at the trail of the laser pulse. The density modulations could also grow from the noise present in plasma.

Modulational Instability

Modulations in the amplitude of the laser pulse's \mathcal{E} -field envelope can result in side-band frequencies in its spectral window that can grow in time¹⁴⁷. Considering a plane wave of the form $E = E_0 \exp[i(k_0x - \omega_0t)]$ propagating through a plasma medium of length L , its dispersion relation (D) is given by $D = \omega^2 - \omega_p^2 - c^2k^2 = 0$, where the plasma frequency $\omega_p = \sqrt{n_e e^2 / \varepsilon_0 m_e}$. Assuming that the plasma has a modulated density form of $n_e = n_0 + \delta n$, where $\delta n = \delta n_0 \cos(k_p x - \omega_p t) \ll n_0$. A modulation in the electron-density results in the modulation of central laser frequency ($\delta\omega$), which can be expressed as $\omega = \omega_0 + \delta\omega$. $\delta\omega$ can be related to the electron density (n_e) as follows¹⁴⁷

$$\begin{aligned} \delta\omega &\approx \frac{d\omega}{dt} \delta t = \frac{\partial D / \partial t}{\partial D / \partial \omega} \frac{kL}{\omega} \approx -\frac{\partial n_e}{\partial t} \frac{e^2}{\varepsilon_0 m} \frac{1}{2\omega_0} \frac{k_0 L}{\omega_0} \\ &\approx -\delta n_0 \omega_p \sin(k_p x - \omega_p t) \frac{\omega_p^2}{n_e} \frac{1}{2\omega_0} \frac{k_0 L}{\omega_0} \approx -\delta\omega_0 \cdot \sin(k_p x - \omega_p t) \end{aligned} \quad (2.87)$$

where the modulation frequency amplitude $\delta\omega_0 = \omega_p^3 / 2\omega_0^2 \cdot \delta n_0 / n_e \cdot k_0 L$. In the case of a laser pulse interaction with a plasma wave, this quantity ($\delta\omega_0$) represents the increase in frequency of the EM wave packet trapped in an electron plasma wave corresponding to the energy loss of the plasma wave (termed *photon acceleration*)¹⁴⁸. After a certain propagation distance L , the modulation frequency also introduces modulations in the \mathcal{E} -field of the input wave, which can be mathematically shown as follows

$$\begin{aligned} \mathcal{E} &= \mathcal{E}_0 \exp[i(k_0x - [\omega_0 - \delta\omega_0 \sin(k_p x - \omega_p t)]t)] \\ &= \mathcal{E}_0 \exp[i(k_0x - \omega_0 t)] \cdot \sum_{l=-\infty}^{\infty} J_l(t\delta\omega_0) \exp[il(k_p x - \omega_p t)] \end{aligned} \quad (2.88)$$

where the Jacobi-Anger series [$\exp(iz \sin \theta) = \sum_{n=-\infty}^{\infty} J_n(z) \exp^{in\theta}$] is used to expand the \mathcal{E} -field and $J_l(t\delta\omega_0)$ is the l -th Bessel function of the first kind with approximately 2π periodicity. In contrast to Raman scattering, where harmonics of ω_p are added to the laser frequency ($\omega_0 \pm n\omega_p$), equation 2.88 shows that the \mathcal{E} -field is modulated by both plasma density perturbation ($\delta\omega$) and its natural frequency (ω_p). The spectral analysis of the modulated \mathcal{E} -field shows the growth of side-bands corresponding to frequency intervals $\omega_0 \pm l\omega_p \pm \delta\omega$ at the expense of the driving \mathcal{E} -field, where side-bands separated by intervals much less than ω_p can also be found. This is illustrated in figure 2.15, where both the \mathcal{E} -field modulation and its spectral components are shown.

Extending the same approach to a laser pulse, strong modulations in its \mathcal{E} -field could drastically change the envelope shape and lead to a split-up of the laser pulse in the

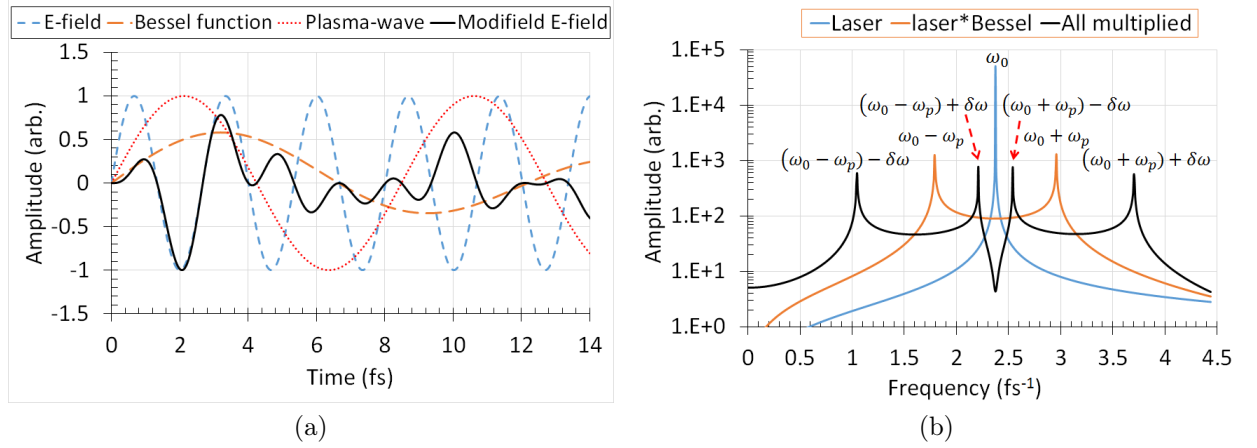


Figure 2.15: (a) \mathcal{E} -field modulation due to plasma perturbation and wave excitation for a propagation length of $250 \mu\text{m}$, $\omega_0 = 2.35 \text{ fs}^{-1}$ ($\lambda_0 = 0.8 \mu\text{m}$), $\omega_p = 0.74 \text{ fs}^{-1}$ ($n_e = 0.1n_c$, $\delta n_e = 0.01n_e$) and $\delta\omega = 0.288 \text{ fs}^{-1}$, (b) its spectral window showing various frequency components.

longitudinal direction. Thus, the spectral broadening extent and the side-band instability can be used as a diagnostic tool for laser wakefield acceleration^{147;149}. In the case of a plasma medium with a density gradient, during the interaction with a laser pulse, a wide range of side-bands can be expected to appear on both sides of the laser frequency. In a similar approach to Raman scattering, Decker *et al.*, obtained the growth rate for MI (Γ_{MI}) in the low intensity limit¹⁵⁰

$$\Gamma_{\text{MI}} = \frac{\omega_p^2}{8\omega_0} \frac{a_0^2}{(1 + a_0^2)^{3/2}} \quad (2.89)$$

Filamentation Instability

Filamentation instability is a non-resonant coupling between the laser pulse and the transverse density perturbation^{151;152}. In the case of a collisionless plasma, the local variations in the intensity of the laser pulse is the primary cause of the filamentation process, which can be qualitatively explained in the following way: any local increase in the laser intensity leads to an increase in the local refractive index due to ponderomotive and relativistic self-focusing effects. This acts as a positive lens to create bundles of EM-waves (filaments) across the laser beam, which causes the local laser intensity to further increase. An increased laser intensity expels the electrons from the intense regions even more^{153;154}. Thus, the modified laser beam could start a feedback loop and increase the filamentation process, which manifests itself as a transverse standing wave of electron density perturbations¹²³. Relativistic self-focusing can be considered to be a special case of filamentation,

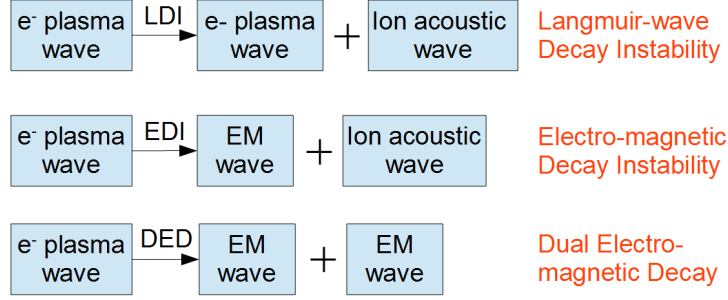


Figure 2.16: Possible secondary instabilities during the laser-Plasma interactions.

where the change in refractive index due to relativistic effects in the transverse direction also plays a crucial role. Kruer⁹⁸ derived the growth-rate for filamentation instability based on the dispersion relation for Brillouin scattering, which is given by,

$$\Gamma_{\text{FI}} = \frac{1}{8} \frac{\omega_p^2}{\omega_0} \frac{c^2}{v_e^2} \frac{a_0^2}{1 + a_0^2/2} \quad (2.90)$$

A more detailed treatment can be found in references^{152;155}.

2.10.6 Other Instabilities

During the laser-plasma interaction, the EM-wave could decay into a scattered EM-wave and ion-acoustic motion, which is referred to as *Brillouin Scattering* (BS). Similar to Raman scattering, BS could also undergo forward (Stokes and anti-Stokes) and backward scattering, where the scattered wave's frequency is close to the pump frequency. In the case of back-scattering, the ion wave vector is on the order of the laser wave vector and therefore, could lead to resonant scattering. Reflectivity of up to 10% has been previously reported¹⁵⁶. Due to the heavy nature of ions, their oscillation frequency (ω_{pi}) is much smaller than their electron counterpart, and therefore, it is present throughout the underdense regime up to the critical density (n_c). For example, Argon ions with $n_e = 0.2n_c$ yield an ion frequency $\omega_{pi} = 8.5 \times 10^{12} \text{ s}^{-1}$, whereas electron plasma frequency $\omega_p = 10^{15} \text{ s}^{-1}$ (i.e. $\omega_{pi} \approx \omega_p/100$). This corresponds to an ion oscillation period of $\tau_{pi} = 740 \text{ fs} \gg 30 \text{ fs}$ (laser pulse duration). Thus, this instability is only relevant for pulse durations greater than the ion oscillation period.

In addition to the instabilities mentioned so far, an electron plasma wave (EPW) could also decay into other secondary wave forms as shown in figure 2.16. In particular, Langmuir wave decay instability (LDI) refers to the decay of an EPW into another counter propagating EPW of approximately the same frequency and a low frequency ion acoustic wave at the cost of pump EPW damping. This instability occurs when the EPW is strong enough to cause a disturbance in the ion population. It has been shown through

simulations that the oscillation energy of EPW has to be greater than the thermal energy of the background electrons for this to occur¹⁵⁷. The generation of an ion acoustic wave from an EPW has also been experimentally verified by Depierreux *et al.*¹⁵⁸.

Another instability that results from the decay of an EPW is the electro-magnetic decay instability (EDI) which yields an EM-wave and an ion acoustic wave. Since the scattered EM-wave frequency is close to the pump EPW frequency, it can be used to determine the type of primary instability associated with the laser-plasma interaction. For example, two plasma decay (TPD) results in two plasma waves, each at half the laser frequency ($\omega_0/2$). Thus, any observation of light emission at $\omega_0/2$ from the interaction region might indicate the presence of the TPD instability through EDI¹⁵⁹. Any ion density perturbation caused by EDI could act as a seed for Brillouin scattering¹⁶⁰.

Since the secondary instabilities drain the energy of the pump EPW, they act as a threshold for Raman and TPD instabilities limiting the amount of energy that can be transferred to the EPW. They could also lead to a cascading effect, if the decay modes are strong enough to exceed the threshold for any particular instability.

Chapter 3

Experimental Set-up

This chapter describes the experimental layout and diagnostics used for the high intensity laser-plasma experiments carried out at the JETI40 laser facility at IOQ and the characterisation of the gas nozzles, which were used in those experiments.

3.1 Laser-Plasma Experiments

3.1.1 Experimental Layout

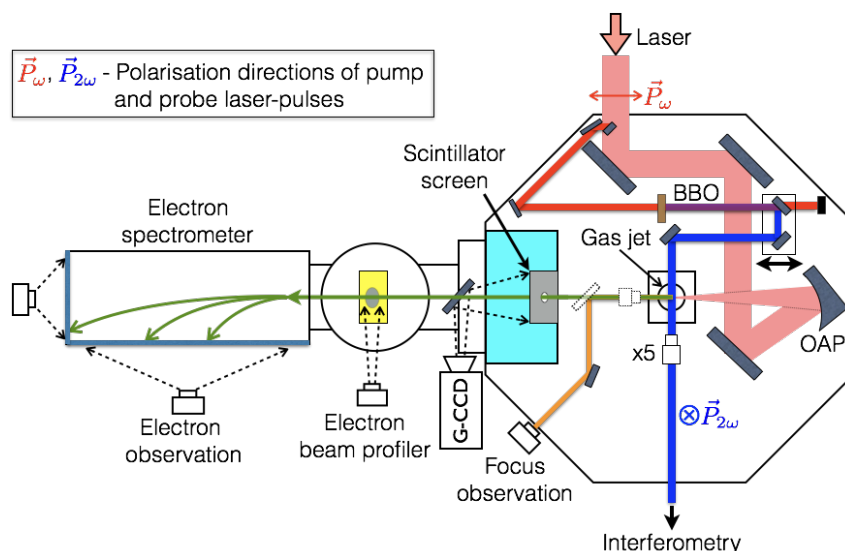


Figure 3.1: Schematic layout of the experimental setup used at JETI40.

The high intensity laser-plasma experiments have been carried out at the JETI40 laser, which is a solid-state high-power laser system using the technique of Chirped Pulse Amplification (CPA) that is capable of producing laser pulses of up to 40 TW power. It can be operated at a repetition rate of 10 Hz with a maximum pulse energy of 550 mJ on target. The output pulses have a beam diameter of 55 mm and a pulse duration of ~ 30 fs. The two laser-plasma interaction experiments that have been carried out during June 2014

Experimental conditions	June-2014	March-2015
Focusing optics	f/6	f/2
Gas-jet	Subsonic	Transonic
Side-view imaging	Achromat	Mitutoyo mic. objective
FWHM focal-spot radius	3.3 μm	1.3 μm
Pulse energy on target (inside the FWHM focus)	210 mJ	190 mJ
Maximum intensity, I	4.4x10 ¹⁹ W/cm ²	2.5x10 ²⁰ W/cm ²
Normalised vec. pot., a_0	3.2	7.6
Ponderomotive potential, Φ_p	1.2 MeV	3.4 MeV
Critical density, n_c	1.72 x 10 ²¹ cm ⁻³	

Table 3.1: Important laser and experimental parameters.

and March 2015 at JETI40 have similar experimental setups with a few differences in the diagnostics, which are shown in table 3.1. Figure 3.1 shows the schematic layout of the experimental setup, in which the laser pulses were focused using an off-axis parabola ($f/6$ and $f/2$) into the gas jet at a height of $500\ \mu\text{m}$ above the nozzle outlet. Their respective focal spots were imaged onto a CCD (16-bit) using a microscope objective that was placed after the focal region, as shown in fig. 3.1. The resulting intensity distributions of the focal spots are shown in fig. 3.2, which were optimized using adaptive optics.

The laser-plasma interaction region was probed using a (2ω) probe beam of 400 nm at 90° with respect to the main beam's propagation direction. This has been generated by reflecting off a small portion of the main beam and allowing it to pass through a (free standing) BBO crystal of $150\ \mu\text{m}$ thickness, as shown in fig. 3.1. The BBO crystal was characterised beforehand to have $\sim 40\%$ second-harmonic conversion efficiency. The dichroic mirror mounted on a delay-stage after the BBO crystal separated the second-harmonic beam from the first-harmonic, as it has a very high reflectance ($>99.5\%$) for 350 – 440 nm and high transmission (96%) for 500 – 1000 nm. The delay-stage was used to change the arrival time of the probe beam with respect to the main beam. The pulse duration of the probe beam remained nearly the same, as the dispersion caused by the BBO crystal was negligible compared to the pulse duration. The FWHM duration of a Gaussian laser-pulse broadened due to group velocity dispersion ($D_\omega = \partial^2 k / \partial \omega^2$) is given by,¹⁶¹

$$\Delta\tau_2 = \Delta\tau_1 \sqrt{1 + \left(\frac{4 \ln 2 \cdot D_\omega \cdot L}{\Delta\tau_1^2} \right)^2} \quad (3.1)$$

where $\Delta\tau_1$ and $\Delta\tau_2$ are the pulse durations of the laser-pulse before and after the BBO crystal, and L is the propagation length in the crystal. For $\Delta\tau_1 = 30$ fs, a BBO crystal of $150\ \mu\text{m}$ thickness (L) and $196\ \text{fs}^2/\text{mm}$ dispersion parameter¹⁶² (D_ω) corresponding to

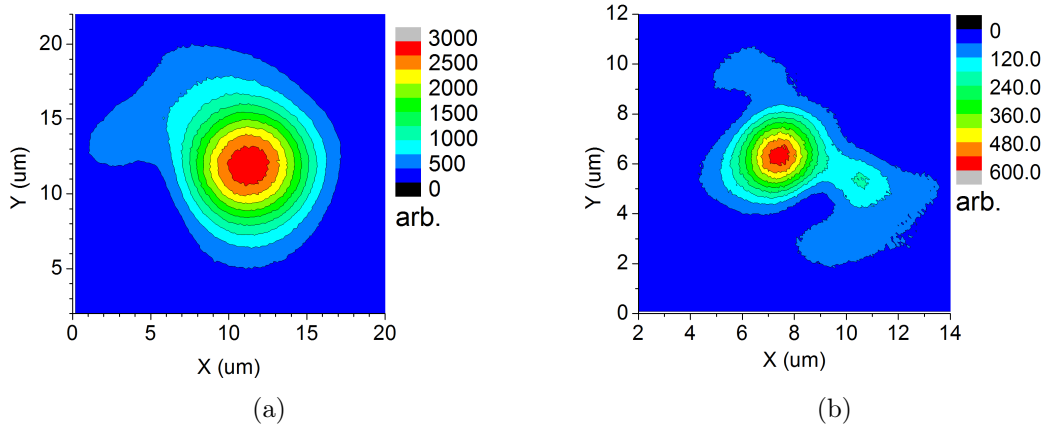


Figure 3.2: Intensity distributions of the focal-spots obtained for $f/6$ and $f/2$ optics after optimisation using adaptive optics. The images are in linear colormap with arbitrary units.

400 nm central wavelength, equation 3.1 yields $\Delta\tau_2 = 30.05 \text{ fs} \approx \Delta\tau_1$.

To be able to detect any energetic particles that might have been accelerated in the laser's forward direction, several diagnostics were installed and used during the experiment. Electrons of energies $> 5 \text{ MeV}$ could have been detected using the electron spectrometer covering a half opening angle of 0.05° ($900 \mu\text{rad}$) and its beam profile could be monitored using a Lanex screen placed before the spectrometer. The kinetic energies of the accelerated ions could have been measured using the combination of a scintillator screen (BC-422Q by Saint-Gobain Crystals) covering an observation half-angle of 23° (0.4 rad) and a Gatable-CCD (G-CCD) camera with sub-nanosecond resolution. In practise, its temporal resolution was limited to $30 - 40 \text{ ns}$ due to the jitter in the reference signal obtained from the laser system. Therefore, the G-CCD was operated outside the time-window, within which there was real danger of detection parts of the main laser pulse that could potentially damage or destroy the G-CCD. The scintillator screen (which was not covered by any light shielding element e.g. a thin aluminium foil) was sensitive to most of the energetic particles shown in fig. 3.3a by emitting light with a response time of $\sim 100 \text{ ps}$. The G-CCD was placed in such a way that it looked at the backside of the scintillator screen and its shutter opening time of the G-CCD was chosen in such a way that it predominantly looked for the accelerated Argon ions. Figure 3.3b shows that due to the heavier nature ($\sim 70,000m_e$) of Argon ions, their arrival time at the screen is on a nanosecond time scale, which is much slower than the energetic electrons and photons of the same energy. The G-CCD was thereby sensitive to ions of energies $< 5 \text{ MeV}$.

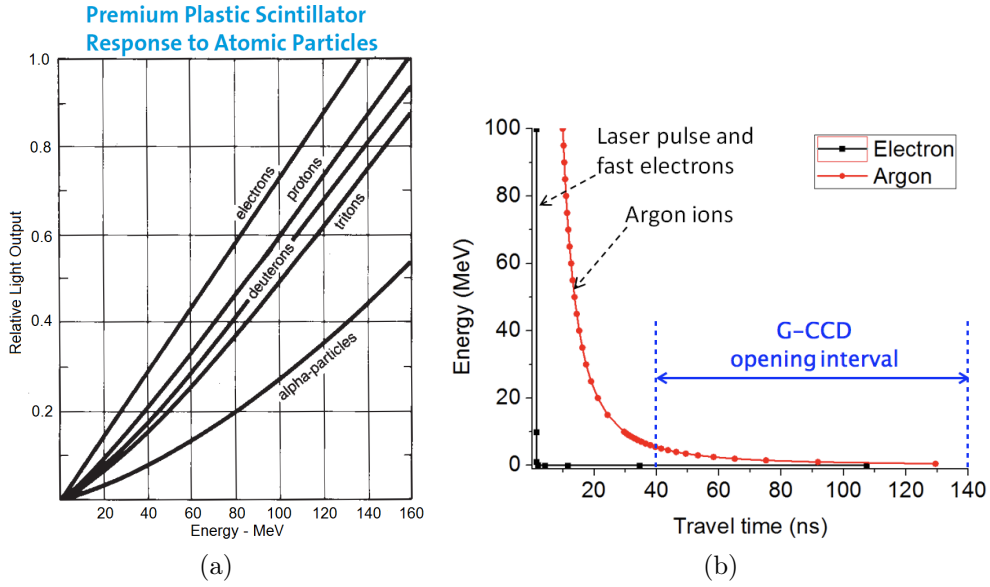


Figure 3.3: (a) Response of the scintillator screen BC-422Q for various energetic particles¹⁶³, and (b) Opening time setting of the G-CCD camera.

3.1.2 Interferometry Diagnostic

In order to measure the plasma density during the high intensity laser-plasma experiments, two types of interferometers, namely a Nomarski and a Mach-Zehnder interferometer have been used.

Nomarski Interferometry

Figure 3.4a shows the layout of the Nomarski interferometer, where a Wollaston prism is placed after the focal spot of the imaging objective and it is oriented at 45° to the incoming laser's polarisation direction, after which the incoming laser beam is split into two angularly separated and orthogonally polarised laser beams. The 45° polariser placed after the prism ensures that the two initially orthogonally polarised laser beams again have the same polarisation and can then interfere, as shown in fig. 3.4a. The angular separation of the beam, which is determined by the chosen Wollaston prism, is such that part of the diverging laser beam, which contains the desired phase shift is overlapped with the undisturbed part of the diverging second beam. The Nomarski interferometer has the advantage of yielding an inherent temporal synchronisation between the two beams. The resolution of the interferogram, according to Nyquist sampling rate, is limited to $2.6 \mu\text{m}$ corresponding to the calibration factor of the interferogram $1.3 \mu\text{m}/\text{px}$. Whereas, the Abbe limit corresponding a numerical aperture of 0.23, and wavelength of $0.4 \mu\text{m}$ is $0.9 \mu\text{m}$.

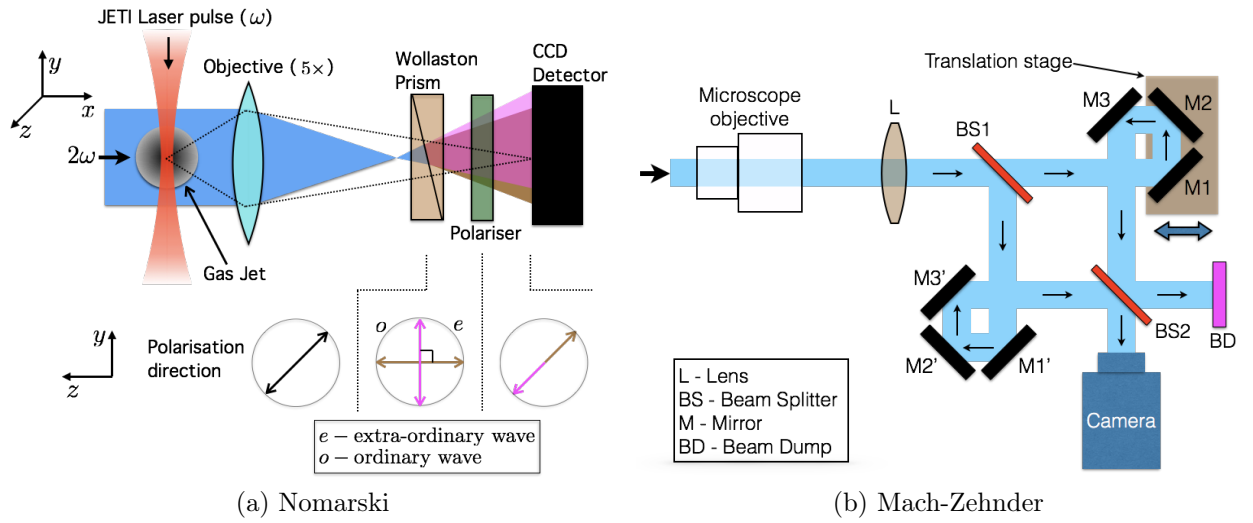


Figure 3.4: Schematic representation of the two different interferometric setups namely, (a) Nomarski and (b) Mach-Zehnder interferometers.

Mach-Zehnder Interferometry

In the second experiment conducted at JETI40, Mach-Zehnder interferometer was used to investigate the laser-plasma interaction region, as it offers several advantages over the Nomarski interferometer. For instance,

- it offers greater control over the fringe spacing and orientation in the interferogram as the wave-front of each interfering beam can be individually controlled.
- As it constructed outside the vacuum chamber, it offers ease of alignment during the experiment
- Unlike the Nomarski interferometry, where the aperture size of the wollaston prism might limit the resolution of the interferogram, this methods avoids such a constraint (provided that the corresponding optical elements were large enough not to clip the beam).

The schematic layout of the Mach-Zehnder interferometer is shown in fig. 3.4b, where the lens L combined with the infinity correctly microscope objective images the laser-plasma interaction region onto a camera. After the lens, the laser beam is split into two replicas using the beam-splitter BS1. It is important to note that unlike a conventional Mach-Zehnder interferometer, the laser beam is split after it passes through the interaction region (like a shearing interferometer) so that the whole unit can be constructed in a compact way and placed outside the vacuum chamber. Each replica then traverses in a separate arm, after which they are combined using the beam splitter BS2 as shown in

fig. 3.4b. This way, the part of the laser beam with desired phase-shift is made to overlap with the undisturbed portion of the second beam using the set of mirrors present in both arms. The temporal overlap of both beams after BS2 is achieved by making sure that the paths travelled by both beams are of equal length using the translation-stage present in one of the arms. The resolution of the interferogram, corresponding to Nyquist sampling rate, is limited to $0.66\ \mu\text{m}$, which is twice the calibration factor of the interferogram $0.33\ \mu\text{m}/\text{px}$. Whereas, the Abbe limit corresponding to the numerical aperture of 0.4, and wavelength of $0.4\ \mu\text{m}$ is $0.5\ \mu\text{m}/\text{px}$. An optical spectrometer (range: $340 - 1020\ \text{nm}$) was also placed on the other exit arm to analyse the spectrum of the radiation emitted from the laser-plasma interaction region.

3.2 Gas Nozzle Characterisation

Gas nozzles of two different geometries have been used to produce near-critical plasma during the experimental campaigns at JETI40. These nozzles correspond to subsonic and transonic flow geometries. The density distribution across the gas-jets produced by the nozzles under varying backing pressures have been measured using Mach-Zehnder interferometry. The characterisation was carried out well before the actual high-intensity laser-plasma experiments. Although several nozzles of diameters ranging from $300 - 500\ \mu\text{m}$ have been characterised, only the results obtained for nozzles of $400\ \mu\text{m}$ and $700\ \mu\text{m}$ outlet diameters, which were subsequently used at JETI40, are presented here.

3.2.1 Valve-Nozzle Construction

The nozzles that were used during the laser-plasma experiments were mounted on a Parker solenoid valve (Series 9, Part no.: 009-1669-900) that is capable of operating up to 80 bar backing pressure. The internal structure of the valve assembly is shown in fig. 3.5a, where the flow path is indicated. The flow between the valve and the nozzle is controlled by the poppet, which is mounted inside the plunger and pressed against the valve body with the help of a spring and the gas backing pressure. When the coil structure mounted on the outer body of the valve is energised using a DC voltage ($28\ \text{V}$), a magnetic-field is created inside the coil, which magnetises the plunger. This way, the plunger is pulsed downwards, thereby letting the gas to flow through the resulting gap between the poppet and the valve body. This process has a response time of $\sim 2\ \text{ms}$. When the electric current through the coil is stopped, the plunger is pushed back again by a spring mounted inside to block the gas flow.

The nozzles were designed in such a way that they can be directly mounted on the valve assembly. The subsonic nozzle shown in figs. 3.6a and 3.6b consists of a convergent-parallel flow section. As the gas flows through the convergent section of the nozzle (shown in red in fig. 3.6b), its velocity continues to increase reaching a maximum value of Mach 1

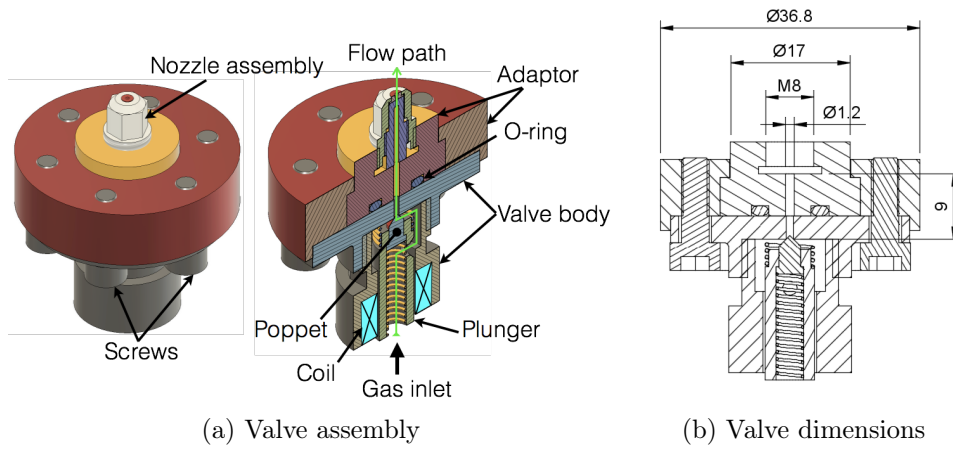


Figure 3.5: (a) 3D view of the Parker valve (Series 9, part no.: 009-1669-900) along with its radial section view indicating its various internal components along with the adaptor plates and the nozzle assembly mounted on top of it, and (b) the important dimensions of the valve assembly without the nozzle.

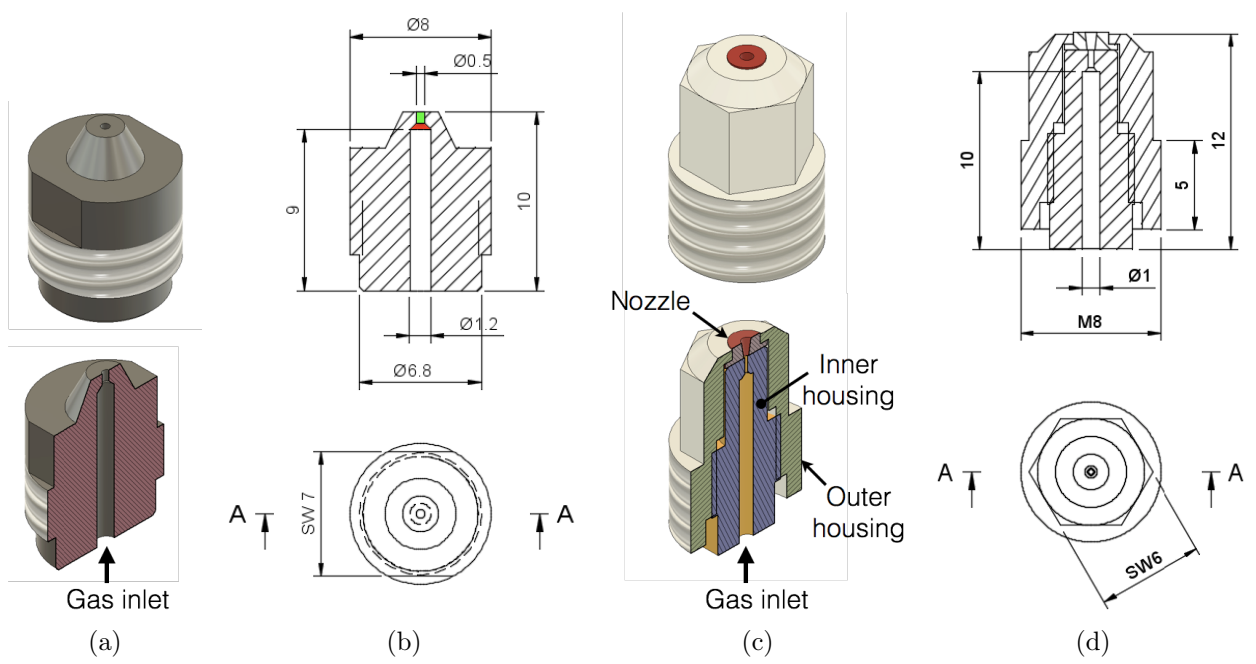


Figure 3.6: (a) 3D view of the subsonic nozzle along its cross section, (b) its important dimensions, (c) 3D view of the transonic nozzle assembly, where the nozzle (Hutblende) is mounted inside a housing because of its small dimensions, and (d) the dimensions of the nozzle housing.

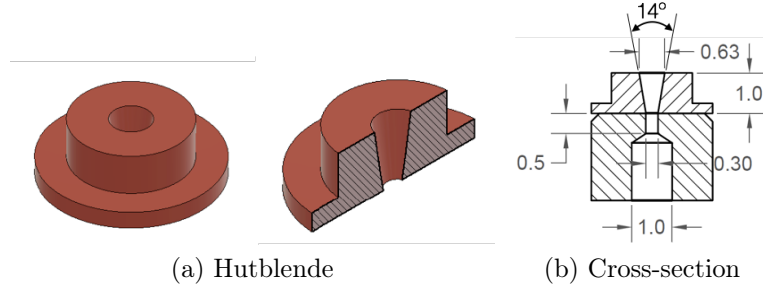


Figure 3.7: (a) 3D view of the transonic nozzle along with its cross-section, and (b) its important dimensions along with part of the inner housing's flow section.

at the throat section where the cross section of the nozzle remains unchanged (i.e. at the parallel flow section shown in green in fig. 3.6b), where the flow is said to be choked¹⁶⁴. This means that any further decrease in pressure along the downstream gas flow do not result in an increased mass flow rate i.e. its flow velocity remains constant. Therefore, this type of nozzle results in a subsonic flow during the free space expansion, whose density distribution measurements will be discussed in the measurement section 3.2.3.

The transonic nozzle assembly is shown in figs. 3.6c and 3.6d, where the divergent section of the nozzle shown in fig. 3.7a is mounted inside a housing. Together with the flow region inside the inner housing, it forms a convergent-divergent flow section, as shown in fig. 3.7b. The divergent section of the nozzle enables the gas flow to reach supersonic velocities at the nozzle exit¹⁶⁵. The exact density distribution profile however depends on the length and divergence angle of the divergent flow section. The measurement section 3.2.3 similarly describes the corresponding measured density distribution of the resulting gas-jet.

The exit velocity (v_0) of the central flow region of such a nozzle can be estimated from the formula¹⁶⁵:

$$v_0 = \left[\frac{TR}{M} \frac{2\gamma}{\gamma - 1} \left(1 - \left[\frac{P_o}{P_i} \right]^{(\gamma-1)/\gamma} \right) \right]^{1/2} \quad (3.2)$$

where T is the inlet temperature, the universal gas constant $R = 8.314 \text{ kgm}^{-2}\text{mol}^{-1}\text{K}^{-1}\text{s}^{-2}$, M is the molar mass, γ is the ratio of the specific heats of the gas at constance pressure and constant volume ($\gamma = 1.67$ for monoatomic gas), P_i and P_o are the inlet and outlet pressures, respectively. For example, for argon gas jet with parameters $M_{\text{Ar}} = 40 \text{ g/mol}$, $T = 300 \text{ K}$ and $P_o/P_i = 0.1$, the exit velocity $v_0 = 1.27 \text{ M}$ (M - Mach number), which is supersonic.

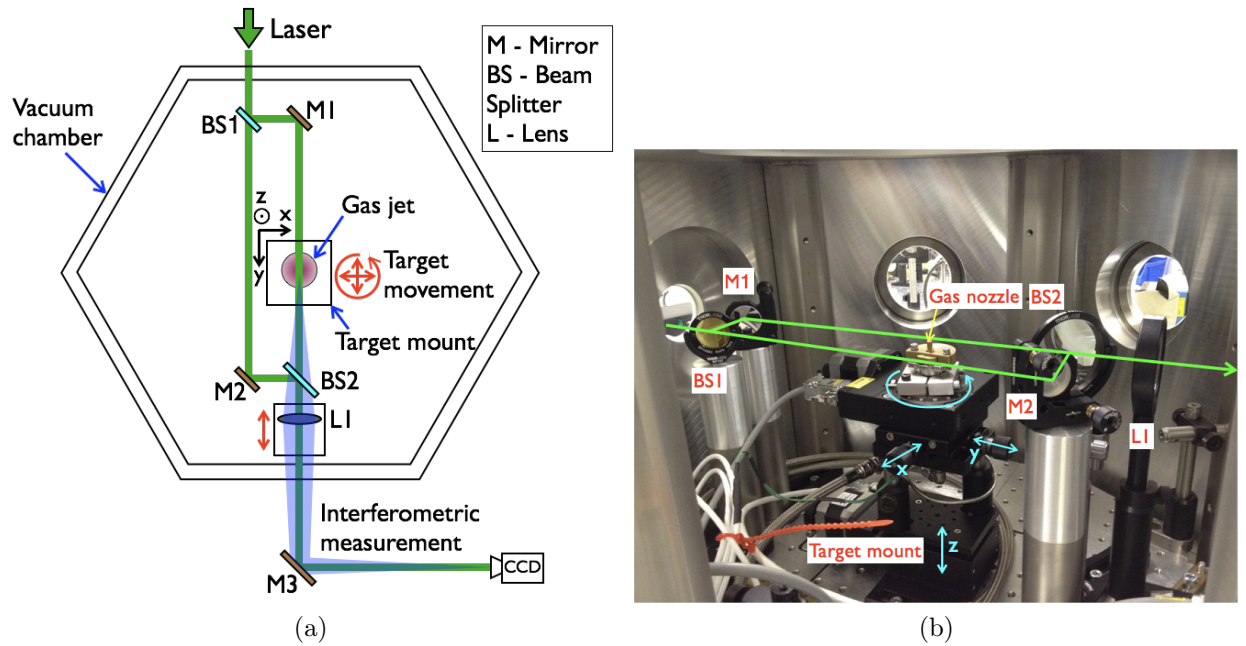


Figure 3.8: (a) Schematic layout of the Mach-Zehnder interferometer showing the optical layout and the positioning of the gas jet, and (b) a look into the vacuum chamber showing the construction of the optical mounts and the target (gas jet) positioning system.

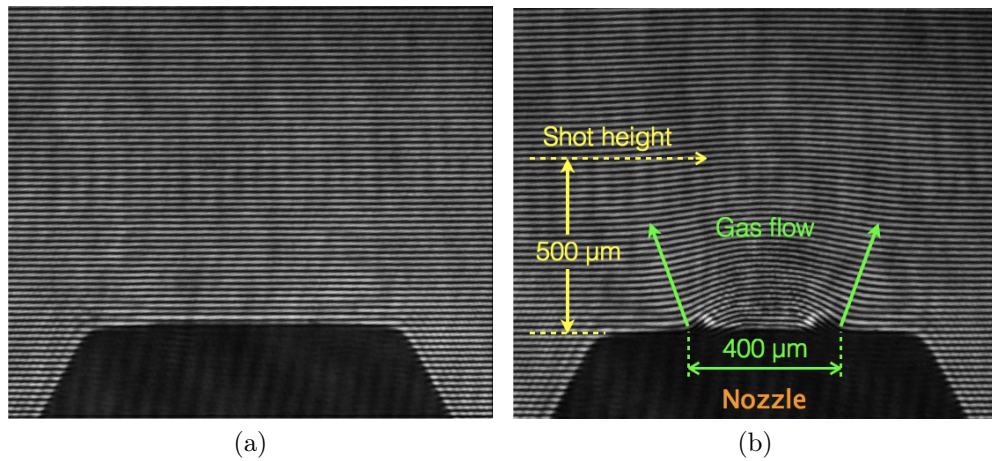


Figure 3.9: Sample interferograms obtained (a) in the absence of gas flow showing the fringe spacing and alignment with respect to the nozzle surface, and (b) during the steady-state argon gas flow for 400 μm outlet diameter nozzle and 50 bar backing pressure, where the visible fringe shift next to the nozzle outlet can be shown to correspond to the gas density distribution of the gas jet.

3.2.2 Mach-Zehnder Interferometer

The Mach-Zehnder interferometry technique is used to measure the phase shift accumulated by a laser pulse propagating through the gas jet, which can then be related to its density distribution. The schematic layout of the Mach-Zehnder interferometer used for the gas nozzle characterisation is shown in fig. 3.8a, where laser pulses of 532 nm central wavelength and 10 ns FWHM pulse duration were used.

It shows that a laser pulse is divided into two replicas using the beam splitter (BS1), after which one beam passes through the gas jet and the other one simply traverses the interferometer in a parallel path of identical geometric length. The phase shift accumulated by the part of the laser pulse propagating through the gas jet can be obtained by overlapping it with its undisturbed replica using the beam splitter BS2. The objective L1 placed after BS2 then images the gas jet onto a CCD camera, where an interferogram with the desired fringe pattern (as shown in fig. 3.9a) can be recorded by tilting the phase front of the reflected beam using BS2. During the steady-state gas flow, the phase shift caused by the gas jet is made visible by the bending of the fringes in the interferogram, as shown in fig. 3.9b.

3.2.3 Interferogram Analysis

The steps involved in analysing the interferogram is shown in fig. 3.10a in the form of a flow chart, whereby the radial density distribution of the gas jet $\rho(r)$ can be obtained from the phase shift $\Delta\phi(x)$ present in the interferogram. Here, $\Delta\phi(x)$ represents the additional phase difference accumulated by the laser-pulse propagating through the gas jet in comparison to the laser pulse replica traversing in the other arm of the interferogram, which is termed the integrated phase shift. Figure 3.10b shows such a scenario, where the laser pulse is shown to traverse a radial cross-section of the gas jet, which results in the integrated phase shift $\Delta\phi(x)$.

A cylindrically symmetric nozzle, such as the one used in our case, is expected to result in a symmetric radial density distribution $\rho(r)$ and thereby a symmetric integrated phase $\Delta\phi(x)$, as shown in fig. 3.10b (black solid-line). However, in practice, due to manufacturing imperfections and/or inaccurate nozzle alignment, a slight asymmetry might result in the gas density distribution, which in turn might result in an asymmetric integrated phase $\Delta\phi(x)$, which is also shown in fig. 3.10b (red dashed-line). In both cases, the radial phase shift $\Delta\phi_r(r)$ can be determined from the integrated phase shift $\Delta\phi(x)$ using the generalised Abel inversion method¹⁶⁶, where the asymmetry in $\Delta\phi(x)$ is assumed to result from a radial gas density distribution $\rho(r)$ (and therefore $\Delta\phi_r(r)$) that is only asymmetric with respect to y-axis (i.e. it is symmetric with respect to x-axis), as shown in fig. 3.10c.

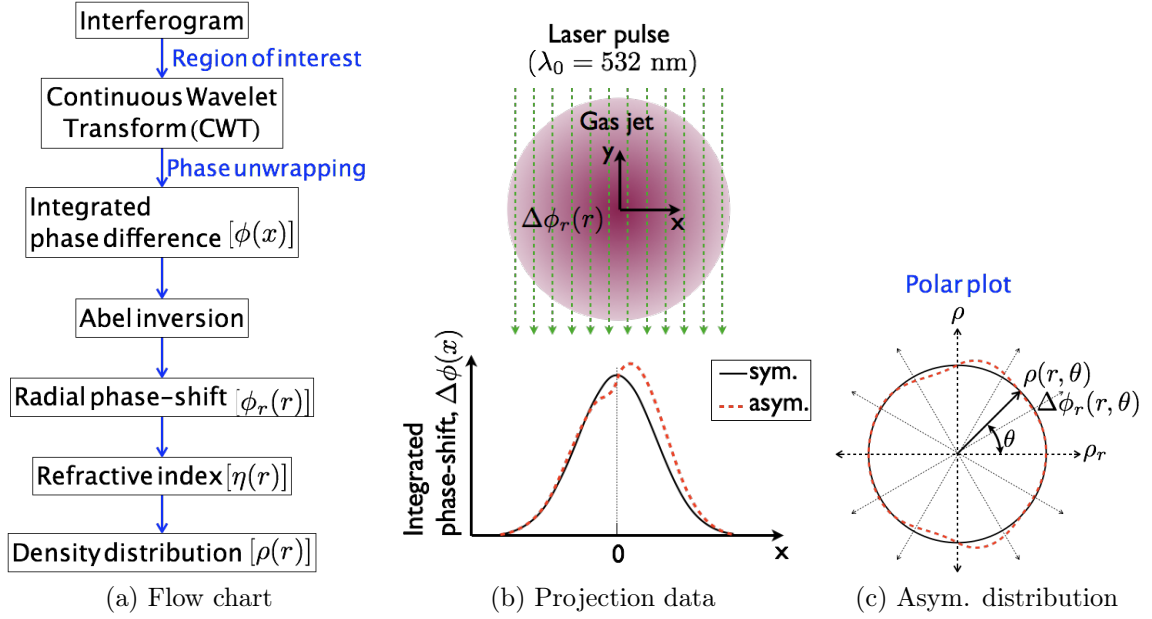


Figure 3.10: (a) Steps involved in obtaining the gas density distribution from an interferogram, (b) additional phase shift acquired by the laser pulse propagating through a radial cross-section of the gas jet, and (c) asymmetric distribution of the radial gas density $\rho(r)$ and phase shift $\Delta\phi(r)$.

Mathematical Formulation

At a given height above the nozzle surface ($z = z_0$), the 1D integrated phase-shift $\Delta\phi(x)$ accumulated by the laser pulse can be seen as the projection of the 2D radial phase shift distribution $\Delta\phi_r$ onto x-axis (as shown in fig. 3.10b), which in its mathematical form can be written as¹⁶⁷,

$$\Delta\phi(x, z_0) = 2 \int_x^\infty \frac{r \Delta\phi_r}{\sqrt{r^2 - x^2}} dr \quad (3.3)$$

It shows that the integrated phase $\Delta\phi(x)$ at x is affected by all the values of the radial phase shift $\Delta\phi_r(r)$ at and above x (i.e. $r \geq x$). If the radial phase shift $\Delta\phi_r(r)$ can be assumed to take the asymmetric distribution of the form¹⁶⁶:

$$\Delta\phi_r(r, \theta, z_0) = \Delta\phi_0(r, z_0) + \Delta\phi_1(r, z_0) \cos \theta \quad (3.4)$$

where $\theta = x/r$. Therefore, $\Delta\phi_p$ can be written as,

$$\Delta\phi(x, z_0) = 2 \int_x^\infty \frac{r}{(r^2 - x^2)^{1/2}} \left(\Delta\phi_0 + \Delta\phi_1 \frac{x}{r} \right) dr \quad (3.5)$$

$$= 2 \int_x^\infty \frac{r\Delta\phi_0}{(r^2 - x^2)^{1/2}} dr + 2x \int_x^\infty \frac{\Delta\phi_1}{(r^2 - x^2)^{1/2}} dr \quad (3.6)$$

$$= \underbrace{\hspace{10em}}_{\Delta\phi_s} + \underbrace{\hspace{10em}}_{\Delta\phi_a} \quad (3.7)$$

Thus, the resulting integrated phase $\Delta\phi_p$ can be understood to be a combination of the symmetrical and asymmetrical phase shift components: $\Delta\phi_s$ and $\Delta\phi_a$. Therefore, once if these components are known, their respective radial phase shift factors $\Delta\phi_0$ and $\Delta\phi_r$ can be obtained by the so called Abel inversion integral of the form¹⁶⁶⁻¹⁶⁸:

$$\Delta\phi_0(r, z_0) = -\frac{r}{\pi} \int_r^\infty \frac{d[\Delta\phi_s]/dx}{\sqrt{x^2 - r^2}} dx; \quad \Delta\phi_1(r, z_0) = -\frac{r}{\pi} \int_r^\infty \frac{d[\Delta\phi_a]/dx}{\sqrt{x^2 - r^2}} dx \quad (3.8)$$

These integrals show that the inversion process depends on the derivative of the projection data meaning that it depends on the variation of the projection data with respect to its neighbourhood. Therefore, if the projection data were to contain strong fluctuations due to the presence of noise, it is important to smoothen it first to avoid the noise being amplified during the inversion process. For the purpose of numerical implementation, the Abel inversion integral can be written as,

$$\Delta\phi_r(r_i, z_0) = \frac{1}{\Delta x} \sum_{j=0}^{\infty} D_{ij} \Delta\phi_p(x_j, z_0) \quad (3.9)$$

where, Δx is the spacing between the successive data points and D_{ij} are the Abel inversion coefficients, which can be calculated using a method called ‘onion-peeling’, as discussed in the article by Dasch¹⁶⁷. Here, D_{ij} acts as a differential operator and it is independent of the projection data.

Phase-shift Extraction

The phase shift contained in the interferograms can be extracted using a technique called Continuous Wavelet Transform (CWT). In this method, a 1D continuous spatially (or time) dependent signal is transformed into a 2D space-scale (or time-scale) complex domain, where the strength of its coefficients denote the phase shift values. A short mathematical description of this method is given in this section, whereas a more detailed description can be found in the article by Tomassini et al¹⁶⁹.

After selecting an appropriate region of interest (ROI) from the interferogram, such as the one shown in fig. 3.11a containing the gas flow region, each pixel column $f(x_i, z)$

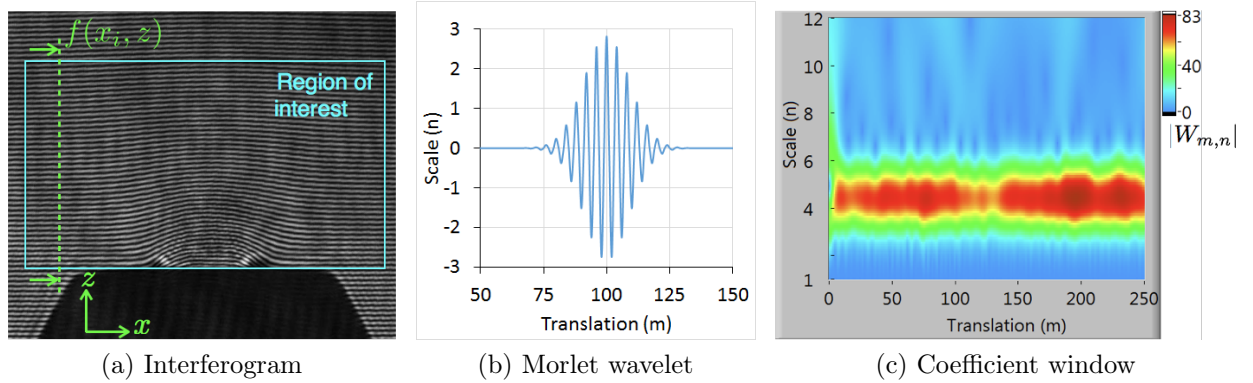


Figure 3.11: (a) Interferogram showing the region of interest section, (b) absolute part of the Morlet wavelet for $m = 100$, $n = 4.5$, $\sigma = 2$ and $k = 3\pi/2$ and (c) window containing the absolute value of the complex coefficients obtained using the continuous wavelet transform method for a pixel column of the interferogram image.

of the image is made to undergo CWT to yield complex wavelet coefficients W_{mn} of the form:¹⁶⁹

$$W_{mn}(x_i, z) = \int_{-\infty}^{\infty} f(x_i, z) \psi_{mn}^*(z) dz \quad (3.10)$$

where

$$\psi_{mn}(z) = \frac{1}{\sqrt{n}} \psi\left(\frac{z - m}{n}\right); \quad \begin{array}{l} m = 1, 2, 3, \dots [\text{no. of rows}] \\ n = 1, 0.1, 0.2, \dots, 13 \end{array}$$

Here, the function $\psi(z)$ is called the ‘Mother wavelet’, which is a complex valued oscillatory function that can be translated (m) and scaled (n) to obtain multiple ‘Daughter wavelets’ $\psi_{mn}(z)$ whose complex conjugates are used as a weighing function. The magnitude of the scaling factor n is chosen according to the fringe spacing, and its factor of increment ($\Delta n = 0.1$) helps to localise wavelet coefficients W_{mn} , which help to extract the phase information contained in the interferogram.

Though there are multiple forms of mother wavelets available, the so-called ‘Morlet wavelet’ will be used in this analysis, as it provides a very good spatial and frequency localisation depending on the translation (m) and scaling (n) factors. The Morlet wavelet assumes the form of a plane wave modulated by a Gaussian function, as shown in fig. 3.11b and it can be expressed as¹⁷⁰,

$$\psi(z) = \frac{1}{\sqrt[4]{\sigma^2 \pi}} \exp\left[-\frac{z^2}{2\sigma^2} + jkz\right] \quad (3.11)$$

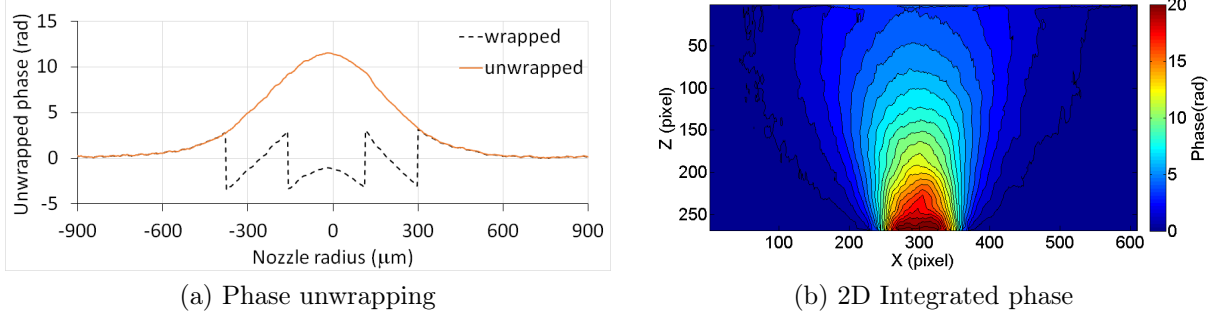


Figure 3.12: (a) Process of phase unwrapping, where a 2π phase either added or subtracted at the discontinuities present in the extracted phase, and (b) resulting 2D phase distribution extracted from the interferogram corresponding to 50 bar backing pressure.

where, σ is the standard deviation, and j is the imaginary unit and k is the wave number.

Thus, for each column of the ROI, equation 3.10 yields a set of 2D complex wavelet coefficients W_{mn} corresponding to varying translation (m) and scaling (n) factors, whose absolute part $|W_{mn}|$ is shown in fig. 3.11c. The phase values $\Delta\vartheta(x_i, z)$ corresponding to the selected column $f(x_i, z)$ of the interferogram can be obtained by first determining the scaling factor (n_0) at which the maximum value of $|W_{mn}|$ is reached for each translation factor m and then determining the ratio between the imaginary (\Im) and real (\Re) part of the respective wavelet coefficient W_{mn_0} , as given by

$$\Delta\vartheta(x_i, z) = \tan^{-1} \left[\frac{\Im(W_{mn_0})}{\Re(W_{mn_0})} \right], \quad i = 1, 2, \dots [\text{no. of columns}] \quad (3.12)$$

Repeating this process for the entire ROI, one obtains the corresponding 2D phase values $\Delta\vartheta(x, z)$. Equation (3.12) indicates that $\Delta\vartheta(x, z)$ varies only between $-\pi$ and π and thereby introduces discontinuities or phase jumps in the resulting phase. Therefore, each row $\Delta\vartheta(x, z_m)$ of the 2D phase is made to undergo the so called phase unwrapping process, whereby a factor 2π is either added to or subtracted from $\Delta\vartheta$ at the discontinuities such that it yields a continuously varying signal¹⁷¹, as shown in fig. 3.12a. After the phase unwrapping process, the resulting 2D phase distribution still contains a tilted plane of additional phase that was introduced across the interferogram to obtain the desired fringe spacing and orientation, which needs to be subtracted. Thus, the 2D integrated phase-shift $\Delta\phi_p(x, z)$ present in the interferogram can be obtained, an example of which is shown in fig. 3.12b.

Density Analysis

The corresponding symmetric ($\Delta\phi_s$) and asymmetric ($\Delta\phi_a$) phase shift components can be obtained from the measured phase shift $\Delta\phi_p$ by first splitting $\Delta\phi_i$ with respect to the

nozzle centre in the following way,

$$\Delta\phi_i^-(\xi, z_0) = \Delta\phi_i(-x, z_0), \text{ for } x < 0; \quad (3.13)$$

$$\Delta\phi_i^+(\xi, z_0) = \Delta\phi_i(x, z_0), \text{ for } x > 0, \quad (3.14)$$

$$\Delta\phi_i^0(\xi, z_0) = \Delta\phi_i(x, z_0), \text{ for } x = 0, \text{ where } \xi = |x| \quad (3.15)$$

and then by setting

$$\Delta\phi_s = \frac{1}{2}(\Delta\phi_i^- + \Delta\phi_i^+) + \Delta\phi_i^0(\xi, z_0); \quad \Delta\phi_a = \frac{1}{2}(\Delta\phi_i^- - \Delta\phi_i^+) + \Delta\phi_i^0(\xi, z_0) \quad (3.16)$$

The corresponding symmetric ($\Delta\phi_0$) and asymmetric ($\Delta\phi_1$) radial phase shift components can be obtained using the ‘onion peeling’ method (as discussed in the previous section), from which the resultant asymmetric 2D radial phase-shift $\Delta\phi_r$ can be constructed using

$$\Delta\phi_r(r, \theta, z) = \Delta\phi_0(r, z) + \Delta\phi_1(r, z) \cos \theta \quad (3.17)$$

However, in the limit of $\Delta\phi_a \rightarrow 0$, one can directly resort to the symmetric Abel inversion process¹⁶⁷. Figure 3.12b shows that the region immediately above the nozzle exit exhibits an asymmetric behaviour, but evolves into a more uniform distribution with respect to the nozzle axis. At a height of 500 μm above the nozzle edge, which is of interest to us, the gas jet exhibits a nearly symmetric distribution, as shown in fig. 3.13a. The resultant radial phase shifts obtained through the symmetric and asymmetric Abel inversion processes are shown in fig. 3.13b, where it can be seen that the difference is minimal. Therefore, it was decided that the symmetric Abel inversion be used for the radial phase shift analysis.

Figure 3.13b shows the corresponding resultant radial phase shifts obtained through the symmetric and asymmetric Abel inversion processes. The radial phase shift $\Delta\phi_r$ acquired by the laser pulse can be related to the refractive index of the medium η in the following way,

$$\eta = 1 + \Delta\eta = 1 + \frac{\lambda_0}{2\pi} \frac{\Delta\phi_r}{l} \quad (3.18)$$

where, λ_0 is the central laser wavelength in vacuum, $\Delta\eta$ is the change in refractive index and l is the propagation length. The corresponding number density distribution ρ_r of the gas-jet can then be obtained using the *Lorentz-Lorenz* relation, as shown below,

$$\rho_r = \frac{3}{4\pi\alpha} \left(\frac{\eta^2 - 1}{\eta^2 + 2} \right) \quad (3.19)$$

where, α is the molecular polarisability ($\alpha_{\text{Ar}} = 1.642 \pm 0.001 \text{ \AA}^3$).

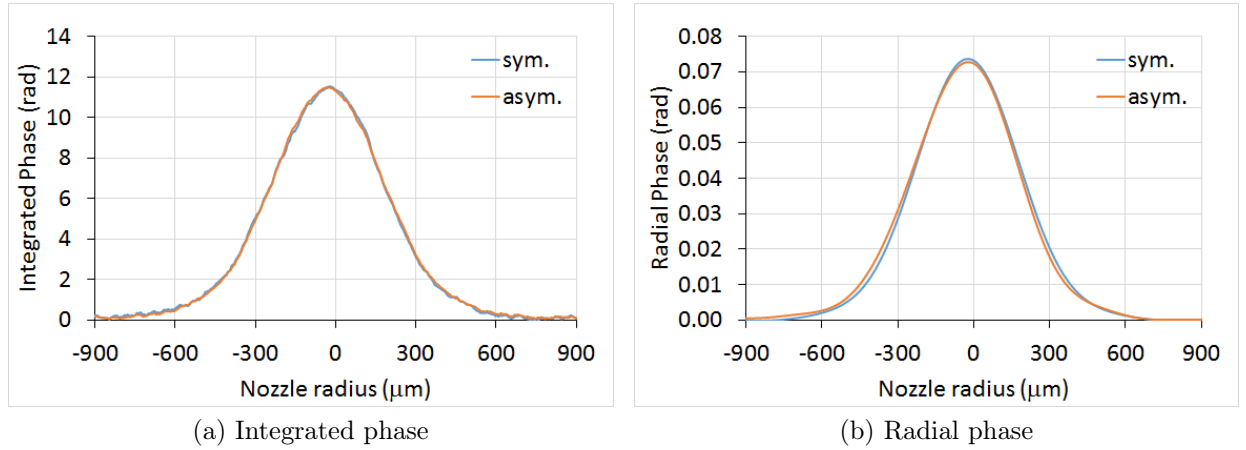


Figure 3.13: (a) Comparison between the symmetric and asymmetric integrated phase lineouts, and (b) comparison between the radial phase shifts obtained using the symmetric and asymmetric Abel inversion methods.

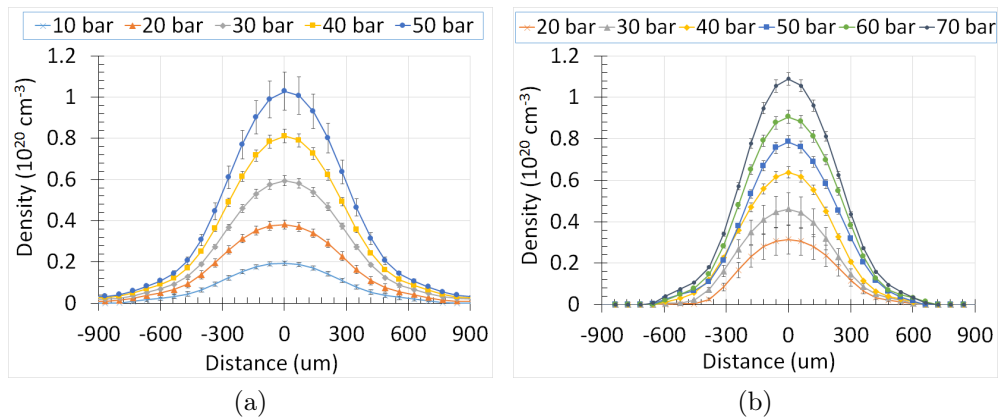


Figure 3.14: Radial number-density distribution of (a) subsonic and (b) transonic argon gas-jets at a height of $500 \mu\text{m}$ above the nozzle's exit for varying backing pressures.

Density Measurements

Figure 3.14 shows the radial atomic number distribution across the subsonic and transonic gas jets obtained at a height of $500 \mu\text{m}$ above the nozzle edge for varying backing pressures. A subsonic gas jet is usually characterised by its Gaussian-like distribution with a long tail of decreasing radial gas density distribution at the edges, whereas a transonic gas jet is characterised by its relatively shorter (radial) tail. It is important to note that the exit diameters of the subsonic and transonic nozzles are $400 \mu\text{m}$ and $650 \mu\text{m}$, respectively. Therefore, fig. 3.14 shows that for nozzle with an exit diameter 1.6 times greater than that of the subsonic nozzle, one obtains a gas jet with relatively shorter (radial) tail region but with a slightly lower peak gas density, which can, however, be adjusted by using a higher backing pressure.

The exact flow dynamics of these nozzles can only be understood with the help of flow analysis softwares such as, ANSYS (Fluent). But here, we are only interested in the density distribution of the gas-jet. It can be seen from figs. 3.14a and 3.14b that it is possible to reach the critical density of $1.72 \times 10^{21} \text{ cm}^{-3}$ at the central region of the gas distribution for $\geq \text{Ar}^{10+}$ ionisation level. Therefore, for a given ionisation level, the desired plasma density can be achieved by varying the nozzle backing pressure, even when the laser intensity is kept constant.

Chapter 4

Results and Discussion

A discussion on the results obtained from the two subsequent high-intensity laser-plasma experiments conducted at the JETI40 laser system is presented here, which were aimed at deepening the understanding of the laser-plasma interactions at near-critical densities.

4.1 June 2014 Experiment

In this experiment, laser pulses of 800 nm central wavelength, 30 fs FWHM pulse duration, and 550 mJ energy were focused into the middle of a subsonic gas jet (as described in the previous section) at a height of 500 μm above the nozzle edge using an $f/6$ off-axis parabola reaching a maximum intensity of $4.4 \times 10^{19} \text{ W/cm}^2$. The backing pressure of the argon gas nozzles was varied from 5 – 80 bar. The laser-plasma interaction region was imaged onto a CCD camera with an objective and backlighted using a second harmonic (2ω) probe beam of 400 nm at various temporal delays between the pump and probe beams. It must be pointed out that neither energetic electrons of kinetic energy $> 5 \text{ MeV}$ nor ions of kinetic energy $< 5 \text{ MeV}$ could be detected along the laser's forward propagation direction by their respective diagnostics. The absence of high energy electrons ($> 5 \text{ MeV}$) also rules out the possibility of the presence of ion energies $> 5 \text{ MeV}$. However, the images obtained using the side-view diagnostic show the existence of a preferential laser side-scattering mechanism during the laser-plasma interactions for varying nozzle backing pressures. Since this is an energy loss mechanism, by which laser energy can be transported away from the interaction region, this section aims to examine the possible origin of this process.

4.1.1 Side-view Images

Figure 4.1a shows a typical interferogram obtained using the side view diagnostics, where the laser pulse is focused to the centre of the gas jet. The clarity of the interference fringes is affected by the intensity modulations caused by the gas and plasma density distributions. The laser-gas jet interaction region shows that the intensity of the laser pulse surrounding the central FWHM focal region (as indicated by the green dotted-lines) is intense enough to ionize the Argon atoms at least to $\text{Ar}^{1+\dots 2+}$ states, thus making the

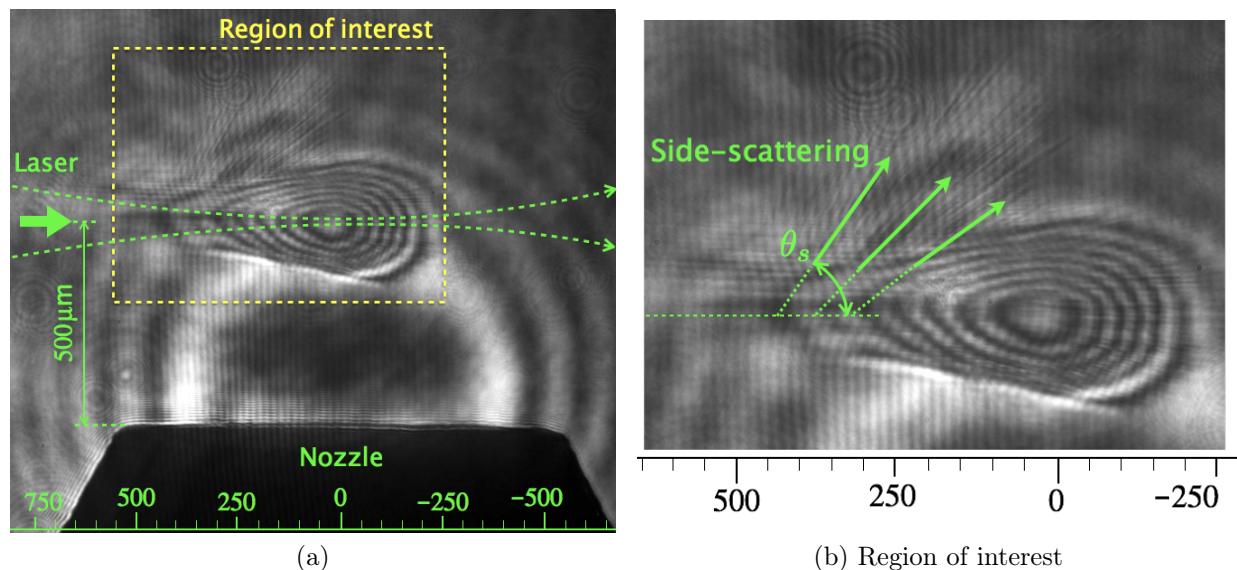


Figure 4.1: (a) Typical interferogram showing the laser-plasma interaction region, which was obtained for 11 bar nozzle backing pressure using Nomarski interferometer and (b) corresponding variation of the scattering-angle measured with respect to the laser axis along the laser propagation direction.

interaction region larger than expected. This also causes ambiguities in the interferograms, as it tends to refract the probe beam and causes intensity modulations in the interferograms. However, an interesting feature of the side-view image is the preferential side-scattering that could be seen propagating upwards from the interaction region, as shown in figure 4.1b. The scattering is made visible by the filamentary structure indicating ionisation caused by the intensity of the scattered light most likely originating from the central laser-plasma interaction region.

Figure 4.2 shows the side-view images obtained for varying backing pressures, where the phenomenon of side-scattering has been observed up to 40 bar backing pressure to varying degrees. As the laser pulse propagates from the outer edges of the gas jet towards the region of higher densities (centre), the scattering angle θ_s measured with respect to the laser's forward direction gradually decreases. For nozzle backing pressures: 20 and 40 bar, the scattering process is shown to undergo a gradual transition from positive (upwards) to negative angles (downwards), as shown in figs. 4.2e and 4.2f. At densities close to the critical density n_c , the laser pulse is expected to be strongly absorbed due to the (near) resonance between the laser and plasma frequencies. This is referred to as the *laser pulse collapse* by Sylla et al³⁶. Figure 4.2g shows that for backing pressure 60 bar, the intense parts of the laser pulse possibly gets stopped by the near-critical plasma due to near resonance between the laser and plasma frequencies, whereas only the less intense parts of the laser pulse undergoes the filamentation process. Figure 4.3c shows the

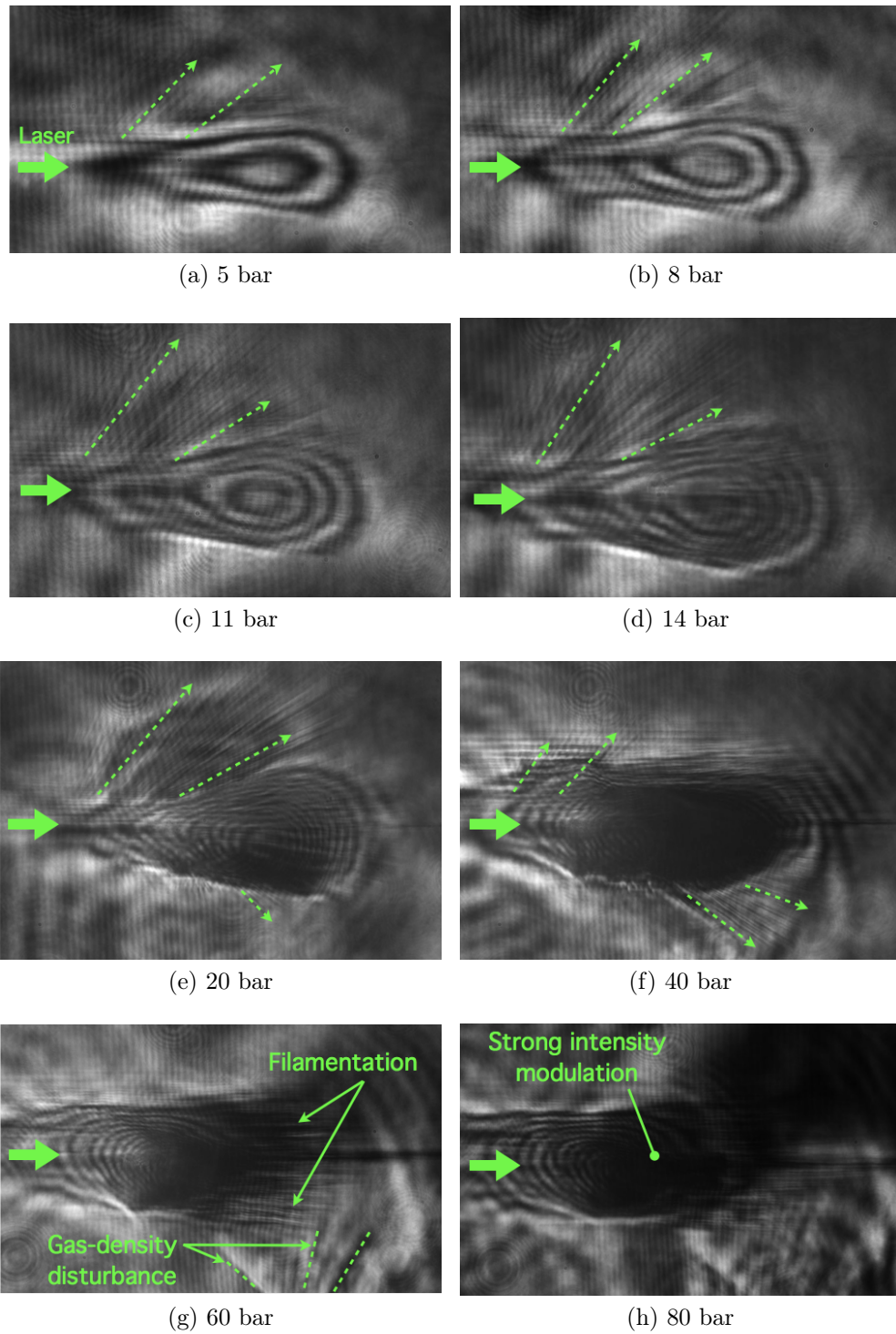


Figure 4.2: Side-view images obtained for nozzle backing pressures varying from 5 – 80 bar.

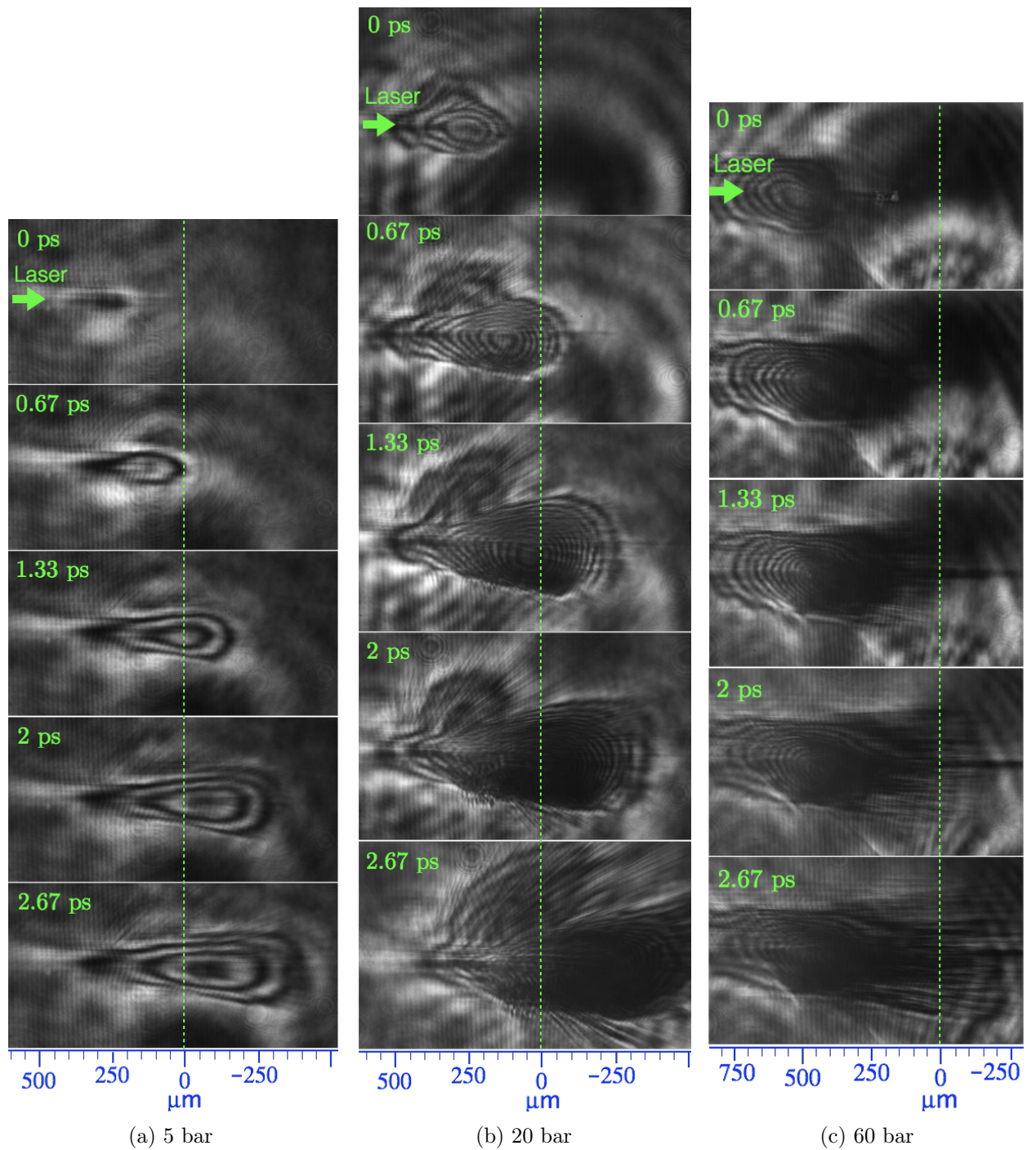


Figure 4.3: Side-view images obtained for varying pump-probe delay times showing the propagation of the laser pulse through the gas jet for backing pressures (a) 5 bar (b) 20 bar, and (c) 60 bar, where the dotted lines indicate the nozzle centre.

side-view images obtained for 60 bar pressure at various pump-probe time delays, where the propagation of the laser pulse through the gas jet and the subsequent filamentation process of the laser pulse, which starts to occur before the nozzle centre, could clearly be seen. The filamentation process refers to coupling between parts of the laser pulse and the transverse electron density perturbation^{151;152}, as discussed in 2.10.5. This results in bundles of EM-waves (filaments) across the laser beam, as shown in fig. 4.2g, which are guided forward by the local negative lens-like refractive index modulations created by the filaments itself. Figures 4.3a and 4.3b show the side-view images obtained for 5 and 20 bar backing pressures at various pump-probe delay times, where the propagation of the laser pulse through the gas jet past the nozzle centre could be seen. The gas jets corresponding to 5 and 20 bar pressures can be expected to result in peak plasma densities of $0.08n_c$ and $0.35n_c$, respectively. These densities correspond to the peak (vacuum) laser intensity of $4.1 \times 10^{19} \text{ W/cm}^2$ and the argon ionisation state of Ar^{16+} .

These images also show that their visibility is heavily affected the absorption and refraction of the probe beam energy (primarily) by the plasma density distribution created across the path of the main laser pulse. Increasing the probe beam energy any further does not necessary lead to better visualisation of the interaction region, as the plasma also acts a strong negative lens to refract the beam away from its initial propagation direction, which may not be collected by the objective lens used for the side-view diagnostic. Since the intense laser pulse propagates only $500 \mu\text{m}$ above the nozzle surface, repeated usage of the nozzle causes plasma induced damage to its outlet surface resulting in density disturbances immediately next to the nozzle surface, as shown in figure 4.2g.

4.1.2 Limitations of Interferometry

Although the Nomarski interferometry was originally employed in the side-view diagnostics to measure the electron density distribution across the laser-plasma interaction region, the intensity modulations caused by the plasma deteriorate the contrast of the resulting interferograms thus making them difficult to analyse. In fig. 4.4a, the central interaction region corresponding to Argon ionisation levels of $>\text{Ar}^{8+}$, whereas the surrounding region corresponds to Ar^{1-2+} , which results from the laser energy distribution around the focal region. Therefore, the substantial difference in the resulting electron-density between the outer and inner regions leads to a sharp increase in the phase-shift over a few micrometers. A simulation of this scenario is shown in fig. 4.4b, where the parameters are based on the corresponding experimental conditions. This sharp increase in the phase shift becomes indistinguishable from the surrounding region of the interferogram because of the strong intensity modulations thus rendering them difficult to analyse.

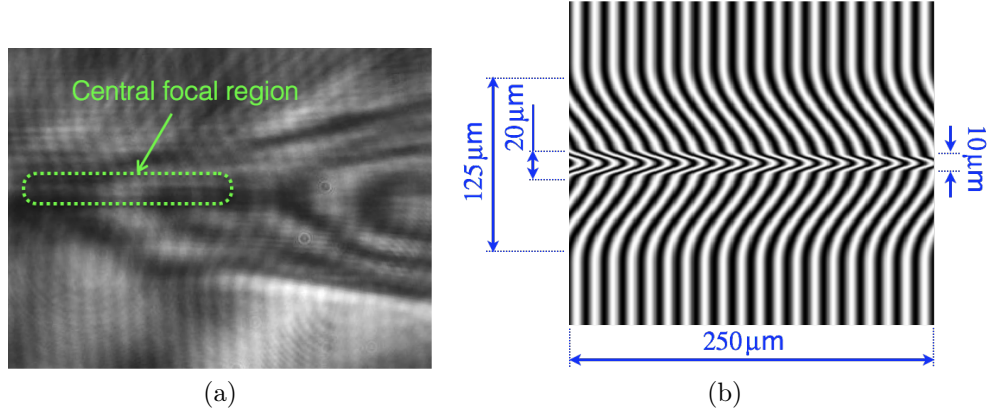


Figure 4.4: (a) A close-up view of the interferogram obtained for 11 bar backing pressure and (b) a simulated interferogram showing the fringe-shift (corresponding to the integrated phase-shift) caused for similar plasma density conditions. Here, the transverse electron density distribution is assumed to have a Gaussian distribution, where a maximum argon ionisation state of Ar^{8+} (corresponding to intensities $1.9 \times 10^{16} - 1.6 \times 10^{18} \text{ W/cm}^2$, which is calculated using the barrier suppression ionisation mechanism) is assumed for the central interaction region. Furthermore, the transition of the argon ionisation states is also assumed to be smooth i.e. no step-like profile.

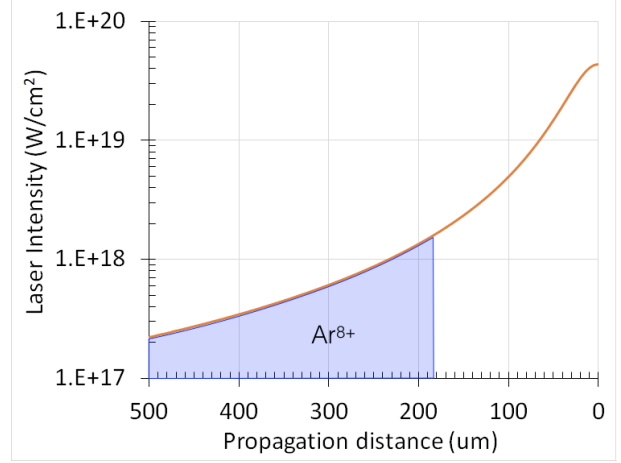
4.1.3 Electron Density Estimation

Since direct measurements of the electron density distribution (n_e) of the plasma along the laser's propagation direction are extremely difficult to obtain, it needs to be estimated from the combination of the gas density measurements and the laser focusing geometry. For peak laser intensities along the propagation axis shown in fig. 4.5b, the electron density n_e can be estimated by first assuming that the argon atoms are directly field ionised by the barrier suppression ionisation mechanism and then multiplying the ionisation factor with the gas density measurements. Figure 4.5a shows the laser intensity levels required to directly field ionise the argon atom to varying degrees, starting from the outermost electron shell. At distances of $300 - 650 \mu\text{m}$ from the nozzle centre over which side-scattering was observed, the laser intensity (corresponding to the focusing in vacuum) varies between $1 - 6 \times 10^{17} \text{ W/cm}^2$ corresponding to the time averaged Lorentz factor related to the electron motion $\langle \gamma_e \rangle$ of 1.03-1.13, where $\langle \gamma_e \rangle$ is related to the refractive index (η) of the plasma through $\eta = \sqrt{1 - n_e / \langle \gamma_e \rangle n_c}$. As discussed in section 2.9.2, at relativistic intensities, the laser self-focusing effects due to relativistic electron mass increase and ponderomotive electron expulsion are just beginning to play a role and tend to compensate the effect of ionisation induced defocusing.

A more accurate estimation of n_e would require a sophisticated and self-consistent 3D

Ionisation state	Atomic shell	Ionisation energy (eV)	Intensity (W/cm ²)
Ar ¹⁺	1s ² 2s ² 2p ⁶ 3s ² 3p⁵	15.8	2.50E+14
Ar ²⁺	1s ² 2s ² 2p ⁶ 3s ² 3p⁴	27.6	5.80E+14
Ar ³⁺	1s ² 2s ² 2p ⁶ 3s ² 3p³	40.7	1.20E+15
Ar ⁴⁺	1s ² 2s ² 2p ⁶ 3s ² 3p²	59.8	3.20E+15
Ar ⁵⁺	1s ² 2s ² 2p ⁶ 3s ² 3p¹	75.0	5.10E+15
Ar ⁶⁺	1s ² 2s ² 2p ⁶ 3s²	91.0	7.60E+15
Ar ⁷⁺	1s ² 2s ² 2p ⁶ 3s¹	124.3	1.90E+16
Ar ⁸⁺	1s ² 2s ² 2p⁶	143.5	2.70E+16
Ar ⁹⁺	1s ² 2s ² 2p⁵	422.4	1.60E+18
Ar ¹⁰⁺	1s ² 2s ² 2p⁴	478.7	2.10E+18
Ar ¹¹⁺	1s ² 2s ² 2p³	539.0	2.80E+18
Ar ¹²⁺	1s ² 2s ² 2p²	618.3	4.10E+18
Ar ¹³⁺	1s ² 2s ² 2p¹	686.1	5.20E+18
Ar ¹⁴⁺	1s ² 2s²	755.7	6.70E+18
Ar ¹⁵⁺	1s ² 2s¹	872.6	1.00E+19
Ar ¹⁶⁺	1s²	939	1.20E+19
Ar ¹⁷⁺	1s¹	3947	3.40E+21
Ar ¹⁸⁺	—	4264	4.10E+21

(a)



(b)

Figure 4.5: (a) Laser-intensity required to achieve successive Argon ionisation states starting from the outermost shell^{172?}, and (b) peak intensity variation along the laser's propagation axis corresponding to the vacuum focusing geometry, where the distances over which the peak ionisation of Ar⁸⁺ is expected to remain unchanged.

numerical simulations taking into account argon's successive ionisation steps across the laser pulse in each time step, the resulting plasma refractive index profile and various laser propagation effects in plasma such as, ionisation induced defocusing, relativistic and ponderomotive self-focusing, and self-phase modulation (SPM), which are described in the theory section. Furthermore, the ionisation state Ar⁸⁺ remains unchanged for laser intensities ranging from $1.9 \times 10^{16} - 1.6 \times 10^{18}$ W/cm² over distances shown in fig. 4.5b, where the side-scattering was observed. Therefore, any slight variations in the laser intensity within this range due to either focusing or defocusing effects do not lead to any measurable change in the ionisation state of the argon atoms. Therefore, although the electron density estimations might slightly deviate from the actual values, this discussion still helps to shed light into the phenomenon of side-scattering and understand its origin.

4.2 Scattering Measurement

Figure 4.6a shows the scattering angle measured for various nozzle backing pressures, where it can be seen that as the laser pulse propagates further towards the regions of higher gas density, the scattering angle θ_s decreases. Figure 4.6b shows the scattering angle measured for 20 bar backing pressure, where the scattering shows a transition from

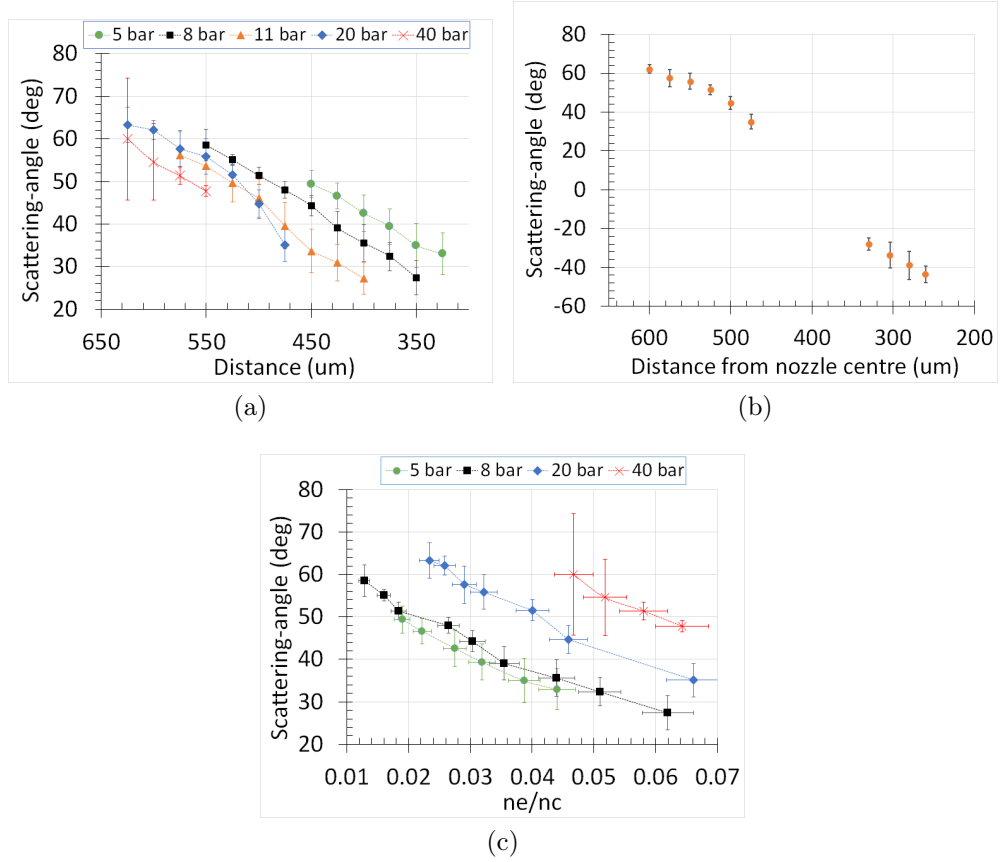


Figure 4.6: (a) Scattering-angle measured along the laser-axis for varying nozzle backing pressure, (b) scattering-angle measured for 20 bar backing pressure showing the transition from upward to downward scattering and (b) variation of the scattering-angle with respect to the electron density.

upward to downward direction. Although downward scattering was also observed for 40 bar backing pressure, the exact distances from the nozzle centre from which the scattering originates could not be measured. This is because, the scattering seems to originate from a strongly localised interaction region at distances close to $\sim 430 \mu\text{m}$ from the nozzle centre and the ionisation stripes indicate that the scattering process is distorted. The measurements also show that the longitudinal positions, from where the scattering starts and where it ends differ for different backing pressures. Figure 4.6c shows the variation of the scattering angle θ_s with respect to the electron density n_e calculated from the prevailing laser intensity and gas density conditions, from which it can be seen that as the density n_e increases, the scattering angle θ_s decreases invariably for all nozzle backing pressures. However, the scattering angle θ_s does not seem to depend on the absolute electron density, as there are multiple angles θ_s observed for the same electron density n_e

suggesting that in addition to n_e , other factors also might play a role.

4.3 Scattering Mechanisms

Some of the possible mechanisms from which side-scattering could originate within the laser-plasma interaction region are as follows:

- **Raman Scattering** - resulting from the decay of the pump laser pulse
- **Plasma Grating** - diffraction of the laser-beam by a grating-like periodic electron density structure
- **Ionisation Induced Defocusing** - occurring due to the divergence caused by the plasma lens
- **Density Gradient Emission** - scattering due to the non-uniform plasma density distribution

This section will attempt to show that most likely the last of the above mentioned mechanisms is the origin of the observed scattering phenomenon.

4.3.1 Raman Scattering

Raman scattering is the result of the decay of a light wave in to another light-wave and an electron plasma wave (refer to section 2.10.2). Its phase matching condition is given by $\vec{k}_0 = \vec{k}_s + \vec{k}_p$, where \vec{k}_0 , \vec{k}_s , \vec{k}_p are the wave vectors of the incoming light wave, scattered light wave and plasma wave. This instability is expected to dominate for plasma densities below $n_c/4$, thus making it relevant in our case. The corresponding dispersion relation describing the propagation of a laser pulse in a plasma medium is described in section 2.10.2 in which only the down shifted frequency component (Stokes, $D[\omega - \omega_0, \mathbf{k} - \mathbf{k}_0]$) is considered to be resonant. Thus, if the pump laser pulse is to undergo Raman decay in a plasma medium, the phenomenon of side-scattering could be viewed as the result of the non-alignment of the resulting light wave and plasma wave wave vectors, as shown in fig. 4.7a. The wave number of the scattered wave k_s is related to the electron density through⁹⁸ $k_s = k_0 \sqrt{1 - 2\sqrt{n_e/n_c}}$, where k_0 is the wave number of the light wave. Therefore, for a given electron density n_e , the wave number k_s remains constant. A more detailed discussion on the properties of the decay light and plasma waves can be found in the next section, where Raman side-scattering was indeed believed to have occurred in the second experiment conducted at the JETI40 laser system. For the maximum non-alignment between the incoming light wave vector \vec{k}_0 and plasma wave vector \vec{k}_p , the

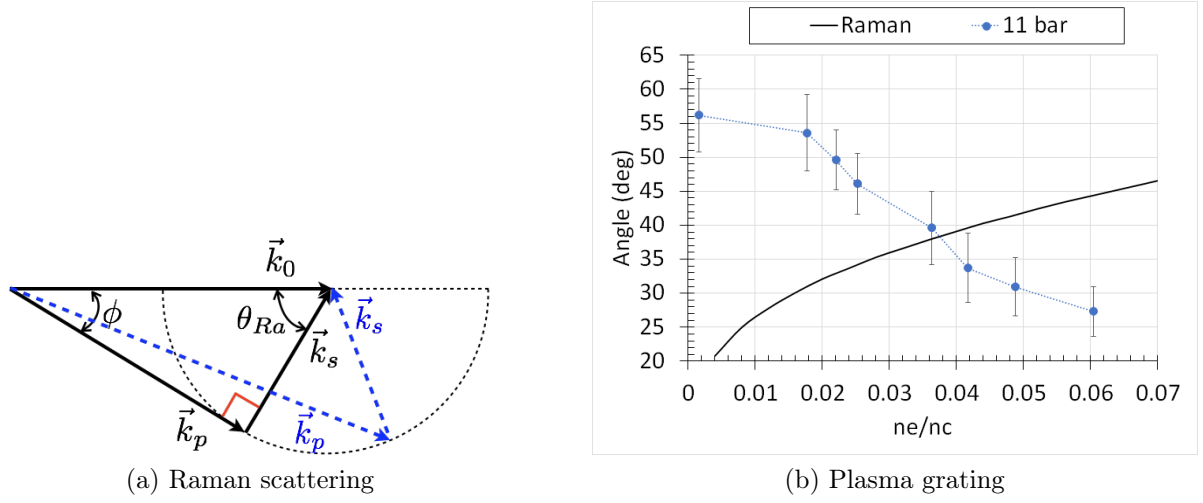


Figure 4.7: (a) Phase-matching condition for Raman side-scattering process, where the wave number of the scattered wave k_s is determined by the electron density through⁹⁸ $k_s = k_0 \sqrt{1 - 2\sqrt{n_e/n_c}}$, where k_0 is the wave number of the light wave, and (b) comparison between the experimentally measured angle for 11 bar backing pressure and the scattering angle calculated from the Raman scattering.

angle θ_{Ra} at which the scattered wave is oriented is given by⁹⁹

$$\sin \theta_{Ra} = \frac{k_p}{k_0} = \sqrt{\frac{2\omega_p}{\sqrt{\gamma_e}\omega_0}} \Rightarrow \boxed{\sin \theta_{Ra} = \left(\frac{4 n_e}{\gamma_e n_c}\right)^{1/4}} \quad (4.1)$$

where θ_{Ra} is the scattering angle, ω_p is the plasma frequency and γ_e is the time averaged Lorentz factor associated with the electron motion. Unlike Raman forward scattering, where the wave vectors are parallel, the wave vector mismatch limits the energy transfer from the pump light wave to the scattered one. For a plasma medium, where the electron density varies continuously along the laser's propagation direction, equation 4.1 entails that the scattering angle θ_{Ra} can also be expected to vary continuously.

Figure 4.7b shows the comparison between the measured scattering angle for 11 bar backing pressure and the scattering angle θ_{Ra} corresponding to the Raman side-scattering, where it can be seen that the scattering-angle θ_{Ra} increases as the electron density n_e increases. This is in stark contrast to that of the measured values. Higher-order Raman scattering could lead to higher scattering angles, but its dependence on the electron density follows the same trend i.e. the scattering angle increases, as the electron density increases. Therefore, it is highly unlikely that Raman scattering is the source of the side-scattering that was observed during the high intensity laser-plasma experiment.

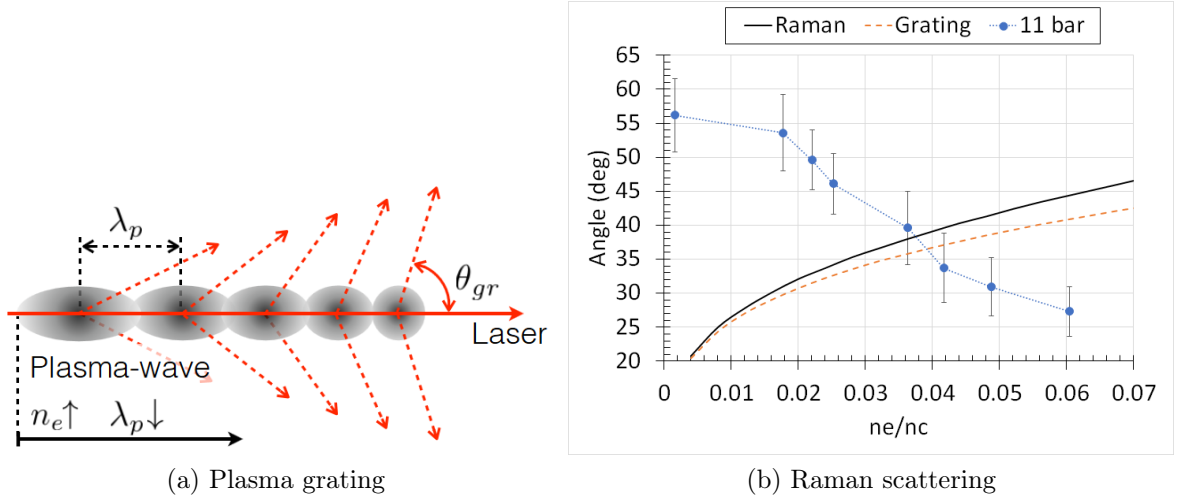


Figure 4.8: (a) Periodic plasma density disturbance acting as a grating structure to diffract the co-linear laser-pulse, and (b) comparison between the experimentally measured angle for 11 bar backing pressure and the scattering-angle calculated from the plasma-wave scattering.

4.3.2 Plasma Grating

As the intense laser pulse propagates in the plasma medium, the ponderomotive force of the laser pulse expels the electrons from its focal region from its ionic background, thus creating a charge separation between the ions and the electrons. As a result of the restoring force offered by ionic background, the electrons are pulled back, and thereby setting up a periodic plasma density disturbance at the trail of the laser front, as described in section 2.7, which is called the plasma-wave. If the spatial extent of the laser pulse in the propagation direction is longer than the period of plasma density oscillation, the periodic electron density disturbance could act as a grating structure to diffract the laser pulse, thus resulting in the laser side-scattering process. For instance, for plasma densities $n_e = 0.01 - 0.25n_c$, the plasma wavelength λ_p varies between $14 - 2.52 \mu\text{m}$, where the laser's FWHM longitudinal spatial extent of $9 \mu\text{m}$ exceeds the plasma wavelength for $n_e \geq 0.03n_c$. The corresponding first-order diffraction angle (θ_{Gr}) is related to the plasma wavelength using the following grating equation

$$\lambda_0 = \lambda_p(\cos \alpha - \cos \theta_{Gr}) \quad (4.2)$$

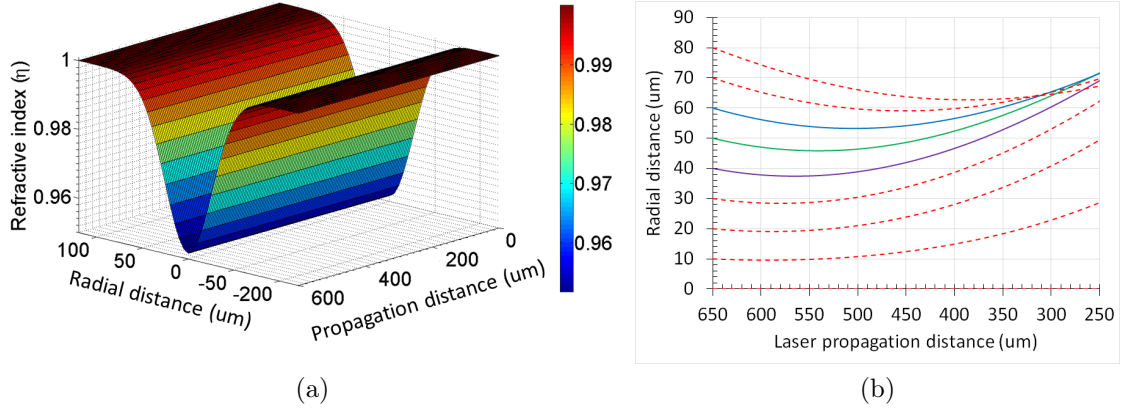


Figure 4.9: (a) Refractive index distribution calculated using the intensity and density conditions at $600 \mu\text{m}$ from the nozzle axis along the laser propagation direction for 20 bar pressure, and (b) corresponding ray-tracing carried out for the laser-pulse focused using an $f/6$ off-axis parabola in the plasma medium.

setting $\alpha = 0^\circ$ for a laser-pulse propagating along the grating-like structure and substituting $\lambda_0/\lambda_p = \omega_p/\sqrt{\gamma_e}\omega_0 = (n_e/\gamma_e n_c)^{1/2}$, the following expression can be obtained

$$\boxed{\cos \theta_{Gr} = 1 - \left(\frac{1}{\gamma_e} \frac{n_e}{n_c} \right)^{1/2}} \quad (4.3)$$

Similar to Raman scattering, for a non-uniform plasma density distribution, the diffraction angle θ_{Gr} can also be expected to continuously change during the laser pulse's propagation direction. The dependence of scattering angle θ_{Gr} on the electron-density n_e , as shown in fig. 4.8b, is similar to that of the scattering angle θ_{Ra} from the Raman scattering relation 4.1, which is again opposite to that of the measured values, where the scattering angle θ_s decreases, as the electron density n_e increases. Furthermore, both of these scattering mechanisms are expected to result in symmetric scattering on both sides of the interaction region and thus fail to explain the asymmetric nature of the experimentally observed scattering process.

4.3.3 Ionization Induced Defocusing

A focused laser pulse propagating through a medium could be defocused before it reaches its peak intensity, if its intensity is sufficiently high to ionise and thus modify the refractive index profile of the medium before the (vacuum) focal plane is reached. Since the intense parts of the laser pulse lead to higher ionisation rates, for non-relativistic intensities ($\gamma_e \approx 1$), a Gaussian intensity distribution leads to a negative-lens-like refractive

index profile, as discussed in detail in section 2.9.1. However, for laser intensities above 10^{17} W/cm² corresponding to the central interaction region, relativistic self-focusing due to electron mass increase and ponderomotive electron expulsion dominates, in general (refer to section 2.9.2). Thus, the propagation of a laser pulse in plasma is determined by the interplay between the focusing and defocusing effects. Furthermore, since the refractive index profile across the laser pulse can vary depending on the prevailing intensity, ionisation state of the atoms and extent of ponderomotive electron expulsion, different parts of the laser pulse could experience different focusing or defocusing effects. Therefore, an exact analysis would require numerical simulations that take into account these effects.

However, in order to find out if ionisation induced defocusing could lead to the side-scattering process, a ray tracing analysis of the laser pulse has been carried out by assuming a constant refractive index distribution along the propagation direction, as shown in fig. 4.9a. Here, the electron density corresponding to the refractive index is not self-consistently calculated depending on the extent of laser pulse's defocusing and the focusing effects such as, relativistic electron mass increase and ponderomotive electron expulsion are neglected and the electron density are calculated. Therefore, any defocusing of the laser pulse should lead to lesser intensities, which might lead to relatively lower argon ionisation states, thereby resulting lower electron densities. Thus, the neglect of the focusing effects and electron-density being not self-consistently calculated leads to an over-estimation of electron density. Figure 4.9b shows the resulting paths taken by the rays representing the focused laser pulse, where it can be clearly seen that even an over-estimation of the extent of defocusing does not lead to such large side-scattering angles observed during the experiment. Furthermore, the defocusing effect is also expected to be symmetric around the laser axis. Therefore, it is highly unlikely that ionisation induced defocusing leads to the phenomenon of asymmetric side-scattering. It should be further noted that early defocusing comes from the outer most region of the laser pulse, not from the intense central region, which is also a further indication that the stripes of ionisation in side-scattering are unlikely to be caused by ionisation induced defocusing.

4.4 Gradient Analysis

Since the scattering mechanisms that have so far been examined do not lead to a satisfactory explanation for the side-scattering process, one has to look beyond these mechanisms to find the source of the scattering process. The preferential nature of the side-scattering (i.e., it is upwards) suggests that perhaps the clues to its origin could lie in the non-uniform nature of the gas jet density profile. As the laser pulse propagates from the outer edges of the gas jet towards its centre, it experiences a change in gas density both in transverse and longitudinal directions. This section show that this asymmetry in gas density can indeed lead to the observed side-scattering process.

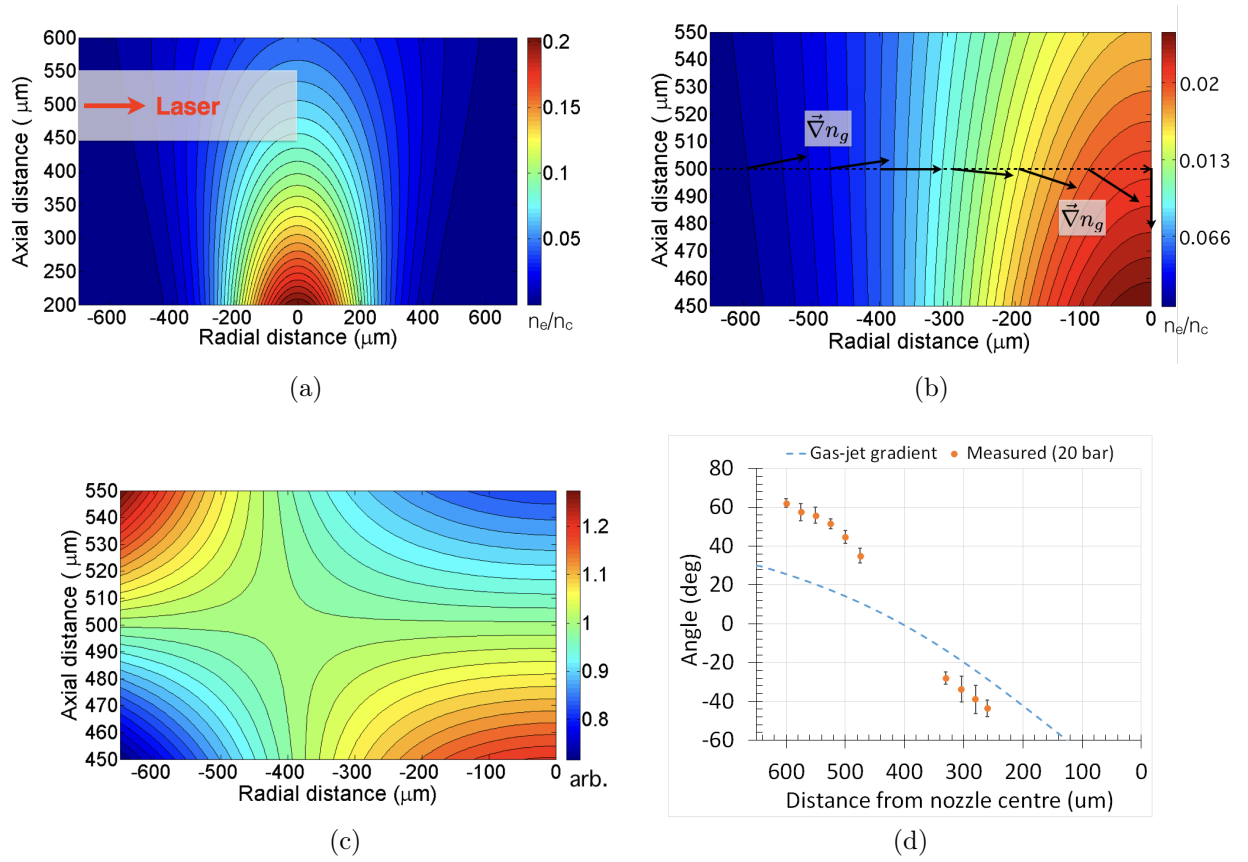


Figure 4.10: (a) Simulated gas-density distribution profile for 20 bar pressure based on the density measurements carried out using the Mach-Zehnder interferometer, (b) close-up view of the region of the gas jet with which the laser pulse interacts, where the arrowed lines along the laser's propagation axis indicate the direction of the gas jet gradient, (c) corresponding plane of asymmetry normalised to 1 along the laser axis indicating the transverse variation of the gas density, and (d) direction of gas density gradient along the laser axis together with the measured scattering angle for 20 bar.

4.4.1 Gas Jet Simulation

The gas density measurements that have been carried out using Mach-Zehnder interferometry contain, in addition to the smooth density variation, high frequency density fluctuations, especially on the edges. This is either inherent to nature of the gas jet, and/or due to the limited phase shift accumulated by part of the portion of the laser beam propagating through the outer regions of the gas jet and/or due to the numerical errors resulting from the Abel inversion process with which the radial phase shift is ob-

tained from the integrated phase shift. The density distribution of the gas jet based on the actual measurements for 20 bar backing pressure is shown in fig. 4.10a, where the local high frequency density fluctuations and the (low frequency) density fluctuations on the outer edges of the gas jet are neglected. Therefore, in order to overcome the presence of the local high frequency density fluctuations, the gas jet distribution has been modelled based on the actual measurements, as shown in fig. 4.10a for 20 bar backing pressure. The graph is plotted in terms of the radial phase shift extracted from the corresponding interferograms, as it is proportional to the gas density and we are only interested in the rate of variation of the gas density distribution along the laser path rather than in the absolute numbers.

A closer look at the interaction region shown in fig. 4.10b, indicates that the density of the gas jet varies continuously from the outer edges of the gas jet to its centre. The non-uniformity of the gas jet is best represented by its gradient* ($\vec{\nabla}n_g$, where n_g represents the local gas density), as indicated by the arrows in fig. 4.10b. As the laser pulse enters the gas jet, the density on the upper side of the laser axis is higher than on its lower side, as indicated by the upward arrows. As the laser pulse propagates further into the gas jet, it encounters a region of uniform transverse density after which, the trend reverses itself, as indicated by the downward arrows. This is best represented by the so called ‘plane of asymmetry’ shown in fig. 4.10c, which is obtained by normalising the density distribution to 1 along the laser axis, where the transverse variations in the gas density can be clearly seen. Figure 4.10d shows the direction of the gas density gradient along the laser axis along with the scattering angle measured for 20 bar backing pressure. Although their absolute values differ from one another, the similarity of the asymmetric nature of the gas density gradient indicates that the origin of scattering could lie on the non-uniform nature of the gas jet. The following section examines the propagation of the laser pulse in the resulting asymmetric plasma density distribution.

4.4.2 Electron Density Analysis

The non-uniform electron density distribution resulting from the ionisation of the gas jet can be obtained by overlapping the plane of asymmetry shown in fig. 4.10c with the symmetric radial electron density distribution shown in fig. 4.11a that could be estimated from the laser’s focusing geometry and the gas density measurements. The electron density distribution is assumed to have a Gaussian transverse profile, but it will be later shown the exact shape of the transverse density profile (e.g. Gaussian) is not of relevance. The resulting non-uniform electron density distribution is shown in fig. 4.11b, where the density asymmetry is indicated by the dotted-lines drawn along the maxima of the contour lines.

Figure 4.12a shows the direction of the electron density gradient ($\vec{\nabla}n_e$) along the laser

*The gradient of a scalar-field points in the direction in which the field increases at the maximum rate

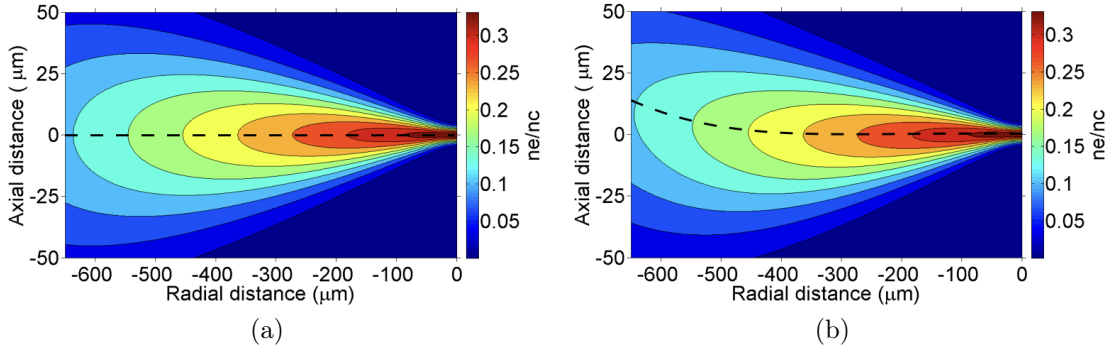


Figure 4.11: (a) Symmetric electron density distribution with respect to the laser's propagation direction for 20 bar backing pressure, where the gas density has been assumed to be symmetric around the laser axis, and (b) asymmetric electron density distribution resulting its overlap with the plane of asymmetry obtained from the corresponding gas jet.

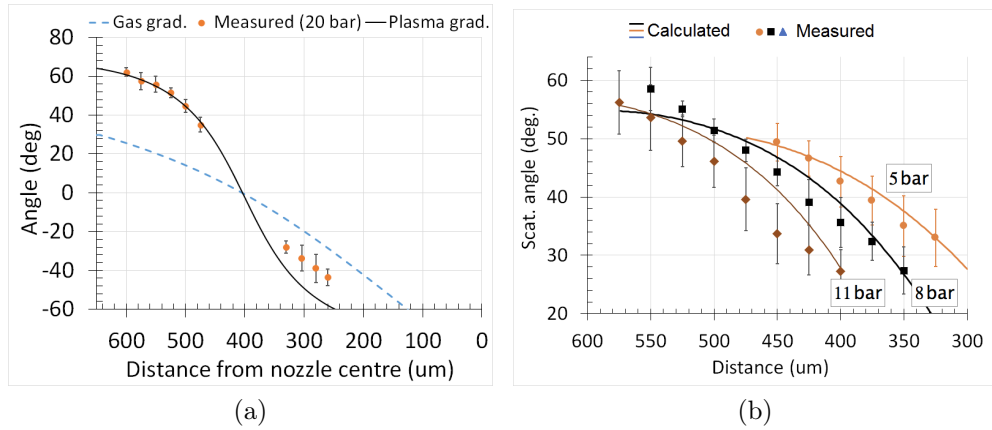


Figure 4.12: (a) Direction of the electron density gradient along the laser axis together with measured scattering angle for 20 bar and the direction of the gas density gradient, and (d) comparison of the simulated and measured scattering angles for multiple nozzle backing pressures.

axis together with the experimentally measured scattering angle values for 20 bar backing pressure, where a good overlap between the two suggests that the side-scattering indeed originates from the intense central interaction region of the laser pulse and propagates away along the direction of the electron density gradient. For distances close to the nozzle centre, the plasma gradient direction slightly deviates from that of the measured scattering angles at negative values, as the corresponding electron density estimates may not hold true any more due to the various propagation effects (refer to section 2.9). Figure 4.12b

shows a similar analysis for 5, 8 and 11 bar backing pressures, where again a good overlap between the measured and calculated values have been observed. It is important to note from fig. 4.12a that the distance at which the direction of both the gas and plasma density gradients correspond to 0° remains unaltered. Thus, the ionisation process can be thought to effectively tilt the plane of asymmetry that is hinged on the line of equi-density going through the point of 0° . The following analysis shows that the choice of the transverse electron density distribution shape (i.e. a Gaussian distribution) is insignificant, as the scattering is shown to originate from the narrow central interaction region.

Mathematical Analysis

The electron-density distribution shown in fig. 4.11b assumes the form $n_e(x,z) = (mx + c) \exp(-z^2/2\sigma_x^2)n_g$, where x - propagation direction, z - transverse direction, $(mx + c)$ - linear axial ionisation factor, σ_x - standard deviation of n_e corresponding to the laser focusing geometry, and $n_g(x,z)$ - gas density distribution. Here, the y dependence is neglected, as the gas density is expected to be symmetric in y -direction and therefore, the plasma density gradient $\vec{\nabla}n_e$ is primarily oriented in the $x - z$ plane. The plasma gradient $\vec{\nabla}n_e$ in the $x - z$ plane can be expressed as follows,

$$\begin{aligned}\vec{\nabla}n_e &= \frac{\partial n_e}{\partial x}\hat{x} + \frac{\partial n_e}{\partial z}\hat{z} \\ &= \exp\left(\frac{-z^2}{2\sigma_x^2}\right) \left[\left(mn_g + (mx + c) \left[\frac{\partial n_g}{\partial x} - n_g \frac{z^2}{\sigma_x^3} \frac{\partial \sigma_x}{\partial x} \right] \right) \hat{x} \right. \\ &\quad \left. + (mx + c) \left(\frac{\partial n_g}{\partial z} - \frac{z}{\sigma_x^2} n_g \right) \hat{z} \right] \\ &= \exp\left(\frac{-z^2}{2\sigma_x^2}\right) \left[(mx + c)\vec{\nabla}n_g + mn_g\hat{x} - (mx + c)\frac{z}{\sigma_x^2} \left(\frac{z}{\sigma_x} \frac{\partial \sigma_x}{\partial x} \hat{x} + \hat{z} \right) \right] \quad (4.4)\end{aligned}$$

since the side-scattering is most likely originating from the intense central interaction region along the propagation direction for which $y \ll \sigma_x$, equation 4.4 can be reduced to

$$\vec{\nabla}n_e = \exp\left(\frac{-z^2}{2\sigma_x^2}\right) \left[(mx + c)\vec{\nabla}n_g + mn_g\hat{x} \right] \quad (4.5)$$

Thus, the direction of the electron-density gradient ($\vec{\nabla}n_e$) is given by,

$$\tan \theta_e = \frac{\partial n_g / \partial z}{\partial n_g / \partial x + n_g(m/(mx + c))} \quad (4.6)$$

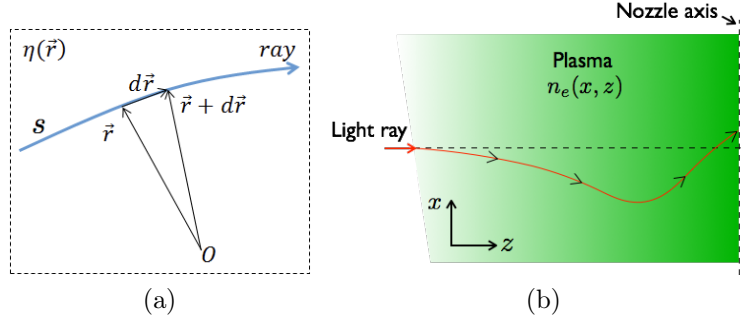


Figure 4.13: (a) Schematic of the light ray propagation in non-uniform media, (b) path taken by a light ray in the non-uniform plasma created by the gas jet ionisation

whereas, the direction of the gas-density gradient ($\vec{\nabla}n_g$) is simply given by,

$$\tan \theta_g = \frac{\partial n_g / \partial z}{\partial n_g / \partial x} \quad (4.7)$$

comparison of eqs. (4.6) and (4.7) shows that the ionisation of atoms modifies only the x -component of the gas density gradient along the laser axis, whereas the z -component remains (nearly) unchanged. Equation 4.6 also indicates that the plasma-gradient is not influenced by the Gaussian distribution function and the distance at which the directions of both $\vec{\nabla}n_e$ and $\vec{\nabla}n_g$ correspond to 0° angle (i.e. along the laser's propagation direction) remains the same. Similarly a non-linear increase in the ionisation factor (instead of a linear increase: $mx + c$) along the laser axis will also lead to a modification of only the x -component of the gas density, as the z -component will also remain (nearly) unchanged.

4.4.3 Origin of Side-scattering

Although the analysis so far shows that side-scattering occurs along the direction of plasma gradient, the mechanism that leads up to the scattering process still remains unresolved. In this section, it is shown to be a direct consequence of the deviation of the pump laser pulse in plasma from its ideal laser axis (straight line).

Ray-tracing

The propagation of a light ray in a medium of non-uniform refractive index (η) can in general be found by solving the eikonal equation of the form:

$$\frac{d}{ds} \left[\eta(\vec{r}) \frac{d\vec{r}}{ds} \right] = \vec{\nabla} \eta(\vec{r}) \quad (4.8)$$

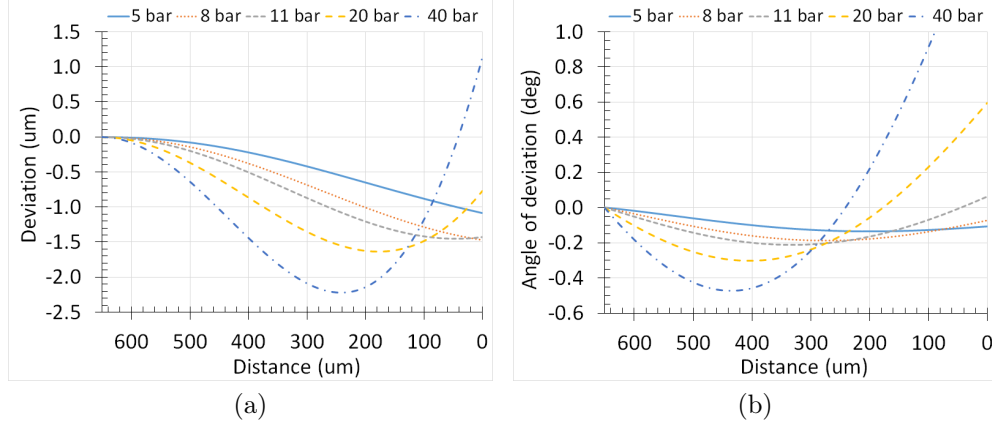


Figure 4.14: (a) Extent of light ray deviation (x_d) from the laser axis for varying pressures, and (b) corresponding angle of light ray deviation (θ_d) measured with respect to the laser axis.

where, \vec{r} is the position vector and s is the propagation distance, as shown in fig. 4.13a. For a 2D refractive index distribution $\eta(x, z)$, it can be expanded to the following form:

$$\left[\frac{\partial \eta}{\partial z} + \frac{\partial \eta}{\partial x} \frac{dx}{dz} \right] \frac{dx}{dz} + \eta(x, z) \frac{d^2 x}{dz^2} = \frac{\partial \eta}{\partial z}$$

$$\eta \frac{d^2 x}{dz^2} + \frac{\partial \eta}{\partial x} \left[\frac{dx}{dz} \right]^2 + \frac{\partial \eta}{\partial z} \left[\frac{dx}{dz} - 1 \right] = 0 \quad (4.9)$$

This is a second-order non-linear differential equation, which can be solved to determine the path taken by the light ray in the medium.

The ray tracing analysis can be used to determine the path undertaken by the intense (central) region of the laser pulse in a non-uniform plasma medium. This can be achieved by assuming a uniform ionisation degree of the argon atoms in the transverse direction (unlike in the previous section, where a Gaussian profile is assumed) depending on the peak intensity of the laser pulse corresponding to the laser's vacuum focusing geometry. This is necessary to ensure the self-consistency of the electron density in the transverse direction, if the laser pulse is to deviate from its propagation axis. The non-uniformity of the gas jet directly leads to the non-uniformity of the plasma density. Though not exact (because of the neglect of the ionisation processes and propagation effects), this analysis helps us to estimate the direction and the extent of deviation of the laser pulse with respect to the straight line. The neglect of the self-focusing and defocusing propagation effects are justified within the distances, over which side-scattering has been observed, as the laser pulse is only mildly relativistic (as discussed in 4.1.3).

Figure 4.13b shows the path taken by a light ray in such a non-uniform plasma, where it can be seen that as the light ray propagates from the outer edges of the gas jet towards

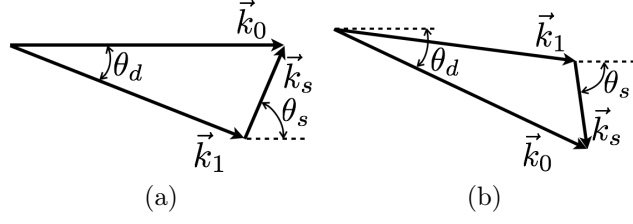


Figure 4.15: Phase matching condition among incoming (\vec{k}_0), refracted (\vec{k}_1) and scattered (\vec{k}_s) components for (a) positive and (b) negative scattering scenarios, respectively.

its centre, it is first deflected below the axis and reverses its direction midway to cross the axis. Figure 4.14a shows the light ray's extent of deviation (x_d) calculated for varying nozzle backing pressures, where it can be seen that the laser pulse can be expected to deviate only a few μm 's from the axis. Whereas, fig. 4.14b shows their corresponding angle of deviation ($\theta_d = \tan^{-1}(dx_d/dz)$) measured with respect to the axis. Although a deviation of few micrometers will hardly be noticeable in the side view images, the following section demonstrates that this small deviation is indeed sufficient to result in the side-scattering phenomenon.

Scattering Mechanism

In addition to energy, a laser pulse also carries linear momentum along its direction of propagation. Thus, in order for the momentum to be conserved, any deviation in the path of the laser pulse could lead to an additional wave vector component, as shown in 4.15. This can be expressed in terms of the phase matching condition $\vec{k}_0 = \vec{k}_1 + \vec{k}_s$, where \vec{k}_0 and \vec{k}_1 represent the incoming and refracted wave vector components, whereas the wave vector \vec{k}_s can be interpreted as the side-scattered wave. Figure 4.15b shows that the deviation of the laser pulse below the laser axis, results in a scattering wave vector \vec{k}_s that is oriented upwards. Whereas, after a certain propagation distance, the laser pulse starts to deviate in the opposite direction, which results in a scattering wave vector that is oriented downwards, as shown in fig. 4.15b.

Figure 4.14b shows the corresponding angle of deviation θ_d of the wave vector, in which decreasing values indicate that the deviation is downwards, as shown in fig. 4.15a. After a certain propagation distance, the angle of deviation θ_d starts to increase indicating that the direction of deviation is now upwards, as shown in fig. 4.15b and the scattering can now be expected to occur at negative angles (i.e. downwards). The experimental observation shown in fig. 4.16 also shows that the scattering gradually changes from upward to downward scattering at a distance where the angle of deviation θ_d is zero, which also coincides with the distance of 0° plasma gradient direction. For 20 and 40 bar backing pressures, the distances at which the scattering orientation changes are $\sim 400 \mu\text{m}$ and $420 \mu\text{m}$ in front of the nozzle centre, which coincides with the position, where the

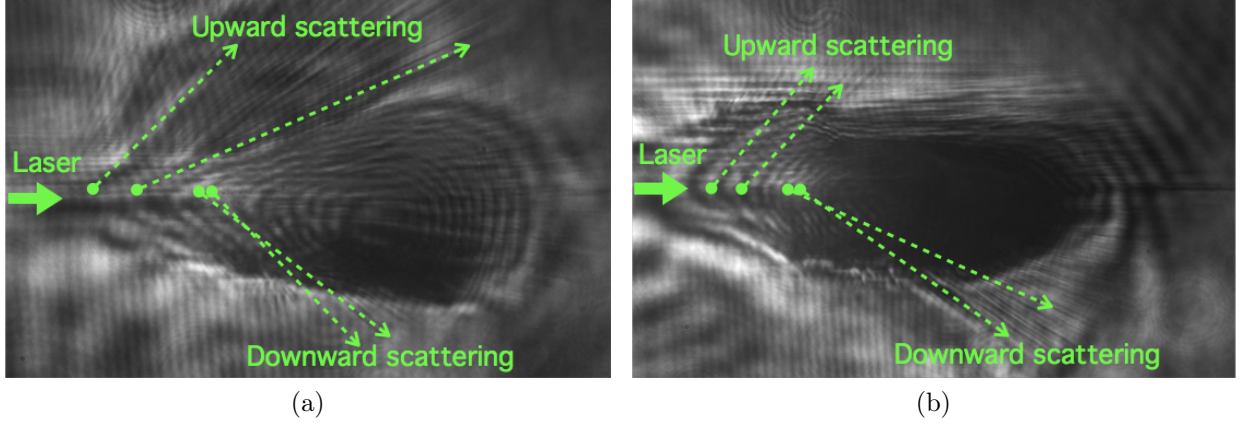


Figure 4.16: Images obtained for (a) 20 bar and (b) 40 bar backing pressures showing the progressive transition of the scattering-angle from upward to downward directions.

electron density gradient is horizontal. In summary, the phenomenon of side-scattering can be viewed as a direct result of the conservation of momentum, whereby a deviation in the laser pulse's propagation direction results in the preferential side-scattering. The scattering being oriented along the direction of the plasma gradient can be understood through the following analysis.

Wave vector Analysis

The analysis that so far has been carried out using the plasma density gradient can be complemented by the use of the wave vector perturbation method, whereby a plasma density perturbation ($\delta n_e \ll n_e < n_c$) is introduced in the expression for the laser's wave number $k = (2\pi/\lambda_0)\eta = (2\pi/\lambda_0)(1 - n_e/n_c)^{1/2}$ in the plasma, as follows,

$$\begin{aligned}
 |\vec{k}| - |\delta\vec{k}| &= \frac{2\pi}{\lambda_0} \sqrt{1 - \frac{(n_e + \delta n_e)}{n_c}} \\
 &= \frac{2\pi}{\lambda_0} \left(1 - \frac{1}{2} \left[\frac{n_e + \delta n_e}{n_c} \right] - \frac{1}{8} \left[\frac{n_e + \delta n_e}{n_c} \right]^2 - \frac{1}{16} \left[\frac{n_e + \delta n_e}{n_c} \right]^3 - \dots \right) \\
 &\approx \frac{2\pi}{\lambda_0} \left(\underbrace{\left[1 - \frac{n_e}{2n_c} - \frac{n_e^2}{8n_c^2} - \frac{n_e^3}{16} - \dots \right]}_{(1 - n_e/n_c)^{1/2}} - \frac{\delta n_e}{2n_c} \underbrace{\left[1 + \frac{n_e}{2n_c} + \frac{3n_e^2}{8n_c^2} \dots \right]}_{(1 - n_e/n_c)^{-1/2}} \right) \\
 &\approx \frac{2\pi}{\lambda_0} \left(\eta - \frac{1}{\eta} \frac{\delta n_e}{2n_c} \right) \tag{4.10}
 \end{aligned}$$

where the higher order term ($\delta n_e^2, \delta n_e^3 \dots$) are neglected. Comparing both sides of the equation, the wave vector component δk ($\ll k_0$) resulting from the plasma density perturbation is given by $\delta k = k_0 \delta n_e / 2n_c \eta$. For a plasma medium with a spatially dependent density distribution, $\delta \vec{k}$ can be written as,

$$\begin{aligned} \frac{\delta k}{\delta l} &= \frac{k_0}{2n_c \eta} \frac{\delta n_e}{\delta l} = \frac{k_0}{2n_c \eta} |\vec{\nabla} n_e| \\ \delta \vec{k} &= \frac{k_0 \delta l}{2n_c \eta} \vec{\nabla} n_e \Rightarrow \boxed{\delta \vec{k} \propto \vec{\nabla} n_e} \end{aligned} \quad (4.11)$$

Thus, the wave vector component $\delta \vec{k}$ is shown to be oriented along the direction of the plasma gradient, which can be interpreted as the scattered light wave component \vec{k}_s observed during the experiment, which was also shown to be oriented along the direction of the plasma gradient. Therefore, this scattering mechanism can be termed as the plasma gradient scattering (PGS).

4.5 March 2015 Experiment

A subsequent high-intensity laser-plasma experiment was conducted at the JETI40 laser system, which was aimed at further examining the laser-plasma interaction dynamics at plasma density and laser intensity combinations different from that of the previous experiment. In this experiment, the laser pulses were focused using an $f/2$ parabola into the centre of the transonic gas jet reaching up to a maximum intensity of 2.5×10^{20} W/cm². The interaction region was probed using a second harmonic probe beam of 400 nm central wavelength, which approximately has the same pulse duration as the pump beam, which is 30 fs. The nozzle backing pressure was varied from 10 – 50 bar.

4.5.1 Side-view Images

Using the side-view diagnostic generating an interferogram, namely Mach-Zehnder interferometry, the laser-plasma interaction was probed at various delay times between the pump and probe laser pulses. The resulting interferograms showed the presence of an undesired pre-pulse, which causes the argon atoms to ionise, thus creating a pre-plasma, as shown in fig. 4.17a. This image was taken ~ 50 ps before the pump-pulse peak arrival. The pre-plasma was observed to have created by the laser pre-pulse at ~ 660 ps before the main laser pulse arrival. Once generated, the pre-plasma expanded radially outwards due to collisions, which could be observed by varying the pump-probe delay times.

Figure 4.17b shows the corresponding electron density distribution obtained by analysing the interferogram in fig. 4.17a, where a bubble-like electron density distribution with a peak density of $0.02n_c$ corresponding to an ionisation state of Ar³⁺ could be observed.

A density line out across the pre-plasma is shown in fig. 4.17c, where the density peaks could be seen. The rate ($R(t)$) at which the density peaks expand radially outwards can be calculated from the Sedov-Taylor equation describing the ‘blast wave’ expansion, which is given by^{173–175},

$$R(t) = \xi \left(\frac{E_l}{\rho_{Ar}} \right)^{1/(\beta+2)} t^{2/(\beta+2)} \quad (4.12)$$

where $\xi = 0.55$ (for ideal gas), E_l is the energy deposited per unit length, ρ_{Ar} is the unperturbed (i.e. neutral) argon mass density, β is a coefficient related to the symmetry of the expansion ($\beta = 1$ (planar), $\beta = 2$ (cylindrical) and $\beta = 3$ (spherical)) and t is the propagation time of the density peak. Here, the pre-plasma expansion is treated as a (nearly) cylindrically symmetric supersonic shock wave expansion after the (spontaneous) deposition of the energy by the pre-pulse. For a pre-plasma length of $\sim 33 \mu\text{m}$, the rate of expansion $R(t)$ that can be calculated from the corresponding interferograms obtained at various probe beam delay times yield a total energy deposition of $\sim 57 \mu\text{J}$. By integrating over the electron density distribution across the pre-plasma, one obtains the average kinetic energy per electron of 460 eV.

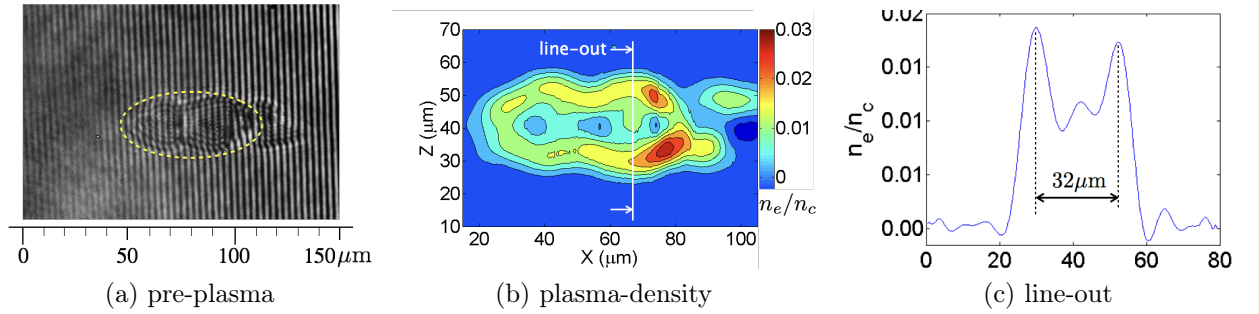


Figure 4.17: (a) Part of the interferogram obtained for 20 bar backing pressure showing the presence of the pre-plasma generated by the pre-pulse, (b) corresponding plasma-density obtained by analysing the interferogram, and (c) variation of the plasma-density across the expanding pre-plasma.

Figure 4.18a shows a shadowgram obtained for 20 bar backing pressure showing the presence of the pre-plasma, whereas fig. 4.18b shows the arrival of the pump pulse, as indicated by its ionisation front. The pre-plasma is formed starting from $\sim 10 \mu\text{m}$ before the vacuum focal plane over $\sim 33 \mu\text{m}$ in length. Thus, the pump pulse upon its arrival interacts with a radially expanding pre-plasma, which scatters off a significant portion its energy, as shown in figs. 4.18c and 4.18d. Furthermore, the expanding pre-plasma, due to its highly non-uniform density distribution along the laser’s propagation direction, might also affect any potential laser particle acceleration mechanisms, such as direct laser

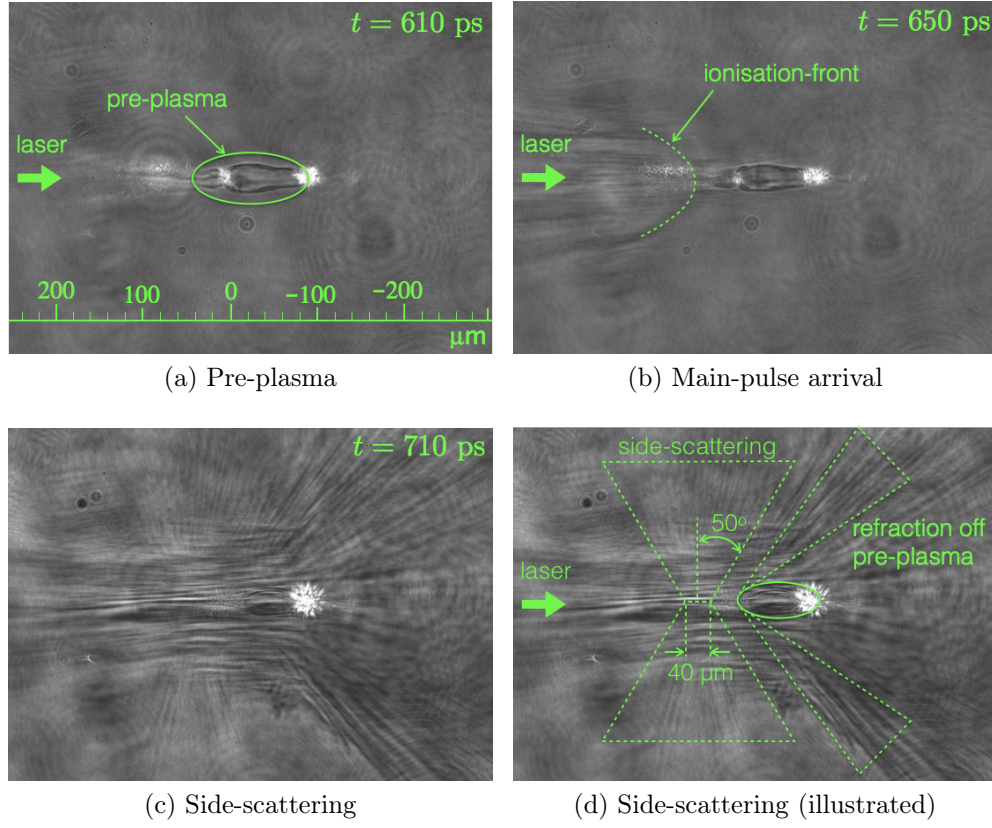


Figure 4.18: Shadowgrams obtained for 10 bar backing pressure at varying probe-beam delay times with respect to the pre-pulse creation showing (a) the pre-plasma created by the pre-pulse, (b) the subsequent arrival of the main-pulse, (c) interaction of the main-pulse with the radially expanding pre-plasma, and (d) is the same as (c) with geometrical guide lines showing side-scattering process and main pulse's refraction of the pre-plasma.

acceleration (described in section 2.8), that could take place at these laser intensities and plasma density conditions. The corresponding electron and ion detection diagnostics present during the experiment also indicate that no energetic electrons and ions of kinetic energy > 5 MeV and < 5 MeV, respectively, could be detected along the forward direction of the laser pulse. The absence of the high energy electrons also rules out the presence of ion energies > 5 MeV.

Figure 4.18d shows that in addition to the pump laser-pulse being scattered off by the pre-plasma, there exists a symmetric side-scattering process, which is indicated by the stripes of ionisation caused by the light scattered in the gas jet. It is assumed to have originated from the central interaction region of $\sim 40 \mu\text{m}$ (in length) at varying distances from the nozzle centre depending on the backing pressure and spreads over an

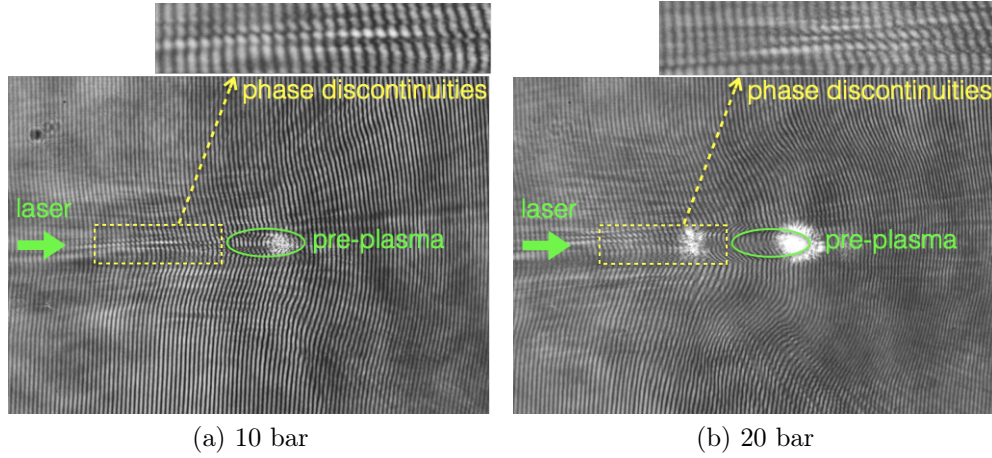


Figure 4.19: Interferograms obtained for (a) 10 bar and (b) 20 bar backing pressure using the Mach-Zehnder interferometry showing the phase discontinuities present in the central interaction region.

angle of $\sim 100^\circ$. The scattering process can be treated as an instability or an energy loss mechanism by which energy is being transported away from the laser-plasma interaction. The following section provides the respective scattering measurements and also an analysis that sheds light into its origin.

The interferograms obtained using the Mach-Zehnder interferometer contain phase discontinuities at the central interaction region, as shown in fig. 4.19, thus rendering them not analysable. Therefore, in the absence of any direct electron density measurements of the laser-plasma interaction region, similar to the previous experiment, the density again needs to be estimated from the gas density measurements and peak laser intensities corresponding to the vacuum focusing geometry. Here, the laser propagation effects, such as ionisation induced defocusing and relativistic self-focusing are similarly ignored. Although the estimated electron densities might deviate from the actual values, it still helps us to understand the mechanism behind the side-scattering process.

4.5.2 Scattering Measurement

The scattering angle (θ_s) measured for backing pressures 10, 20, and 30 bar is shown in fig. 4.20a, where it can be seen that the scattering occurs in a symmetric way (i.e. upwards and downwards) with respect to the laser's propagation axis. The scattering angle varies over $\pm 50^\circ$ with respect to the line perpendicular to the laser's propagation (i.e. over 100° in the observation plane, which is also perpendicular to the polarisation plane of the main laser pulse), as shown in fig. 4.18d. As the backing pressure increases, scattering occurs farther away from the nozzle centre, as the increase in backing pressure enables the laser

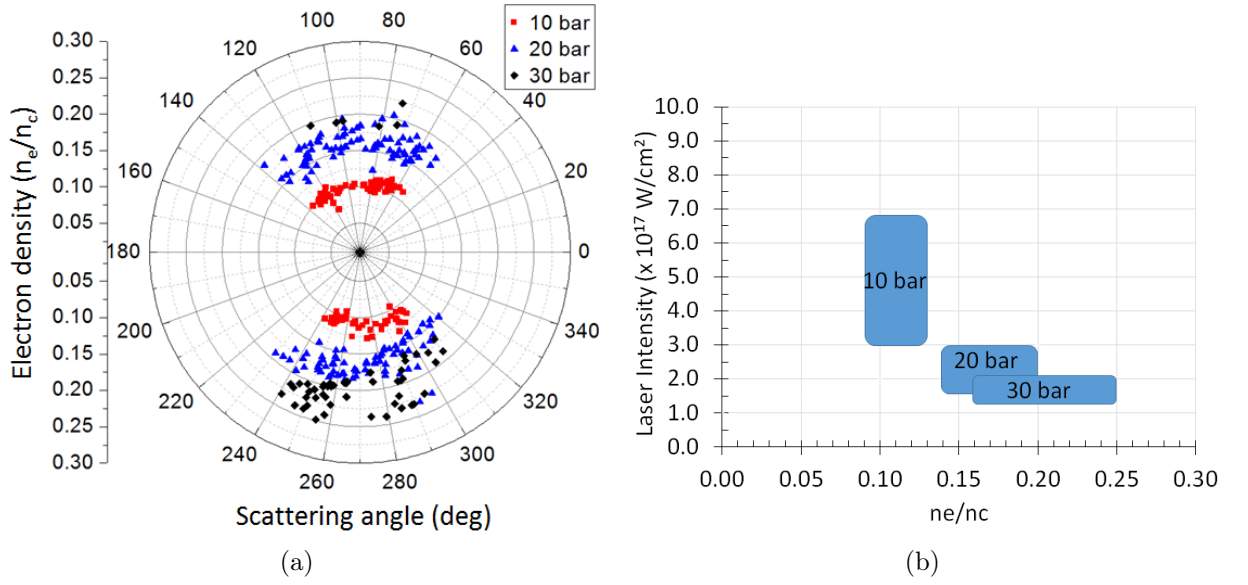


Figure 4.20: (a) Scattering angle measured for backing pressures ranging from 10 – 30 bar with respect to the electron density estimations and (b) combination of laser intensity and electron density ranges within which scattering occurs.

pulse to access the same gas densities farther out from the nozzle centre. For backing pressures > 30 bar, the side-scattering disappears. Figure 4.20b shows the combination of estimated electron densities and peak laser-intensities, over which the side-scattering occurs. These quantities are listed in table 4.1, where it can be seen that the scattering occurs at mildly relativistic laser intensities corresponding to the (maximum) normalised vector potential a_0 in the range of 1.0–1.1. It is found that the scattering process occurs in the (estimated) peak plasma densities ranging from $0.09n_c - 0.25n_c$ (near-critical plasma).

Pressure	Distance from nozzle-centre	Density (n_e/n_c)	Intensity	Relativistic factor (a_0)
bar	um		W/cm ²	
10	75 - 115	0.09 - 0.13	3 - 6.8 e17	1.0 - 1.1
20	115 - 155	0.14 - 0.2	1.6 - 3 e17	
30	135 - 175	0.16 - 0.25	1.25 - 2.1 e17	

Table 4.1: Relevant scattering parameters.

4.5.3 Scattering Origin

The nature of this side-scattering is significantly different from that of the previous experiment, since it is symmetric around the interaction region and does not gradually vary

over the propagation distance. It also has both forward and backward side-scattering components. The observation of side-scattering also suggests that it occurs perpendicular to the pump laser's polarization plane, which is horizontally orientated i.e. perpendicular to the plane of observation. All these factors point towards Raman scattering as a possible mechanism behind the scattering process, where the scattered light wave can be viewed as the result of wave vector mismatch between the incoming light wave and the plasma wave.

Wave-vector Analysis

The phase and frequency matching conditions for the Raman scattering are given by,

$$\vec{k}_0 = \vec{k}_p + \vec{k}_s; \quad \omega_0 = \omega_p + \omega_s \quad (4.13)$$

where the light wave components satisfy the dispersion relation of the form: $\omega^2 = \omega_p^2 + c^2k^2$, where ω and k are the frequency and wave number of the light waves, respectively. Figure 4.21a shows the schematic representation of the wave vector mismatch, which results in the Raman side-scattering process. The corresponding wave number k_s of the scattered light wave can be obtained using the relations section 4.5.3, as follows,

$$\begin{aligned} k_s^2 &= \frac{\omega_s^2 - \omega_p^2}{c^2} = \frac{(\omega_0 - \omega_p)^2 - \omega_p^2}{c^2} = \frac{\omega_0^2}{c^2} \left(\left(1 - \frac{\omega_p}{\omega_0}\right)^2 - \frac{\omega_p^2}{\omega_0^2} \right) \\ k_s &= k_0 \sqrt{1 - 2\frac{\omega_p}{\omega_0}} = k_0 \sqrt{1 - 2\sqrt{\frac{n_e}{n_c}}} \end{aligned} \quad (4.14)$$

where the phase velocity of the scattered wave v_s is given by,

$$\begin{aligned} v_s &= \frac{\omega_s}{k_s} = \frac{\omega_0 - \omega_p}{k_0 \sqrt{1 - 2(\omega_p/\omega_0)}} \\ &= c \frac{1 - (\omega_p/\omega_0)}{\sqrt{1 - 2(\omega_p/\omega_0)}} \equiv c \frac{1 - \sqrt{n_e/n_c}}{\sqrt{1 - 2\sqrt{n_e/n_c}}} \end{aligned} \quad (4.15)$$

whereas its group velocity $v_{s,gr}$ is given by,

$$v_{s,gr} = \frac{c^2}{v_s} = c \frac{\sqrt{1 - 2\sqrt{n_e/n_c}}}{1 - \sqrt{n_e/n_c}} \quad (4.16)$$

Figure 4.21b shows the variation of $v_{s,gr}$ with respect to the electron plasma density n_e , where it can be seen that as n_e approaches $0.25n_c$, $v_{s,gr}$ drops to zero meaning that the

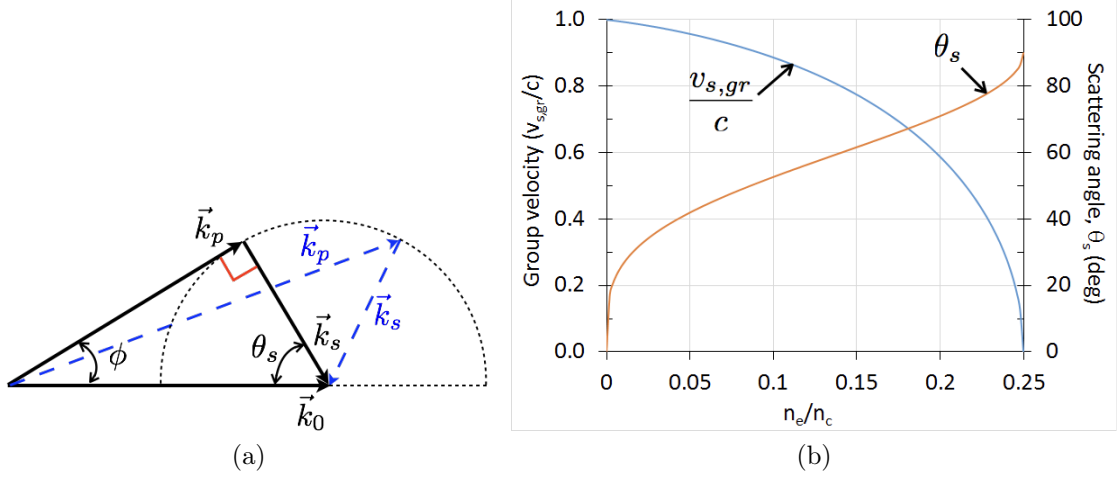


Figure 4.21: (a) Phase matching condition for Raman side-scattering process, and (b) the variation of the scattering angle θ_s with respect to the normalised electron density n_e/n_c , where n_c is the critical density of the plasma.

scattered wave is trapped inside the plasma region. The corresponding phase velocity of the plasma wave v_p is then given by,

$$v_p = \frac{\omega_p}{k_p} = \frac{\omega_0}{k_0} \frac{\omega_p/\omega_0}{\sqrt{2\omega_p/\omega_0}} \quad (4.17)$$

$$= c \sqrt{\frac{\omega_p}{2\omega_0}} = c \left(\frac{n_e}{4n_c} \right)^{1/4} \quad (4.18)$$

where the relation $k_0^2 = k_p^2 + k_s^2$, which corresponds to the maximum wave vector mismatch (shown in fig. 4.21a) is used in obtaining the expression for v_p . For example, for $n_e = 0.1n_c$, $v_p = c/2.5$ and it approaches a value of $c/2$ at electron density $n_e/n_c = 0.25$.

The scattering angle θ_s corresponding to the wave vector mismatch can be related to the wave vectors, as follows,

$$\begin{aligned} k_p &= \sqrt{(k_0 - k_s \cos \theta_s)^2 + k_s^2 \sin^2 \theta_s} \\ &= \sqrt{k_0^2 + k_s^2 - 2k_0 k_s \cos \theta_s} \end{aligned} \quad (4.19)$$

substituting equation 4.14 for k_s , one can obtain the following relation

$$\begin{aligned} k_p &= k_0 \sqrt{2 \left(1 - \frac{\omega_p}{\omega_0} - \sqrt{1 - 2 \frac{\omega_p}{\omega_0} \cos \theta_s} \right)} \\ &= k_0 \sqrt{2 \left(1 - \sqrt{\frac{n_e}{n_c}} - \sqrt{1 - 2 \sqrt{\frac{n_e}{n_c}} \cos \theta_s} \right)} \end{aligned} \quad (4.20)$$

Thus, for a given electron density n_e , the scattering angle θ_s corresponding to the maximum non-alignment between the incoming light wave \vec{k}_0 and the plasma wave \vec{k}_p is given by,

$$\sin \phi_{\max} = \cos \theta_s = \frac{k_s}{k_0} = \sqrt{1 - 2 \frac{\omega_p}{\omega_0}} = \sqrt{1 - 2 \sqrt{\frac{n_e}{n_c}}} \quad (4.21)$$

This yields

$$k_p = k_0 \sqrt{2 \frac{\omega_p}{\omega_0}} = k_0 \left(\frac{4n_e}{n_c} \right)^{1/4} \quad (4.22)$$

At relativistic laser intensities, the time averaged Lorentz factor γ_e can be introduced into the expression for the scattering angle to account for the relativistic electron mass increase, as follows,

$$\boxed{\sin \theta_s = \frac{k_p}{k_0} = \left(\frac{4 n_e}{\gamma_e n_c} \right)^{1/4}} \quad (4.23)$$

Figure 4.21b shows the variation of the scattering angle θ_s with respect to the electron-density n_e , where it can be seen that as n_e approaches quarter critical density ($n_c/4$), θ_s approaches 90° .

Thus, for electron densities at which scattering has been observed, namely from $0.09n_c$ to $0.25n_c$, Raman side-scattering is expected to result in symmetric side-scattering at angles close to the values measured during the experiment. The growth of Raman scattering is expected to be zero at 90° , as the incoming and scattered wave vector are aligned perpendicular to each other⁹⁸. It can be seen from measurements (fig. 4.20a) that there is indeed less scattering observed at 90° , which is suggestive of Raman scattering. Therefore, this analysis suggests that Raman side-scattering is likely to be the source of the scattering observed during this experiment. Unlike Raman forward scattering, where the wave vectors are aligned in-line, the side-scattering limits the region over which the waves can interact, thus limiting the growth of the scattered light. Nevertheless, since laser energy is being transported away from the laser-plasma interaction region, this instability can deplete the pump laser pulse's energy and inhibit the laser pulse from reaching its maximum intensity. From the laser intensity estimates, Raman side-scattering has been shown to have a threshold intensity of $> 1 \times 10^{17} \text{ W/cm}^2$.

4.5.4 Further Comments

When compared to the previous experiment, both plasma gradient and Raman scattering processes seem to occur with in the laser intensity range $1 - 7 \times 10^{17} \text{ W/cm}^2$ and the asymmetric nature of the targets (i.e. gas jet) also remains the same. However, in the second experiment, the plasma gradient scattering could not be observed from the laser-plasma interaction region. This could be due to the short focusing geometry ($f/2$) used in this experiment (in contrast to the $f/6$ geometry in the previous experiment), where the peak laser-intensity increases from $1 - 7 \times 10^{17} \text{ W/cm}^2$ within a longitudinal distance of $120 \mu\text{m}$ (in contrast to $350 \mu\text{m}$ in the previous experiment). This means that the focusing geometry $f/2$ limits the deviation of the laser pulse from its propagation axis due to the asymmetry in the plasma-density distribution within the specified laser intensities, thus hindering the occurrence of the plasma gradient scattering.

With regard to Raman side-scattering not being observed in the first experiment, one possible reason could be the narrow plasma density ranges, within which Raman side-scattering has been observed in the second experiment. The combination of a subsonic gas jet and a focusing geometry of $f/6$ leads to a gradual increase in plasma density, as the focused laser pulse propagates towards the nozzle centre. Whereas, the combination of a transonic gas jet and a focusing geometry of $f/2$ leads to a higher rate of plasma density increase towards the nozzle centre. In addition to the absolute plasma density, if Raman side-scattering is also to be attributed to the rate of change of plasma density, a gradual increase in plasma density might contribute to Raman side-scattering not occurring during the first experiment.

Chapter 5

Conclusion and Outlook

The high-intensity laser-plasma experiments conducted at the high-power laser system JETI in IOQ, which were aimed at exploring the laser-plasma interaction dynamics at near-critical plasma densities. In the first experiment conducted at JETI40, although no energetic particles were detected, a laser side-scattering mechanism was observed, which is treated as an energy loss mechanism, whereby main laser pulse's energy is being transported away from the intense laser-plasma interaction region. The scattering process was shown to be a result of the laser pulse's propagation in a non-uniform plasma, where the scattering angle was shown to be oriented along the direction of the plasma gradient. It was found to occur from under-dense to quarter critical plasma densities for laser intensities ranging from $1 - 6 \times 10^{17} \text{ W/cm}^2$. In addition to the known instabilities, such as Raman scattering and two-plasmon decay, the results from this experiment introduce an additional mechanism, by which laser energy is scattered away by the plasma, which is be termed as the plasma-gradient scattering (PGS).

In the second experiment conducted at JETI40, an undesired pre-pulse was found to exist at 670 ps before the main pulse arrival, which was intense enough to ionise the argon atoms present in the gas jet. Therefore, the main laser-pulse, upon its arrival, was found to interact with an expanding pre-plasma. The highly non-uniform density distribution caused by the expanding pre-plasma along the laser's propagation direction could have affected any electron acceleration process that might take place during the laser-plasma interactions. However, in the regions before the main laser pulse interacts with the pre-plasma, a symmetric side-scattering process was found to occur over limited angles. A subsequent analysis showed that Raman scattering was responsible for the scattering process, which is a result of the wave vector non-alignment between the main laser pulse and the resulting plasma wave. This scattering process was found to occur between $0.09n_c - 0.25n_c$ plasma densities for laser intensities ranging from $1.3 - 6.8 \times 10^{17} \text{ W/cm}^2$.

Understanding these light scattering mechanisms, which occur at specific plasma-density and laser-intensity combinations help to avoid their occurrence in future high-intensity laser-plasma experiments. These experiments could either be aimed, for instance, at exploring particle acceleration mechanisms or laser driven plasma fusion, where intense laser-pulses are focused onto a fusion target, within which the energy transfer from the laser pulses to the target is to be maximised. Any instabilities or mechanisms, by which laser energy might be transported away from the region of interest should be avoided.

Since in both of these scattering mechanisms, the scattered wave is not aligned in-line with the incoming light wave (i.e. the main laser pulse), the growth of the scattered wave is limited. A previous experiment aimed at measuring the Raman side-scattered light, which was carried out using a solid gold target and a nanosecond laser system, showed that up to 4% of the incoming laser energy can be side-scattered¹⁷⁶. Since in PGS mechanism, similar to Raman scattering, the electronic response of the plasma medium facilitates the side-scattering process, a similar fraction of energy loss can be expected. In order to avoid the occurrence of PGS, one can resort to ensuring uniform transverse plasma density across the interaction region. Whereas, the excitation of Raman side-scattering instability can be avoided by going for laser intensities other than the threshold intensity observed during the second experiment.

Bibliography

- [1] M. ROTH, T. E. COWAN, M. H. KEY, S. P. HATCHETT, C. BROWN, W. FOUNTAIN, J. JOHNSON, D. M. PENNINGTON, R. A. SNAVELY, S. C. WILKS, K. YASUIKE, H. RUHL, F. PEGORARO, S. V. BULANOV, E. M. CAMPBELL, M. D. PERRY, H. POWELL, *Fast ignition by intense laser-accelerated proton beams*, Physical Review Letters, 86 (2001), 436–439.
- [2] C. DEUTSCH J.-P. DIDELEZ, *Inertial confinement fusion fast ignition with ultra-relativistic electron beams*, Laser and Particle Beams, 29 (2011), 39–44.
- [3] A. ROBINSON, D. STROZZI, J. DAVIES, L. GREMILLET, J. HONRUBIA, T. JOHZAKI, R. KINGHAM, M. SHERLOCK, A. SOLODOV, *Theory of fast electron transport for fast ignition*, Nuclear Fusion, 54 (2014), 054003.
- [4] D. SCHULZ-ERTNER H. TSUJII, *Particle radiation therapy using proton and heavier ion beams*, Journal of Clinical Oncology, 25 (2007), 953–964.
- [5] S. LE PAPE, M. KOENIG, T. VINCI, E. MARTINOLLI, A. BENNUZZI-MOUNAIX, D. HICKS, P. PATEL, A. MACKINNON, L. ROMAGNANI, M. BORGHESI, S. KAR, T. BOEHLY, *Novel diagnostic of low-Z shock compressed material*, High Energy Density Physics, 2 (2006), 1–6.
- [6] G. ETHERINGTON, A. WRIGHT, J. WENZEL, J. DORE, J. CLARKE, R. SINCLAIR, *A neutron diffraction study of the structure of evaporated amorphous germanium*, Journal of Non-Crystalline Solids, 48 (1982), 265–289.
- [7] S. KIM, B. MARELLI, M. A. BRECKLE, A. N. MITROPOULOS, E. S. GIL, K. TSIORIS, H. TAO, D. L. KAPLAN, F. G. OMENETTO, *All-water-based electron-beam lithography using silk as a resist*, Nature Nanotechnology, 9 (2014), 306–310.
- [8] S. CHATRCHYAN, *Observation of a new boson at a mass of 125 GeV with the CMS experiment at the LHC*, Physics Letters, Section B: Nuclear, Elementary Particle and High-Energy Physics, 716 (2012), 30–61.
- [9] M. ROTH, D. JUNG, K. FALK, N. GULER, O. DEPPERT, M. DEVLIN, A. FAVALLI, J. FERNANDEZ, D. GAUTIER, M. GEISSEL, R. HAIGHT, C. E. HAMILTON, B. M. HEGELICH, R. P. JOHNSON, F. MERRILL, G. SCHAUMANN, K. SCHOENBERG, M. SCHOLLMEIER, T. SHIMADA, T. TADDEUCCI, J. L. TYBO, F. WAGNER, S. A. WENDER, C. H. WILDE, G. A. WURDEN, *Bright laser-driven neutron source based on the relativistic transparency of solids*, Physical Review Letters, 110 (2013), 1–5.

- [10] B. J. HOLZER, *Introduction to Particle Accelerators and their Limitations*, Proceedings of the CAS-CERN Accelerator School: PlasmaWake Acceleration, 1 (2016), 29.
- [11] H. SUIT, T. DELANEY, S. GOLDBERG, H. PAGANETTI, B. CLASIE, L. GERWECK, A. NIEMIERKO, E. HALL, J. FLANZ, J. HALLMAN, A. TROFIMOV, *Proton vs carbon ion beams in the definitive radiation treatment of cancer patients*, Radiotherapy and Oncology, 95 (2010), 3–22.
- [12] SLAC, *Electron Accelerator*{https://portal.slac.stanford.edu/sites/ard_public/facet/newnav/Pages/tf/facet/whatis.aspx}.
- [13] T. TAJIMA J. DAWSON, *Laser Electron Accelerator*, Physical Review Letters, 43 (1979), 267–270.
- [14] J. D. CALLEN, *Lecture notes on Fundamentals of plasma physics*, 2003.
- [15] W. P. LEEMANS, A. J. GONSALVES, H. S. MAO, K. NAKAMURA, C. BENEDETTI, C. B. SCHROEDER, C. TOTH, J. DANIELS, D. E. MITTELBERGER, S. S. BULANOV, J. L. VAY, C. G. R. GEDDES, E. ESAREY, *Multi-Gev electron beams from capillary-discharge-guided subpetawatt laser pulses in the self-trapping regime*, Physical Review Letters, 113 (2014), 1–5.
- [16] C. JOSHI, W. B. MORI, T. KATSOULEAS, J. M. DAWSON, J. M. KINDEL, D. W. FORSLUND, *Ultra-high gradient particle acceleration by intense laser-driven plasma density waves*, Nature, 311 (1984), 525–529.
- [17] J. B. ROSENZWEIG, *Trapping, thermal effects, and wave breaking in the nonlinear plasma wake-field accelerator*, Physical Review A, 38 (1988), 3634–3642.
- [18] E. ESAREY M. PILLOFF, *Trapping and acceleration in nonlinear plasma waves*, Physics of Plasmas, 2 (1995), 1432.
- [19] S. P. D. MANGLES, C. D. MURPHY, Z. NAJMUDIN, A. G. R. THOMAS, J. L. COLLIER, A. E. DANGOR, E. J. DIVALL, P. S. FOSTER, J. G. GALLACHER, C. J. HOOKER, D. A. JAROSZYNSKI, A. J. LANGLEY, W. B. MORI, P. A. NORREYS, F. S. TSUNG, R. VISKUP, B. R. WALTON, K. KRUSHELNICK, *Monoenergetic beams of relativistic electrons from intense laser-plasma interactions.*, Nature, 431 (2004), 535–538.
- [20] J. FAURE, Y. GLINEC, A. PUKHOV, S. KISELEV, S. GORDIENKO, E. LEFEBVRE, J.-P. ROUSSEAU, F. BURGUY, V. MALKA, *A laser-plasma accelerator producing monoenergetic electron beams*, Nature, 431 (2004), 541–544.

- [21] C. G. R. GEDDES, C. S. TOTH, J. VAN TILBORG, E. ESAREY, C. B. SCHROEDER, D. BRUHWILER, C. NIETER, J. CARY, W. P. LEEMANS, *High-quality electron beams from a laser wakefield accelerator using plasma-channel guiding.*, Nature, 431 (2004), 538–41.
- [22] E. GUILLAUME, A. DOEPP, C. THAURY, K. TA PHUOC, A. LIFSCHITZ, G. GRITANI, J. P. GODDET, A. TAFZI, S. W. CHOU, L. VEISZ, V. MALKA, *Electron Rephasing in a Laser-Wakefield Accelerator*, Physical Review Letters, 115 (2015), 1–5.
- [23] P. MORA, *Plasma Expansion into a Vacuum*, Phys. Rev. Lett., 90 (2003), 185002.
- [24] S. P. HATCHETT, C. G. BROWN, T. E. COWAN, E. A. HENRY, J. S. JOHNSON, M. H. KEY, J. A. KOCH, A. B. LANGDON, B. F. LASINSKI, R. W. LEE, A. J. MACKINNON, D. M. PENNINGTON, M. D. PERRY, T. W. PHILLIPS, M. ROTH, T. C. SANGSTER, M. S. SINGH, R. A. SNAVELY, M. A. STOYER, S. C. WILKS, K. YASUIKE, *Electron, photon, and ion beams from the relativistic interaction of Petawatt laser pulses with solid targets*, Physics of Plasmas, 7 (2000), 2076–2082.
- [25] J. FUCHS, P. ANTICI, E. D’HUMIERES, E. LEFEBVRE, M. BORGHESI, E. BRAMBRINK, C. A. CECCHETTI, M. KALUZA, V. MALKA, M. MANCLOSSI, S. MEYRONEINC, P. MORA, J. SCHREIBER, T. TONCIAN, H. PEPIN, P. AUDEBERT, *Laser-driven proton scaling laws and new paths towards energy increase*, Nat Phys, 2 (2006), 48–54.
- [26] T. ESIRKEPOV, M. BORGHESI, S. V. BULANOV, G. MOUROU, T. TAJIMA, *Highly Efficient Relativistic-Ion Generation in the Laser-Piston Regime*, Phys. Rev. Lett., 92 (2004), 175003.
- [27] R. A. SNAVELY, M. H. KEY, S. P. HATCHETT, I. E. COWAN, M. ROTH, T. W. PHILLIPS, M. A. STOYER, E. A. HENRY, T. C. SANGSTER, M. S. SINGH, S. C. WILKS, A. MACKINNON, A. OFFENBERGER, D. M. PENNINGTON, K. YASUIKE, A. B. LANGDON, B. F. LASINSKI, J. JOHNSON, M. D. PERRY, E. M. CAMPBELL, *Intense high-energy proton beams from petawatt-laser irradiation of solids*, Physical Review Letters, 85 (2000), 2945–2948.
- [28] E. L. CLARK, K. KRUSHELNICK, J. R. DAVIES, M. ZEPF, M. TATARAKIS, F. N. BEG, A. MACHACEK, P. A. NORREYS, M. I. K. SANTALA, I. WATTS, A. E. DANGOR, *Measurements of energetic proton transport through magnetized plasma from intense laser interactions with solids*, Physical Review Letters, 84 (2000).
- [29] B. M. HEGELICH, B. J. ALBRIGHT, J. COBBLE, K. FLIPPO, S. LETZRING, M. PAFFETT, H. RUHL, J. SCHREIBER, R. K. SCHULZE, J. C. FERNANDEZ, *Laser acceleration of quasi-monoenergetic MeV ion beams*, Nature, 439 (2006), 441–444.

- [30] H. NISHIMURA, K. MIMA, Y. YANASE, N. BANJOYA, H. FUJITA, K. IBA, M. MATOBA, S. NAKAI, C. YAMANAKA, *Resonance absorption and surface instability at a critical density surface of a plasma irradiated by a CO₂ laser*, Plasma Physics, 22 (1980), 69.
- [31] H. Y. WANG, C. LIN, Z. M. SHENG, B. LIU, S. ZHAO, Z. Y. GUO, Y. R. LU, X. T. HE, J. E. CHEN, X. Q. YAN, *Laser Shaping of a Relativistic Intense, Short Gaussian Pulse by a Plasma Lens*, Physical Review Letters, 107 (2011), 265002.
- [32] A. PUKHOV, Z.-M. SHENG, J. MEYER-TER VEHN, *Particle acceleration in relativistic laser channels*, Physics of Plasmas, 6 (1999), 2847.
- [33] S. C. WILKS, W. L. KRUEER, M. TABAK, A. B. LANGDON, *Absorption of ultra-intense laser pulses*, Phys. Rev. Lett., 69 (1992), 1383.
- [34] S. BULANOV, T. ESIRKEPOV, N. NAUMOVA, F. PEGORARO, V. VSHIVKOV, *Solitonlike Electromagnetic Waves behind a Superintense Laser Pulse in a Plasma*, Physical Review Letters, 82 (1999), 3440–3443.
- [35] S. BULANOV, M. LONTANO, T. ESIRKEPOV, F. PEGORARO, A. PUKHOV, *Electron Vortices Produced by Ultraintense Laser Pulses*, Physical Review Letters, 76 (1996), 3562–3565.
- [36] V. SYLLA, F. AND FLACCO, A. AND KAHALY, S. AND VELTCHEVA, M. AND LIFSCHITZ, A. AND MALKA, V. AND D’HUMIERES, E. AND ANDRIYASH, I. AND TIKHONCHUK, *Short Intense Laser Pulse Collapse in Near-Critical Plasma*, Physical Review Letters, 110 (2013), 085001.
- [37] C. S. BRADY, C. P. RIDGERS, T. D. ARBER, A. R. BELL, *Gamma-ray emission in near critical density plasmas*, Plasma Physics and Controlled Fusion, 55 (2013), 124016.
- [38] A. PUKHOV J. MEYER-TER VEHN, *Relativistic magnetic self-channeling of light in near-critical plasma: Three-dimensional particle-in-cell simulation.*, Physical review letters, 76 (1996), 3975–3978.
- [39] C. GAHN, G. TSAKIRIS, A. PUKHOV, J. MEYER-TER VEHN, G. PRETZLER, P. THIROLF, D. HABS, K. WITTE, *Multi-MeV Electron Beam Generation by Direct Laser Acceleration in High-Density Plasma Channels*, Physical Review Letters, 83 (1999), 4772–4775.
- [40] S. MANGLES, B. WALTON, M. TZOUFRAS, Z. NAJMUDIN, R. CLARKE, A. DANGOR, R. EVANS, S. FRITZLER, A. GOPAL, C. HERNANDEZ-GOMEZ, W. MORI,

- W. ROZMUS, M. TATARAKIS, A. THOMAS, F. TSUNG, M. WEI, K. KRUSHELNICK, *Electron Acceleration in Cavitated Channels Formed by a Petawatt Laser in Low-Density Plasma*, Physical Review Letters, 94 (2005), 245001.
- [41] Y. J. GU, Q. KONG, Y. Y. LI, H. Y. BAN, Z. ZHU, S. KAWATA, *Steady plasma channel formation and particle acceleration in an interaction of an ultraintense laser with near-critical density plasma*, Physics of Plasmas, 18 (2011), 030704.
- [42] P. M. NILSON, A. G. R. THOMAS, K. KRUSHELNICK, R. J. CLARKE, R. HEATHCOTE, W. NAZAROV, N. LOPES, K. MARSH, *Proton acceleration from near critical density foam targets using the Vulcan Petawatt laser*, tech. report, Central Laser Facility, Didcot, 2006.
- [43] L. WILLINGALE, P. M. NILSON, A. G. R. THOMAS, S. S. BULANOV, A. MAK-SIMCHUK, W. NAZAROV, T. C. SANGSTER, C. STOECKL, K. KRUSHELNICK, *High-power, kilojoule laser interactions with near-critical density plasma*, Physics of Plasmas, 18 (2011), 056706.
- [44] J. C. DIELS, W. RUDOLPH, P. F. LIAO, P. KELLEY, *Ultrashort Laser Pulse Phenomena*, Optics and Photonics, Elsevier Science, 2006.
- [45] D. J. GRIFFITHS, *Introduction to Electrodynamics*, Pearson Education, Inc., 5 ed., 2007.
- [46] A. E. SIEGMAN, *Lasers*, University Science Books, 1986.
- [47] R. W. BOYD, *Nonlinear Optics*, vol. 5 of Electronics & Electrical, Academic Press, 2003.
- [48] A. EINSTEIN, *Concerning an heuristic point of view toward the emission and transformation of light*, Annalen der Physik, 17 (1905), 132.
- [49] M. GÖPPERT-MAYER, *Elementary processes with two quantum transitions*, Annalen der Physik, 401 (1931), 273–294.
- [50] L. V. KELDYSH, *Ionization in the field of a strong electromagnetic wave*, Soviet Physics JETP, 20 (1965), 1307–1314.
- [51] S. AUGST, D. D. MEYERHOFER, D. STRICKLAND, S. L. CHINT, *Laser ionization of noble gases by Coulomb-barrier suppression*, 1991.
- [52] J. C. SLATER, *Atomic shielding constants*, Physical Review, 36 (1930), 57–64.
- [53] D. J. GRIFFITHS, *Introduction to Quantum Mechanics*, Pearson Education, Inc., 2005.

- [54] L. D. LANDAU E. M. LIFSHITZ, *Quantum Mechanics - Non-relativistic Theory*, vol. 3, Pergamon Press, 1965.
- [55] A. M. PERELOMOV, V. S. POPOV, M. TARENT'EV, *Ionization of atoms in an alternating electrical field*, Sov. Phys. JETP, 23 (1966), 924.
- [56] M. V. AMMOSOV, N. B. DELONE, V. P. KRAINOV, *Tunnel ionization of complex atoms and of atomic ions in an alternating electromagnetic field*, Sov. Phys. JETP, 64 (1986), 1191–1194.
- [57] P. B. CORKUM, N. H. BURNETT, F. BRUNEL, *Above-threshold ionization in the long-wavelength limit*, Physical Review Letters, 62 (1989), 1259–1262.
- [58] W. P. LEEMANS, C. E. CLAYTON, W. B. MORI, K. A. MARSH, P. K. KAW, A. DYSON, C. JOSHI, J. M. WALLACE, *Experiments and simulations of tunnel-ionized plasmas*, Phys. Rev. A, 46 (1992), 1091–1105.
- [59] P. GIBBON, *Short Pulse Laser Interactions with Matter: An Introduction*, Imperial College Press, London, 2005.
- [60] P. M. WOODWARD, *A method of calculating the field over a plane aperture required to produce a given polar diagram*, 1946.
- [61] J. LAWSON, *Lasers and Accelerators*, Nuclear Science, IEEE Transactions on, 26 (1979), 4217–4219.
- [62] M. C. KALUZA, *Lecture notes on High intensity and Relativistic optics*, Jena, 2010.
- [63] B. QUESNEL P. MORA, *Theory and simulation of the interaction of ultraintense laser pulses with electrons in vacuum*, Physical Review E, 58 (1998), 3719–3732.
- [64] D. BAUER, P. MULSER, W. H. STEEB, *Relativistic ponderomotive force, uphill acceleration, and transition to chaos*, Physical Review Letters, 75 (1995), 4622–4625.
- [65] T. LEHNER, *Intense magnetic field generation by relativistic ponderomotive force in an underdense plasma*, Physica Scripta, 49 (1994), 704–611.
- [66] D. BOHM E. P. GROSS, *Theory of plasma oscillations. A. Origin of medium-like behavior*, Physical Review, 75 (1949), 1851–1864.
- [67] A. PIEL, *Plasma Physics: An Introduction to Laboratory, Space, and Fusion Plasmas*, Springer International Publishing, 2017.
- [68] M. BORN R. OPPENHEIMER, *Zur Quantentheorie der Molekeln*, Annalen der Physik, 84 (1927), 30.

- [69] R. W. BOYD, *Nonlinear Optics*, Electronics & Electrical, Academic Press, 2008.
- [70] F. X. KÄRTNER O. MUECKE, *Lecture notes on Nonlinear Optics*, 2016.
- [71] R. FEYNMAN, M. SANDS, R. B. LEIGHTON, *The Feynman Lectures on Physics*, 1964.
- [72] PROF A WOLSKI, *Lecture Notes on Advanced Electromagnetism*.
- [73] A. EINSTEIN, *Zur Elektrodynamik bewegter Koerper*, annalen der physik, (1905), 891.
- [74] E. LEFEBVRE G. BONNAUD, *Transparency/opacity of a solid target illuminated by an ultrahigh-intensity laser pulse*, Physical Review Letters, 74 (1995), 2002–2005.
- [75] E. HINNOV J. G. HIRSCHBERG, *Electron-Ion Recombination in Dense Plasmas*, Physical Review, 125 (1962), 795.
- [76] L. SERRA, M. SOREL, V. ÁLVAREZ, F. BORGES, M. CAMARGO, S. CÁRCEL, S. CEBRIÁN, A. CERVERA, C. CONDE, T. DAFNI, J. DÍAZ, R. ESTEVE, L. FERNANDES, P. FERRARIO, A. FERREIRA, E. FREITAS, V. GEHMAN, A. GOLDSCHMIDT, J. GÓMEZ-CADENAS, D. GONZÁLEZ-DÍAZ, R. GUTIÉRREZ, J. HAUPTMAN, J. MORATA, D. HERRERA, I. IRASTORZA, L. LABARGA, A. LAING, I. LIUBARSKY, N. LOPEZ-MARCH, D. LORCA, M. LOSADA, G. LUZÓN, A. MARÍ, J. MARTÍN-ALBO, G. MARTÍNEZ-LEMA, A. MARTÍNEZ, T. MILLER, F. MONRABAL, M. MONSERRATE, C. MONTEIRO, F. MORA, L. MOUTINHO, J. VIDAL, M. NEBOT-GUINOT, D. NYGREN, C. OLIVEIRA, J. PÉREZ, J. APARICIO, M. QUEROL, J. RENNER, L. RIPOLL, A. RODRÍGUEZ, J. RODRÍGUEZ, F. SANTOS, J. DOS SANTOS, D. SHUMAN, A. SIMÓN, C. SOFKA, J. TOLEDO, J. TORRENT, Z. TSAMALAIIDZE, J. VELOSO, J. VILLAR, R. WEBB, J. WHITE, N. YAHLALI, *An improved measurement of electron-ion recombination in high-pressure xenon gas*, Journal of Instrumentation, 10 (2015).
- [77] E. ESAREY, R. HUBBARD, W. LEEMANS, A. TING, P. SPRANGLE, *Electron Injection into Plasma Wakefields by Colliding Laser Pulses*, Physical Review Letters, 79 (1997), 2682–2685.
- [78] D. UMSTADTER, E. ESAREY, J. KIM, *Nonlinear plasma waves resonantly driven by optimized laser pulse trains*, Physical Review Letters, 72 (1994), 1224–1227.
- [79] J. FAURE, C. RECHATIN, A. NORLIN, A. LIFSCHITZ, Y. GLINEC, V. MALKA, *Controlled injection and acceleration of electrons in plasma wakefields by colliding laser pulses*, Nature, 444 (2006), 737–739.

- [80] J. FAURE, C. RECHATIN, O. LUNDH, L. AMMOURA, V. MALKA, *Injection and acceleration of quasimonoenergetic relativistic electron beams using density gradients at the edges of a plasma channel*, Physics of Plasmas, 17 (2010).
- [81] M. CHEN, Z. M. SHENG, Y. Y. MA, J. ZHANG, *Electron injection and trapping in a laser wakefield by field ionization to high-charge states of gases*, Journal of Applied Physics, 99 (2006), 2004–2007.
- [82] C. MCGUFFEY, A. G. R. THOMAS, W. SCHUMAKER, T. MATSUOKA, V. CHVYKOV, F. J. DOLLAR, G. KALINTCHENKO, V. YANOVSKY, A. MAKSIMCHUK, K. KRUSHELNICK, V. Y. BYCHENKOV, I. V. GLAZYRIN, A. V. KARPEEV, *Ionization induced trapping in a laser wakefield accelerator*, Physical Review Letters, 104 (2010), 1–4.
- [83] C. E. CLAYTON, J. E. RALPH, F. ALBERT, R. A. FONSECA, S. H. GLENZER, C. JOSHI, W. LU, K. A. MARSH, S. F. MARTINS, W. B. MORI, A. PAK, F. S. TSUNG, B. B. POLLOCK, J. S. ROSS, L. O. SILVA, D. H. FROULA, *Self-guided laser wakefield acceleration beyond 1 GeV using ionization-induced injection*, Physical Review Letters, 105 (2010), 3–6.
- [84] A. BUCK, J. WENZ, J. XU, K. KHRENNIKOV, K. SCHMID, M. HEIGOLDT, J. M. MIKHAILOVA, M. GEISSLER, B. SHEN, F. KRAUSZ, S. KARSCH, L. VEISZ, *Shock-Front Injector for High-Quality Laser-Plasma Acceleration*, Physical Review Letters, 110 (2013), 185006.
- [85] C. THAURY, E. GUILLAUME, A. LIFSCHITZ, K. TA PHUOC, M. HANSSON, G. GRITTANI, J. GAUTIER, J.-P. GODDET, A. TAFZI, O. LUNDH, V. MALKA, *Shock assisted ionization injection in laser-plasma accelerators.*, Scientific reports, 5 (2015), 16310.
- [86] A. J. GONSALVES, K. NAKAMURA, C. LIN, D. PANASENKO, S. SHIRAISHI, T. SOKOLLIK, C. BENEDETTI, C. B. SCHROEDER, C. G. R. GEDDES, J. VAN TILBORG, J. OSTERHOFF, E. ESAREY, C. TOTH, W. P. LEEMANS, *Tunable laser plasma accelerator based on longitudinal density tailoring*, Nature Physics, 7 (2011), 862–866.
- [87] J. GREBENYUK, T. MEHRLING, F. S. TSUNG, K. FLOETTMAN, J. OSTERHOFF, *Simulations of laser-wakefield acceleration with external electron-bunch injection for REGAE experiments at DESY*, AIP Conference Proceedings, 1507 (2012), 688–692.
- [88] A. BUCK, M. NICOLAI, K. SCHMID, C. M. S. SEARS, A. SAVERT, J. M. MIKHAILOVA, F. KRAUSZ, M. C. KALUZA, L. VEISZ, *Real-time observation of laser-driven electron acceleration*, Nat Phys, 7 (2011), 543–548.

- [89] E. ESAREY, B. A. SHADWICK, C. B. SCHROEDER, W. P. LEEMANS, *Nonlinear Pump Depletion and Electron Dephasing in Laser Wakefield Accelerators*, AIP Conference Proceedings, 737 (2004), 578–584.
- [90] J. OSTERHOFF, *Stable ultra-relativistic electron beams by laser-wakefield acceleration*, PhD thesis, Ludwig-Maximilians-Universitaet, 2009.
- [91] C. B. SCHROEDER, E. ESAREY, B. A. SHADWICK, *Warm wave breaking of nonlinear plasma waves with arbitrary phase velocities*, Physical Review E - Statistical, Nonlinear, and Soft Matter Physics, 72 (2005), 3–6.
- [92] E. ESAREY, C. B. SCHROEDER, E. CORMIER-MICHEL, B. A. SHADWICK, C. G. R. GEDDES, W. P. LEEMANS, *Thermal effects in plasma-based accelerators*, Physics of Plasmas, 14 (2007), 1–8.
- [93] E. ESAREY, C. B. SCHROEDER, W. P. LEEMANS, *Physics of laser-driven plasma-based electron accelerators*, Reviews of Modern Physics, 81 (2009), 1229–1285.
- [94] A. PUKHOV J. MEYER-TER VEHN, *Laser wake field acceleration: the highly nonlinear broken-wave regime*, Applied Physics B: Lasers and Optics, 74 (2002), 355–361.
- [95] C. GEDDES, *Computational studies and optimization of wakefield accelerators*, Journal of Physics: Conference Series, (2010).
- [96] V. MALKA, S. FRITZLER, E. LEFEBVRE, M.-M. ALEONARD, F. BURGY, J.-P. CHAMBARET, J.-F. CHEMIN, K. KRUSHELNICK, G. MALKA, S. P. D. MANGLES, Z. NAJMUDIN, M. PITTMAN, J.-P. ROUSSEAU, J.-N. SCHEURER, B. WALTON, A. E. DANGOR, *Electron acceleration by a wake field forced by an intense ultrashort laser pulse.*, Science (New York, N.Y.), 298 (2002), 1596–1600.
- [97] W. P. LEEMANS, B. NAGLER, A. J. GONSALVES, C. TÓTH, K. NAKAMURA, C. G. R. GEDDES, E. ESAREY, C. B. SCHROEDER, S. M. HOOKER, *GeV electron beams from a centimetre-scale accelerator*, Nature Physics, 2 (2006), 696–699.
- [98] W. L. KRUER, *The Physics of Laser Plasma Interactions*, Frontiers in physics, Westview, 2003.
- [99] W. FORSLUND M. KINDEL, *Two-Dimensional Simulations of Single-Frequency and Beat-Wave Laser-Plasma Heating*, Physical Review Letters, 54 (1985), 558.
- [100] E. S. WEIBEL, *Spontaneously Growing Transverse Waves in a Plasma Due to an Anisotropic Velocity Distribution*, Phys. Rev. Lett., 2 (1959), 83.

- [101] S. L. ARTJEMJEVA, O. F. KULIKOV, E. M. MOROZ, K. N. SHORIN, *Betatron oscillation resonances in an electron synchrotron*, Nuclear Instruments and Methods, 2 (1967), 325–330.
- [102] E. ESAREY, B. A. SHADWICK, P. CATRAVAS, W. P. LEEMANS, *Synchrotron radiation from electron beams in plasma-focusing channels*, Physical Review E - Statistical, Nonlinear, and Soft Matter Physics, 65 (2002), 1–15.
- [103] Y. GLINEC, J. FAURE, A. LIFSCHITZ, J. M. VIEIRA, R. A. FONSECA, L. O. SILVA, V. MALKI, *Direct observation of betatron oscillations in a laser-plasma electron accelerator*, EPL (Europhysics Letters), 81 (2008), 64001.
- [104] H. C. WU, B. S. XIE, M. P. LIU, X. R. HONG, S. ZHANG, M. Y. YU, *Electron trajectories and betatron oscillation in the wake bubble in laser-plasma interaction*, Physics of Plasmas, 16 (2009).
- [105] S. CIPICCIA, M. R. ISLAM, B. ERSFELD, R. P. SHANKS, E. BRUNETTI, G. VIEUX, X. YANG, R. C. ISSAC, S. M. WIGGINS, G. H. WELSH, M.-P. ANANIA, D. MANEUSKI, R. MONTGOMERY, G. SMITH, M. HOEK, D. J. HAMILTON, N. R. C. LEMOS, D. SYMES, P. P. RAJEEV, V. O. SHEA, J. M. DIAS, D. A. JAROSZYNSKI, *Gamma-rays from harmonically resonant betatron oscillations in a plasma wake*, Nature Physics, 7 (2011), 867–871.
- [106] M. SCHNELL, A. SÄVERT, B. LANDGRAF, M. REUTER, M. NICOLAI, O. JÄCKEL, C. PETH, T. THIELE, O. JANSEN, A. PUKHOV, O. WILLI, M. C. KALUZA, C. SPIELMANN, *Deducing the Electron-Beam Diameter in a Laser-Plasma Accelerator Using X-Ray Betatron Radiation*, Physical Review Letters, 108 (2012), 075001.
- [107] T. MATSUOKA, C. MCGUFFEY, P. G. CUMMINGS, S. S. BULANOV, V. CHVYKOV, F. DOLLAR, Y. HOROVITZ, G. KALINTCHENKO, K. KRUSHELNICK, P. ROUSSEAU, A. G. R. THOMAS, V. YANOVSKY, A. MAKSIMCHUK, *On electron betatron motion and electron injection in laser wakefield accelerators*, Plasma Physics and Controlled Fusion, 56 (2014), 084009.
- [108] M. SCHNELL, A. SÄVERT, I. USCHMANN, O. JANSEN, M. C. KALUZA, C. SPIELMANN, *Characterization and application of hard x-ray betatron radiation generated by relativistic electrons from a laser-wakefield accelerator*, Journal of Plasma Physics, 81 (2015), 475810401.
- [109] E. ESAREY, S. P., J. KRALL, A. TING, *Review of Plasma-Based Accelerator Concepts*, IEEE Transactions on Plasma Science, 24 (1996), 252.
- [110] W. B. MORI, *The physics of the nonlinear optics of plasmas at relativistic intensities for short-pulse lasers*, IEEE Journal of Quantum Electronics, 33 (1997), 1942–1953.

- [111] R. RANKIN, C. E. CAPJACK, N. H. BURNETT, P. B. CORKUM, *Refraction effects associated with multiphoton ionization and ultrashort-pulse laser propagation in plasma waveguides.*, Optics letters, 16 (1991), 835–837.
- [112] T. AUGUSTE, P. MONOT, L.-A. LOMPRÉ, G. MAINFRAY, C. MANUS, *Defocusing effects of a picosecond terawatt laser pulse in an underdense plasma*, Optics Communications, 89 (1992), 145–148.
- [113] P. GIBBON, F. JAKOBER, P. MONOT, T. AUGUSTE, *Experimental Study of Relativistic Self-Focusing and Self-channeling of an Intense Laser Pulse in an Underdense Plasma*, IEEE Transactions on Plasma Science, 24 (1996), 343–350.
- [114] G. D. TSAKIRIS, R. FEDOSEJEVS, X. F. WANG, *Interaction of TW laser pulses with high density gas jet targets near the threshold for relativistic self-focusing*, AIP Conference Proceedings, 426 (1998).
- [115] R. FEDOSEJEVS, X. WANG, G. TSAKIRIS, *Onset of relativistic self-focusing in high density gas jet targets*, Physical Review E, 56 (1997), 4615–4639.
- [116] M. D. FEIT, A. M. KOMASHKO, A. M. RUBENCHIK, *Relativistic self-focusing in underdense plasma*, Physica D: Nonlinear Phenomena, 152-153 (2001), 705–713.
- [117] A. SULLIVAN, H. HAMSTER, S. P. GORDON, R. W. FALCONE, H. NATHEL, *Propagation of intense, ultrashort laser pulses in plasmas*, Optics letters, 19 (1994), 1544–6.
- [118] R. WAGNER, S.-Y. CHEN, A. MAKSIMCHUK, D. UMSTADTER, *Electron Acceleration by a Laser Wakefield in a Relativistically Self-Guided Channel*, Physical Review Letters, 78 (1997), 3125–3128.
- [119] C. E. MAX, J. ARONST, A. B. LANGDON, *Self-Modulation and Self-Focusing of Electromagnetic Waves in Plasmas*, Physical Review Letters, 33 (1974), 209–212.
- [120] B. M. PENETRANTE, J. N. BARDSLEY, W. M. WOOD, C. W. SIDERS, M. C. DOWNER, *Ionization-induced frequency shifts in intense femtosecond laser pulses*, Journal of the Optical Society of America B, 9 (1992), 2032.
- [121] E. YABLONOVITCH, *Self Phase Modulation and Short Pulse Generation From Laser Breakdown Plasmas*, Physical Review A, 10 (1974), 1888–1895.
- [122] I. WATTS, M. ZEPF, E. L. CLARK, M. TATARAKIS, K. KRUSHELNICK, A. E. DANGOR, R. ALLOTT, R. J. CLARKE, D. NEELY, P. A. NORREYS, *Measurements of relativistic self-phase-modulation in plasma*, Physical Review E - Statistical, Nonlinear, and Soft Matter Physics, 66 (2002), 1–6.

- [123] J. F. DRAKE, *Parametric instabilities of electromagnetic waves in plasmas*, Physics of Fluids, 17 (1974), 778.
- [124] H. G. T. F. LOPEZ, *Investigation of Stimulated Raman Scattering from High Density Underdense Plasmas Irradiated by a 0.35 Micron Laser*, PhD thesis, University of California, 1986.
- [125] A. TING, C. I. MOORE, K. KRUSHELNICK, C. MANKA, E. ESAREY, P. SPRANGLE, R. HUBBARD, H. R. BURRIS, R. FISCHER, M. BAINE, *Plasma wakefield generation and electron acceleration in a self-modulated laser wakefield accelerator experiment*, Physics of Plasmas, 4 (1997), 1889–1899.
- [126] E. ESAREY, B. HAFIZI, R. HUBBARD, A. TING, *Trapping and Acceleration in Self-Modulated Laser Wakefields*, Physical Review Letters, 80 (1998), 5552–5555.
- [127] S. V. BULANOV, F. PEGORARO, A. M. PUKHOV, *Two-dimensional regimes of self-focusing, wake field generation, and induced focusing of a short intense laser pulse in an underdense plasma*, Physical Review Letters, 74 (1995), 710–713.
- [128] C. D. DECKER, W. B. MORI, K.-C. TZENG, T. KATSOULEAS, *The evolution of ultra-intense, short-pulse lasers in underdense plasmas*, Physics of Plasmas, 3 (1996), 2047.
- [129] C. S. LIU, *Raman and Brillouin scattering of electromagnetic waves in inhomogeneous plasmas*, Physics of Fluids, 17 (1974), 1211.
- [130] I. LANGMUIR, *Oscillations in Ionized Gases*, Proceedings of the National Academy of Sciences of the United States of America, 14 (1928), 627–637.
- [131] D. FORSLUND, J. KINDEL, W. MORI, C. JOSHI, J. DAWSON, *Two-dimensional simulations of single-frequency and beat-wave laser-plasma heating.*, Physical Review Letters, 54 (1985), 558–561.
- [132] H. C. BARR, P. MASON, D. M. PARR, *Electron parametric instabilities of relativistically intense laser light in under and overdense plasma*, Physics of Plasmas, 7 (2000), 2604–2615.
- [133] H. BARR, S. BERWICK, P. MASON, *Six-Wave Forward Scattering of Short-Pulse Laser Light at Relativistic Intensities*, Physical Review Letters, 81 (1998), 2910–2913.
- [134] H. C. BARR, P. MASON, D. M. PARR, *Electron Parametric Instabilities Driven by Relativistically Intense Laser Light in Plasma*, Phys. Rev. Lett., 83 (1999), 1606–1609.

- [135] A. TING, C. I. MOORE, K. KRUSHELNICK, C. MANKA, E. ESAREY, P. SPRANGLE, R. HUBBARD, H. R. BURRIS, R. FISCHER, M. BAINE, *Plasma wakefield generation and electron acceleration in a self-modulated laser wakefield accelerator experiment*, *Physics of Plasmas*, 4 (1997), 1889–1899.
- [136] Z. NAJMUDIN, K. KRUSHELNICK, E. L. CLARK, S. P. D. MANGLES, B. WALTON, A. E. DANGOR, S. FRITZLER, V. MALTA, E. LEFEBVRE, D. GORDON, F. S. TSUNG, C. JOSHI, *Self-modulated wakefield and forced laser wakefield acceleration of electrons*, *Physics of Plasmas*, 10 (2003), 2071–2077.
- [137] G. SHVETS, J. S. WURTELE, B. A. SHADWICK, *Analysis and simulation of Raman backscatter in underdense plasmas*, *Physics of Plasmas*, 4 (1997), 1872.
- [138] J. MEYER H. HOUTMAN, *Experimental investigation of the two-plasmon decay instability in a CO₂-laser-produced plasma*, *Physics of Fluids*, 28 (1985), 1549.
- [139] A. A. OFFENBERGER, A. NG, L. PITT, M. R. CERVENAN, *Two-plasmon decay in a CO₂-laser-plasma interaction experiment*, *Physical Review A*, 18 (1978), 746–749.
- [140] B. SINHA, *Observation of two-plasmon decay instability saturation domain in laser-plasma experiments*, *Optics Communications*, 73 (1989), 51–56.
- [141] L. VEISZ, W. THEOBALD, T. FEURER, H. SCHILLINGER, P. GIBBON, R. SAUERBREY, M. S. JOVANOVIĆ, *Three-halves harmonic emission from femtosecond laser produced plasmas*, *Physics of Plasmas*, 9 (2002), 3197–3200.
- [142] L. VEISZ, *Investigation of Parametric Instabilities in Femtosecond Laser-Produced Plasmas*, PhD thesis, University of Jena, 2003.
- [143] L. VEISZ, W. THEOBALD, T. FEURER, H. SCHWOERER, I. USCHMANN, O. RENNER, R. SAUERBREY, *Three-halves harmonic emission from femtosecond laser produced plasmas with steep density gradients*, *Physics of Plasmas*, 11 (2004), 3311–3323.
- [144] R. YAN C. REN, *Two-Plasmon-Decay Instability and Energetic Electron Generation in Direct-Drive Inertial Confinement Fusion*, PhD thesis, University of Rochester, 2012.
- [145] H. X. VU, D. F. DUBOIS, D. A. RUSSELL, J. F. MYATT, J. ZHANG, *Nonlinear development of the two-plasmon decay instability in three dimensions*, *Physics of Plasmas*, 21 (2014), 042705.
- [146] J. ZHANG, J. F. MYATT, R. W. SHORT, A. V. MAXIMOV, H. X. VU, D. F. DUBOIS, D. A. RUSSELL, *Multiple beam two-plasmon decay: Linear threshold to nonlinear saturation in three dimensions*, *Physical Review Letters*, 113 (2014), 1–5.

- [147] R. M. G. M. TRINES, C. D. MURPHY, K. L. LANCASTER, O. CHEKHLOV, P. A. NORREYS, R. BINGHAM, J. T. MENDONÇA, L. O. SILVA, S. MANGLES, C. KAMPERIDIS, A. G. R. THOMAS, K. KRUSHELNICK, Z. NAJMUDIN, *Photon acceleration and modulational instability during wakefield excitation using long laser pulses*, Plasma Physics and Controlled Fusion, 51 (2009), 024008.
- [148] S. C. WILKS, J. M. DAWSON, W. B. MORI, T. KATSOULEAS, M. E. JONES, *Photon accelerator*, Physical Review Letters, 62 (1989), 2600–2603.
- [149] F. AMIRANOFF, M. LABERGE, J. R. MARQUÈS, F. MOULIN, E. FABRE, B. CROS, G. MATTHIEUSSENT, P. BENKHEIRI, F. JACQUET, J. MEYER, P. MINÉ, C. STENZ, P. MORA, *Observation of modulational instability in Nd-laser beat-wave experiments*, Phys. Rev. Lett., 68 (1992), 3710–3713.
- [150] C. D. DECKER, W. B. MORI, K.-C. TZENG, T. KATSOULEAS, *The evolution of ultra-intense, short-pulse lasers in underdense plasmas*, Physics of Plasmas, 3 (1996), 2047.
- [151] C. J. MCKINSTRIE R. BINGHAM, *Stimulated Raman forward scattering and the relativistic modulational instability of light waves in rarefied plasma*, Physics of Fluids B: Plasma Physics, 4 (1992), 2626.
- [152] R. BINGHAM C.N. LASHMORE-DAVIES, *On the Nonlinear Development of the Filamentation of an Electromagnetic wave in a Plasma*, Plasma Physics, 21 (1979), 433–453.
- [153] Z. NAJMUDIN, M. TATARAKIS, K. KRUSHELNICK, E. L. CLARK, V. MALKA, J. FAURE, A. E. DANGOR, *Ultra-High-Intensity Laser Propagation Through Underdense Plasma*, IEEE transactions of plasma science, 30 (2002), 44–45.
- [154] R. W. LEE, R. PETRASSO, R. W. FALCONE, *Science on High-Energy Lasers : From Today to the NIF*, tech. report, 1995.
- [155] R. BINGHAM C. LASHMORE-DAVIES, *Self-modulation and filamentation of electromagnetic waves in a plasma*, Nuclear Fusion, 16 (1976), 67–72.
- [156] S. BATON, F. AMIRANOFF, V. MALKA, A. MODENA, M. SALVATI, C. COULAUD, C. ROUSSEAUX, N. RENARD, P. MOUNAIX, C. STENZ, *Measurement of the stimulated Brillouin scattering reflectivity from a spatially smoothed laser beam in a homogeneous large scale plasma*, Physical Review E, 57 (1998), R4895–R4898.
- [157] T. UMEDA T. ITO, *Vlasov simulation of Langmuir decay instability*, Physics of Plasmas, 15 (2008), 4–7.

- [158] S. DEPIERREUX, C. LABAUNE, J. FUCHS, D. PESME, V. TIKHONCHUK, H. BALDIS, *Langmuir Decay Instability Cascade in Laser-Plasma Experiments*, Physical Review Letters, 89 (2002), 045001.
- [159] K. L. BAKER, K. G. ESTABROOK, R. P. DRAKE, B. B. AFEYAN, *Alternative mechanism for $w_0/2$ emission in laser-produced plasmas*, Physical Review Letters, 86 (2001), 3787–3790.
- [160] K. L. BAKER, *Saturation of Langmuir Waves in Laser-Produced Plasmas*, PhD thesis, University of California, 1996.
- [161] NEWPORT, *Dispersion*{<https://www.newport.com/n/the-effect-of-dispersion-on-ultrashort-pulses>}.
- [162] Eksma Optics{http://eksmaoptics.com/out/media/Ultrathin_Nonlinear_Crystals_Brochure.pdf}.
- [163] SCINTILLATOR, <http://www.crystals.saint-gobain.com/products/organic-scintillation-materials>.
- [164] J. E. HARDY, J. O. HYLTON, T. E. MCKNIGHT, C. J. REMENYIK, F. R. RUPPEL, *Flow Measurement Methods and Applications*, John Wiley & Sons, 1999.
- [165] P. BALACHANDRAN, *Fundamentals of Compressible Fluid Dynamics*, Prentice-Hall of India Pvt. Ltd, 2006.
- [166] P. TOMASSINI A. GIULIETTI, *A generalization of Abel inversion to non-axisymmetric density distribution*, Optics Communications, 199 (2001), 143–148.
- [167] C. J. DASCH, *One-dimensional tomography: a comparison of Abel, onion-peeling, and filtered backprojection methods*, Appl. Opt., 31 (1992), 1146–1152.
- [168] N. ABEL, *Aufloesung einer mechanischen Aufgabe*, Journal fuer die reine und angewandte Mathematik I, 1 (1826), 153–157.
- [169] P. TOMASSINI, A. GIULIETTI, L. A. GIZZI, M. GALIMBERTI, D. GIULIETTI, M. BORGHESI, O. WILLI, *Analyzing Laser Plasma Interferograms with a Continuous Wavelet Transform Ridge Extraction Technique: The Method*, Appl. Opt., 40 (2001), 6561–6568.
- [170] LABVIEW, *Wavelet Transform*{http://zone.ni.com/reference/en-XX/help/371419D-01/lwwavelettk/wa_analytic_wavelet_transform/}.
- [171] LABVIEW, *Phase Unwrapping*{https://zone.ni.com/reference/en-XX/help/371361J-01/lvanls/unwrap_phase/}.

- [172] T. A. CARLSON, C. NESTOR, N. WASSERMAN, J. MCDOWELL, *Calculated ionization potentials for multiply charged ions*, Atomic Data and Nuclear Data Tables, 2 (1970), 63–99.
- [173] A. CAVALIERE A. MESSINA, *Propagation of blast waves*, Astrophysical Journal, 209 (1976), 424–428.
- [174] A. J. MACKINNON, M. BORGHESI, R. GAILLARD, G. MALKA, O. WILLI, A. A. OFFENBERGER, A. PUKHOV, J. MEYER-TER-VEHN, B. CANAUD, J. L. MIQUEL, N. BLANCHOT, *Intense laser pulse propagation and channel formation through plasmas relevant for the fast ignitor scheme*, Physics of Plasmas, 6 (1999), 2185–2190.
- [175] I. A. B. ZELDOVICH Y. P. RAIZER, *Physics of Shock Waves and High-Temperature Hydrodynamic Phenomena*, Dover Books on Physics, Dover Publications, 2002.
- [176] R. P. DRAKE, R. E. TURNER, B. F. LASINSKI, K. G. ESTABROOK, E. M. CAMPBELL, C. L. WANG, D. W. PHILLION, E. A. WILLIAMS, W. L. KRUEER, *Efficient Raman sidescatter and hot-electron production in laser-plasma interaction experiments*, Physical Review Letters, 53 (1984), 1739–1742.

Acknowledgement

Firstly, I would like to extend my warm gratitude to Prof. Dr. Malte C. Kaluza for his extended support and supervision through my research work. On many occasions, his timely support helped me to continue pursuing my research activities despite many odds. I am also grateful to Matthew Schwab for helping me to carry out the experimental campaigns at JETI40. I would also like to thank the other members of my research group for their help and advice during my PhD studies.

I would also like to thank the technical staff members, a few in particular, Diethard Klöpfel, Reinhard Seifert, Falk Ronneberger, Burgard Beleites, and Peter Hanse for being very helpful during the preparatory and execution stages of the experiments at JETI40. Finally, I would also like to thank my friends and family for their moral support during my PhD studies.

Ehrenwörtliche Erklärung

Ich erkläre hiermit ehrenwörtlich, dass ich die vorliegende Arbeit selbständig, ohne unzulässige Hilfe Dritter und ohne Benutzung anderer als der angegebenen Hilfsmittel und Literatur angefertigt habe. Die aus anderen Quellen direkt oder indirekt übernommenen Daten und Konzepte sind unter Angabe der Quelle gekennzeichnet.

Insbesondere habe ich hierfür nicht die entgeltliche Hilfe von Vermittlungs- bzw. Beratungsdiensten (Promotionsberater oder andere Personen) in Anspruch genommen.

Niemand hat von mir unmittelbar oder mittelbar geldwerte Leistungen für Arbeiten erhalten, die im Zusammenhang mit dem Inhalt der vorgelegten Dissertation stehen.

Die Arbeit wurde bisher weder im In- noch im Ausland in gleicher oder ähnlicher Form einer anderen Prüfungsbehörde vorgelegt.

Die geltende Promotionsordnung der Physikalisch-Astronomischen Fakultät ist mir bekannt.

Ich versichere ehrenwörtlich, dass ich nach bestem Wissen die reine Wahrheit gesagt und nichts verschwiegen habe.

Ort, Datum

Unterschrift des Verfassers
